UNIVERSITY OF OKLAHOMA

GRADUATE COLLEGE

EXPLORING THE POTENTIAL OF DYNAMIC MODE DECOMPOSITION IN WIRELESS COMMUNICATION AND NEUROSCIENCE APPLICATIONS

A DISSERTATION

SUBMITTED TO THE GRADUATE FACULTY

in partial fulfillment of the requirements for the

Degree of

DOCTOR OF PHILOSOPHY

in

Electrical and Computer Engineering

By

Ahmed Elsebaay

Norman, Oklahoma

2023

EXPLORING THE POTENTIAL OF DYNAMIC MODE DECOMPOSITION IN WIRELESS COMMUNICATION AND NEUROSCIENCE APPLICATIONS

A DISSERTATION APPROVED FOR THE
SCHOOL OF ELECTRICAL AND COMPUTER ENGINEERING

BY THE COMMITTEE CONSISTING OF

Dr. Hazem H. Refai, Chair

Dr. Choon Yik Tang

Dr. Samuel Cheng

Dr. Adams Curt

To my father, mother, and sister

Acknowledgements

I would like to thank Dr. Hazem Refai for his continuous support, encouragement, and superior way of teaching.

The participation and support of Dr. Choon Yik, Dr. Samuel Cheng, and Dr. Curt Adams on my doctoral committee is greatly appreciated.

The participation of Dr. Elizabeth Hile with CIPN data is greatly appreciated.

My parents, Mohamed and Laila, and sister Fatma are acknowledged for their love and support every step on this journey.

My heartfelt recognition goes to all members of the OU-Tulsa family.

Contents

List of Figures

List of Tables

Abstract

The exponential growth of available experimental, simulation, and historical data from modern systems, including those typically considered divergent (e.g., Neuroscience procedures and wireless networks), has created a persistent need for effective data mining and analysis techniques. Most systems can be characterized as high-dimensional, dynamical, exhibiting rich multiscale phenomena in both space and time. Engineering studies of complex linear and non-linear dynamical systems are especially challenging, as the behavior of the system is often unknown and complex. Studying this problem of interest necessitates discovering and modeling the underlying evolving dynamics. In such cases, a simplified, predictive model of the flow evolution profile must be developed based on observations/measurements collected from the system. Consequently, data-driven algorithms have become an essential tool for modeling and analyzing complex systems characterized by high nonlinearity and dimensionality.

The field of data-driven modeling and analysis of complex systems is rapidly advancing. Associated investigations are poised to revolutionize the engineering, biomedical, and physical sciences. By applying modeling techniques, a complex system can be simplified using low-dimensional models with spatial-temporal structures described using system measurements. Such techniques enable complex system modeling without requiring knowledge of dynamic equations governing the system's operation.

The primary objective of the work detailed in this dissertation was characterizing, identifying, and predicting the behavior of systems under analysis. In particular, characterization and identification entailed finding patterns embedded in system data; prediction required evaluating system dynamics. The

thesis of this work proposes the implementation of dynamic mode decomposition (DMD), which is a fully data-driven technique, to characterize dynamical systems from extracted measurements. DMD employes singular value decomposition (SVD), which reduces high-dimensional measurements collected from a system and computes eigenvalues and eigenvectors of a linear approximated model. In other words, by rather estimating the underlying dynamics within a system, DMD serves as a powerful tool for system characterization without requiring knowledge of the governing dynamical equations.

Overall, the work presented herein demonstrates the potential of DMD for analyzing and modeling complex systems in the emerging, synthesized field of wireless communication (i.e., wireless technology identification) and neuroscience (i.e., chemotherapy-induced peripheral neuropathy [CIPN] identification for cancer patients). In the former, a novel technique based on DMD was initially developed for wireless coexistence analysis. The scheme can differentiate various wireless technologies, including GSM and LTE signals in the cellular domain and IEEE802.11n, ac, and ax in the Wi-Fi domain, as well as Bluetooth and Zigbee in the personal wireless domain. By capturing embedded periodic features transmitted within the signal, the proposed DMD-based technique can identify a signal's time domain signature. With regard to cancer neuroscience, a DMD-based scheme was developed to capture the pattern of plantar pressure variability due to the development of neuropathy resulting from neurotoxic chemotherapy treatment. The developed technique modeled gait pressure variations across multiple steps at three plantar regions, which characterized the development of CIPN in patients with uterine cancer.

Obtained results demonstrated that DMD can effectively model various systems and characterize system dynamics. Given the advantages of fast data processing, minimal required data preprocessing, and minimal required signal

observation time intervals, DMD has proven to be a powerful tool for system analysis and modeling.

Chapter 1 Introduction

The rapid development of technology over the past two decades has precipitated increasingly sophisticated systems-modeling and -analysis methods. Data-driven techniques have played a key role in revolutionizing these approaches and enabled researchers in gaining valuable insights and knowledge from vast amounts of available data. Large dataset analysis can identify patterns and trends that would be difficult—if not impossible—when using traditional methods. Moreover, engineering studies of complex dynamical systems is especially challenging, as the behavior of the system is often unknown and complex. Studying this problem of interest necessitates discovering and modeling the underlying evolving dynamics. In such cases, a simplified, predictive model of the flow evolution profile must be developed based on observations/measurements collected from the system. Consequently, data-driven algorithms have become an essential tool for modeling and analyzing complex systems characterized by high nonlinearity and dimensionality across a range of fields [1, 2].

A data-driven approach enables the development of a model that can accurately capture a system's evolution dynamics without requiring a detailed understanding of the underlying physics. Such models can be useful in a wide range of applications, including but not limited to engineering, fluid dynamics, neuroscience, and biomedical systems. Data-driven techniques for modeling complex dynamical systems are mainly based on two theories: Koopman theory and proper orthogonal decomposition (POD). Koopman theory was first introduced in1931 by mathematician Bernard Koopman [3] as part of his construction of Koopman-von Neumann classical mechanics. The Koopman operator—an infinite-dimensional linear operator that can express the time-evolution of a complex dynamical system-simplifies the modeling of high-dimensional or complex systems [4]. The main alternative to operator-based

Koopman analysis is the projection-based POD method, which achieves model reduction of a high-dimensional system via a Galerkin projection of the temporal dynamics onto a low-dimensional subspace [5, 6].

When compared to Koopman analysis, POD performs better for low-dimensional systems where most of the "energy" is concentrated in a few key states. POD analysis has been used to successfully model various complex systems, including fluid flows, chemical reactions, and biomedical systems. However, its performance can be limited for high-dimensional systems with complex dynamics. Although Koopman analysis is more computationally complex, it provides improved accuracy for high-dimensional systems and greater insight into subtle secondary modes within a narrow frequency band in the dataset. Therefore, the choice between Koopman analysis and POD depends on the specific characteristics of the system being modeled and the research questions under investigation [7, 8].

The work described herein focuses on implementing dynamic mode decomposition (DMD—an algorithm developed by Schmid in 2010 [9]. DMD is a fully data-driven, equation-free, mathematical modelling algorithm that approximates linear infinite-dimensional modes of the Koopman operator. The resulting modes represent infinite-dimensional dynamics. It is notable that DMD allows for their approximation even in the presence of nonlinearity. In other words, DMD modeling can be seen as computing eigenvalues and eigenvectors of a linear model that approximates the underlying dynamics, allowing for the identification of key features of a system's behavior.

While various alternative methods for determining approximation of Koopman operator in data-driven modeling exist (e.g., Generalized Laplace Analysis [10-12], Galerkin discretization [13], [14], Prony analysis [15], and Ulam’s method [16]), DMD has emerged as the most popular implementation of data-driven Koopman spectral analysis [8]. The technique has demonstrated

promising results in a variety of fields. In general, DMD can be leveraged to accomplish two primary tasks [2]:

1. System characterization

   DMD characterizes complex, high-dimensional systems by extracting key low-rank spatiotemporal features, allowing for physically interpretable results in terms of spatial structures and their associated temporal responses.

2. State estimation and future-state prediction

   The generated DMD model can be used for future-state predictions of a dynamical system. DMD utilizes the spatiotemporal structures (i.e., modes) that are dominant in the data to construct dynamical models of the underlying processes observed through best-fit (i.e., least-square) linear model to the dynamical system generating the data.

1.1 Contributions

The work detailed in this dissertation demonstrates DMD as an algorithm for analyzing and modeling complex systems in the fields of wireless communication and cancer research. The treatise provides a brief overview of two specific applications of DMD, as follows.

1. Wireless technology identification.

   This research introduces three novel techniques for wireless technology identification based on DMD data-driven modeling. DMD modes frequency bandwidth-based identification (DMD-BW), DMD mode amplitude-based identification (DMDA), and DMD mode oscillation frequency-based identification (DMDF) techniques were developed for extracting the unique periodic features embedded within a transmitted wireless signal. The

developed algorithms process raw power-measured signals, capturing specifically embedded periodic features within the targeted signals represented in pilot, preamble, synchronization, and control signals. The classification was performed for both individual (or baseline) and different coexistence scenarios. To improve user experiences with signal quality and boost coexistence and spectrum utilization, the aforementioned schemes offer a strategy that can be practically applied to smart radio devices within contemporary heterogeneous networks (i.e., HetNets).

2. Gait cycle analysis for cancer patients' CIPN identification.

   CIPN is a major area of research in the field of cancer. The condition refers to nerve damage that can occur as a side effect of chemotherapy treatment, which leads to troublesome symptoms (i.e., pain, numbness, and tingling in the hands and feet). CIPN can have a significant impact on cancer patients' quality of life, as it may increase the risk of falling while walking. The purpose of this study was analyzing and modeling gait variability in women with uterine cancer who were undergoing chemotherapy treatment. DMD-data driven modeling was used to capture characteristic features of plantar pressure variations between steps for various walking trials.

Classical methods outlined in the related work section in chapter 2 primarily relied on statistical analysis of collected gait parameters. This involved using statistical measures—mean, median, standard deviation, symmetry/asymmetry index, and variability index or variation coefficient—to identify changes in walking behavior. Although such approaches are simple to implement and effective in detecting changes at later stages of a disease, early detection of neuropathy requires more advanced methods to accurately characterize gate cycle dynamics and identify slight changes in the dynamics as a result of CIPN. Recently, machine learning techniques have been introduced to recognize this

paradigm; however, they require additional data preprocessing and expert knowledge to assess the data structure. In this work, a new approach based on DMD is proposed. The developed DMD technique has the advantage of requiring minimal data preprocessing and/or model training. For example, in this study, the DMD method was applied directly to the raw plantar pressure data following foot region segmentation.

Based on outcomes, the proposed methods for using DMD in signal identification provide the following benefits over equivalent methods.

1. Long observation intervals are not necessary, and fewer signal samples are required to execute the technique.

2. The truncated singular value decomposition (SVD) technique used by DMD significantly reduces processing time and computational complexity.

3. When processing signals, time synchronization is not necessary.

4. Identification and classification are direct, one-step processes that do not require further classification techniques for extracting features.

5. Accuracy is not affected by signal power and SNR variations, as DMDA normalizes signal power before classification, and DMDF relies on comparing oscillation frequencies.

6. The techniques can identify signals in real-time.

The balance of this dissertation is organized as follows: Chapter 2 provides a detailed explanation of the standard DMD algorithm, which serves as the primary modeling method for the analysis presented in this study. The chapter emphasizes the relationship between DMD and Koopman theory, in addition to demonstrating how the resulting DMD modes and eigenvalues can be used to describe the dynamics of a system. Chapter 3 reports the development of three novel

techniques for wireless technology identification, namely DMD-BW, DMDA, and DMDF, which are the first to employ a DMD algorithm for identifying signals. Results showed that developed DMD-based algorithms had lower complexity and achieved higher performance for identifying various wireless technologies compared to techniques used in the cited literature. In Chapter 4, DMD was utilized to analyze the impact of neurotoxic chemotherapy on plantar pressure variation among female uterine cancer patients during footfall. To quickly and accurately extract the studied footstep segments, an innovative image processing-based segmentation technique was developed. The magnitude of dominant DMD modes (i.e., eigenvectors) and eigenvalues were used to quantify variation. Results showed that the instability in walking behavior increased as chemotherapy treatment progressed, indicating the progression of neuropathy. Finally, Chapter 5 concludes the dissertation.

Chapter 2 Dynamic Mode Decomposition: Background

The DMD data-driven modeling algorithm is the foundation of identification schemes developed in this dissertation. DMD applications are diverse and include fluid dynamics, image processing, biometrics, neuroscience, and life sciences. In fluid dynamics, DMD was used to extract coherent structures from spatial-temporal fluid flow data and demonstrated its superior capability for extracting relevant modes from complex fluid flows [17-20]. In image processing, DMD was used to separate frames into background and foreground objects [21-23], while in biometrics, DMD was used to detect spoofed samples [24, 25]. In neuroscience, DMD was used to extract coherent patterns in large-scale neural recordings and analyze electrical signals in brain research [26, 27]. In the life sciences, DMD has been used to model complex systems, such as human locomotion [28], brain neural activity [29], and blood flow [30].

Koopman theory forms the rudimentary block for DMD, describing a dynamical system by calculating a linear infinite dimensional (Koopman) operator from a set of observables (i.e., measurements) in the form of a time series signal generated by either experiment or simulation. The operator's eigenvectors (modes) and eigenvalues capture crucial information about the dynamics of a system, describing the evolution of the observables in time. The corresponding eigenvalues describe growth/decay rates and oscillation frequencies for each mode. Jointly, DMD modes and eigenvalues describe dynamics observed in the time series in terms of oscillatory components and serve as an efficient tool for identifying system dominant frequencies. DMD represents a perfect combination

of proper orthogonal decomposition (POD), and Fourier transforms in the time domain [31]. DMD breaks down a dynamical system into a number of approximated Koopman modes. In addition to energy (or amplitude), DMD modes are ranked by detected dynamics (or frequency). As a result, each mode has a distinct amplitude and frequency property [32]. Without relying on presumptions, DMD finds dominant frequencies that show repeating periodicity in signals or systems [33, 34].

2.1 Mathematical Formulation of Koopman Theory

The Koopman operator K_t is an infinite-dimensional linear operator that acts on measurement functions g (i.e., observables), which are elements of an infinite-dimensional Hilbert space:

$$K_t \, \mathrm{g} = \mathrm{g} \, \mathrm{o} \, F_t, \tag{2.1}$$

where o is the composition operator. For a discrete-time system with timestep Δt, Koopman operator advances the observation of the state $\mathrm{g}(x_k)$ to the next time step:

$$g(x_{k+1}) = K_{\Delta t} \, g(x_k) = g\big(F_t(x_k)\big) \tag{2.2}$$

Equation 2.2 indicates that when Koopman operator is applied to a dynamic system with an infinite-dimensional function space, it defines a new infinite-dimensional linear dynamical system that evolves the original dynamic system forward in time. In other words, the application of the infinite-dimensional Koopman operator transitions a system from a finite dimensional nonlinear state space to an infinite-dimensional linear function space [35, 36].

Notably, infinite-dimensionality indicates that many degrees of freedom are required to describe the space among all possible measurement functions of the state g. This complicated process cannot be applied on many systems. Finding a finite-dimensional approximation of Koopman operator has proven to be a

challenging process, involving the identification of a subspace spanned by a subset of eigenfunctions of the Koopman operator [35, 36].

2.2 The standard DMD Algorithm

Assume a dynamical system is approximated by a best linear-fit operator A, which evolves state X forward in time for each k = 1, 2,.....,n-1

$$X_{k+1} = AX_k \tag{2.3}$$

Operator A ∈ R^{mxm} is the best linear fit operator, and it approximates a Koopman operator. Furthermore, the operator satisfies equation (2.3) and represents the solution of a Frobenius norm, least-squares optimization between the one-step future state (X_{k+1}) and the expected future state (AX_k):

$$min \, \|X_{k+1} - AX_k\| \tag{2.4}$$

Consequently, we can write the equation in data matrix format as

$$X' = AX \, , \tag{2.5}$$

where X is the spatial temporal data matrix and X' is the data matrix advanced one step (Δt) in the future.

The standard DMD method can be illustrated in the following steps.

Step 1: Compute the singular value decomposition (SVD) of X.

$$X = U_r \Sigma_r V_r^*, \tag{2.6}$$

Such that: $U_r \in R^{mxr}$, $\Sigma_r \in R^{rxr}$, $V_r \in R^{kxr}$. U_r and Vr consist of r left/right singular vectors corresponding to the r dominant singular values, and Σ_r is the singular values diagonal matrix. The non-negative diagonal elements of Σ_r are the r singular values denoted by σ_i, which are sorted in descending order to satisfy the truncation approximation.

Step 2: Calculate the reduced order matrix $\tilde{A} \in R^{rxr}$. Matrix $\tilde{A}$ describes a low-dimensional, approximated linear model of the system.

$$A = X'X^{\dagger} = X'\, V_r\, {\Sigma_r}^{-1} {U_r}^{*} \tag{2.7}$$

$$\tilde{A} = {U_r}^{*} A\, U_r = {U_r}^{*}\, X' V_r\, {\Sigma_r}^{-1} \tag{2.8}$$

Step 3: Find the eigenvectors and eigenvalues of $\tilde{A}$ by solving the equation.

$$\tilde{A}\, W = \Lambda\, W, \tag{2.9}$$

where † is the Moore–Penrose pseudoinverse, the columns of W are the eigenvectors and Λ is a diagonal matrix containing the corresponding eigenvalues λ_k. Note that λ_k represents the eigenvalues of both A and $\tilde{A}$.

Step 4: Compute the eigenvectors of A (i.e., DMD modes), which are given by columns of matrix Φ ($\Phi \in C^{mxr}$).

$$\Phi = X'\, V_r\, {\Sigma_r}^{-1} W \tag{2.10}$$

To summarize, the DMD algorithm can be seen as an ideal combination of spatial dimensionality-reduction techniques, such as the proper orthogonal decomposition (POD), with Fourier transforms in time [31]. Thus, correlated spatial modes are associated with a given frequency, magnitude, and decay rate. These three parameters are the unique characteristics of each DMD mode. More specifically, DMD modes' characteristic features reflect the dynamics of the input spatiotemporal data (i.e., time domain) in the frequency domain. The method collects snapshots of data X_k from a dynamical system at a number of times tk, where k = 1,2,3, . . . ,m. DMD is a regression of data onto locally linear dynamics $X_k = AX_{k+1}$, where A is chosen to minimize the mean square error between AX_{k+1} and X_k over the whole number of samples denoted by k = 1,2,3, . . . , m −1. Figure 2.1 provides an overview of DMD analysis for time series datasets.

2.3 DMD modes and eigenvalues

DMD dynamic modes are characteristic eigenvectors whose direction does not change following transformation. DMD modes are characterized by energy (amplitude) and dynamics (oscillation frequency). The amplitude determines which DMD mode is more dominant, or, in other words, which mode is more represented in the decomposition. Each DMD mode is associated with a DMD eigenvalue, which describes its temporal behavior. DMD discrete eigenvalues describe the growth/decay and oscillatory characteristics of the corresponding dynamic mode. DMD eigenvalues can be realized by the complex-cartesian coordinate plane in the vicinity of the unitary circle. DMD modes corresponding to eigenvalues inside the unit circle are decaying modes; DMD modes corresponding to eigenvalues outside the unit circle are growing modes. Modes corresponding to eigenvalues on the circle are stable, oscillatory modes [31, 35].

To summarize, DMD is a powerful mathematical tool for analyzing time-series signals in complex systems (i.e., wireless networks and medical systems). DMD extracts the underlying dynamics of a system from high-dimensional data by identifying embedded patterns and trends. More specifically, DMD identifies the dominant modes of the dynamics within a system and separates them from noise and other irrelevant data.

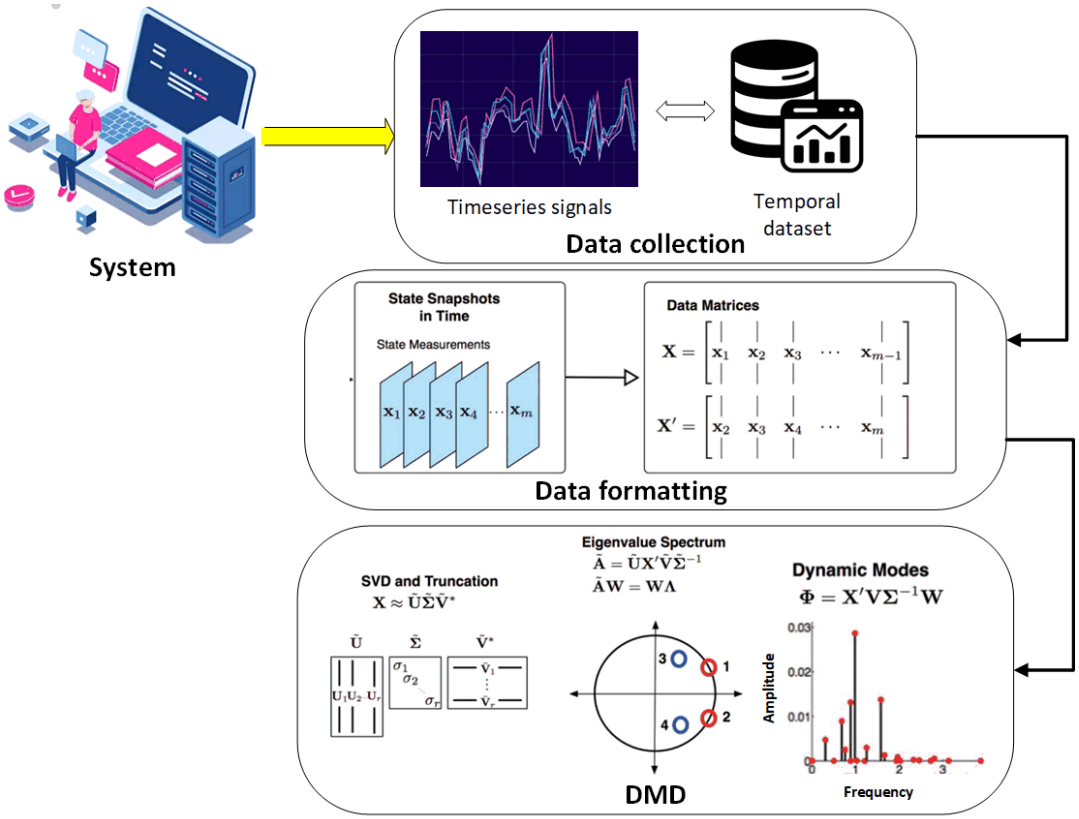

Figure 2.1. System characterization using DMD analysis.

Chapter 3 Wireless Technology Identification Employing DMD

3.1 Background

Escalating traffic demands and significant growth in broadband wireless services, as well as ever-increasing demand on the spectrum caused by vast connectivity and the Internet of Things (IoT), have overstretched limited available spectrum space for wireless services [37, 38], thus, increasing spectrum scarcity. Constrained licensed spectrum resources are simply unable to meet the ever-rising demand [1, 3]. Scarcity and the high cost of licensed spectrum have compelled wireless technologies (e.g., Wi-Fi, ZigBee, and Bluetooth) to share spectrum in unlicensed bands [39]—the Industrial, Scientific, and Medical (ISM) band being one such unlicensed and unrestricted band. Consequently, many technologies attempt to coexist in the ISM band [40]. This trend has led to overutilization and congestion, which, in turn, has caused various levels of interference among coexisting technologies.

Heterogeneous wireless networks (HetNets) − wherein multiple wireless technologies (e.g., Wi-Fi, Bluetooth, Zigbee, LTE, and GSM) coexist and share spectrum−are a promising solution for enhancing spectrum sharing, network capacity, data rate, coverage, and spectrum resource utilization [37, 41, 42]. Ensuring effective coexistence across suitable wireless technologies is imperative. Wireless technologies must be identified within a frequency range for intelligent cognitive radio devices to analyze spectrum occupancy, identify available channels, and model interference while attempting to coexist. Only then can communication be effective and successful [40].

An essential element in developing coexistence protocols is correctly identifying wireless technologies anticipated to share spectrum, and then shifting users

between available wireless technologies in an effort to optimize spectrum usage and minimize interference. For the coexistence research reported in this dissertation, performance of a developed novel algorithm based on DMD mathematical modeling was analyzed to identify and differentiate among various wireless technologies. More specifically, the technique identified GSM and LTE signals in the cellular domain and IEEE802.11n, ac, and ax in the Wi-Fi domain, and Bluetooth, and Zigbee. The proposed DMD-based technique identifies the time domain signature of a signal by capturing embedded periodic features transmitted within the signal. Performance and accuracy were tested and validated using an experimental dataset collected for various time series and raw-power measurements of the targeted technologies. Results showed that the developed DMD-based algorithm can differentiate and classify individual and coexisting wireless signals with high accuracy: greater than 90% for most cases. Furthermore, only a short time–less than one second–is required for identifying a signal and enabling implementation in real-time practical networks. The advantage of the developed technique over comparable techniques is lower complexity (e.g., shorter processing and training time, no channel estimation, no time/frequency synchronization, and no need for long observation-time intervals).

3.2 Related Work

Wireless technology identification schemes can be classified into likelihood-based (LB) and feature-based (FB) methods. Recent research has focused on FB schemes that capture common features shared among similar signal types. Conventional LB methods are based on calculating maximum average probability for proper identification. Comparing LB methods with FB methods reveals that although the latter has suboptimal performance, it has a simpler implementation, lower computational complexity, and relative robustness for modeling mismatches

among various operation cases [37, 43]. Since the DMD used in this work is an FB technique, the related work focuses on FB algorithms based on wavelets, cumulative distribution functions (CDF), second-order cyclostationarity, machine learning (ML), and deep learning (DL). These techniques will be briefly described in the following sections and ordered from oldest to most recent schemes.

3.2.1 Wavelet-based Algorithms

The authors in [44] and [45] introduced a wavelet-based algorithm for identifying GSM and UMTS signals relying on differences in their respective modulation schemes. The algorithm applied wavelet transform to extract transient behaviors within signals resulting from modulation types, and then utilized template matching in the wavelet transform domain for identification. Researchers in [46] and [47] employed wavelet transform for classifying various digitally modulated signals. The wavelet transform magnitude detected distinctive peaks of the transient characteristics of a modulation type, allowing simple processing for identification.

3.2.2 Second-order Cyclostationarity-based Algorithms

Researchers in [48] utilized a second-order cyclostationarity-based algorithm to detect and identify cyclic patterns of GSM, wideband code division multiple access (WCDMA), and orthogonal frequency division multiplexing (OFDM) modulated signals. Cyclostationarity generated by cyclic prefix, preamble, and pilot signals were exploited by [37] to classify GSM, LTE, and CDMA signals utilizing fast Fourier transform (FFT), autocorrelation function (ACF), power spectral density (PSD), and spectral correlation function (SCF) as features for support vector machines (SVM). [49] investigators successfully employed a cyclostationarity-based technique to classify LTE and GSM signals based on their perspective pilot signals. Researchers also investigated the effect of signal-to-noise ratio (SNR) and

observation time on identification accuracy. A classifier model developed by [42] was used for recognizing eight wireless standard signals, namely WCDMA, LTE, GSM, CDMA, Digital Enhanced Cordless Telecommunications (DECT), WLAN, Bluetooth, and Digital Video Broadcasting (DVB). The technique is based on transforming second order cyclostationarity to SCF, and then utilizing it as an input to SVM for classification. By utilizing hidden Markov Models to find second-order cyclic OFDM features, 802.11 a/g signals were categorized in [50]. Authors used a software-defined radio in [51] to present a combined energy detection and cyclostationarity-based technique for detecting IEEE 802.11g and IEEE 802.15.4 signals in the 2.4 GHz range. Ninety percent accuracy was the highest for signals with 1.6 dB SNR.

3.2.3 CDF-based Algorithms

CDF-based algorithms mitigate the primary limiting issues in wavelet-based and cyclostionarity-based algorithms by processing signals that require a shorter observation interval and can tolerate signal SNR variation. Researchers in [52] introduced a novel identification method for distinguishing GSM signals from LTE signals. The amplitude of observed signal samples was employed to extract technology-based features using statistics and signal structures obtained from time and frequency domains. A Kolmogorov-Smirnov (K-S) test was then used to develop a decision principle. This same technique was used in [53] to identify LTE, UMTS, GSM, and CDMA2000 networks.

3.2.4 DL-based Algorithms

Recently, DL-based methods have been introduced as effective techniques for classifying wireless technologies. The fundamental concept behind DL-based algorithms is to input a large number of labeled signal datasets. The neural network then learns and extracts features of a wireless signal technology in the

labeled dataset. Finally, classification is performed based on common features associated with each wireless technology [54].

Convolutional neural networks (CNN) are the most popular DL architectures exploiting both modulation and wireless technology recognition [38]. Highlighting the most recent work in the DL area, researchers in [55] and [56] chiefly constructed classification models based on CNN to process time series signals for GSM, UMTS, and LTE. Authors in [56] enhanced the trained model by utilizing both image and vector representations of the signals. The model achieved high accuracy for classifying signals, including GSM and LTE, with additive white Gaussian noise (AWGN) and Rayleigh fading channels used for identifying UMTS, LTE, and 5G signals simulated by MATLAB LTE and 5G toolboxes. [57] authors proposed a DL-based intelligent recognition method for identifying unlicensed band LTE and Wi-Fi signals generated in a laboratory environment. CNN and recurrent neural network (RNN) models were trained using in-phase and quadrature (IQ) signals.

[58] reported the use of a CNN-based approach for classifying 802.11 b/g, 802.15.4, and 802.15.1 signals that coexist in 2.4GHz unlicensed bands. For SNR greater than or equal to 5 dB, the model's accuracy was greater than 95%. Authors in [59] classified LTE, WiFi, and DVB-T technologies that shared the same ISM band using received signal strength indication (RSSI), IQ samples, and spectrogram features. A CNN model was employed in [40] to distinguish individual and coexisting 802.11n, Bluetooth, and Zigbee signals using frequency domain features. The model was trained using power-frequency measurements taken from the IQ components and recorded at various SNR levels. Researchers compared different ML models' categorization accuracy. Results revealed that for signals with an SNR higher than 15dB, CNN had the highest classification accuracy—greater than 90%. Convolutional denoising autoencoders (CDAEs) were used in a similar study published in [60] to recover distorted spectrograms before categorizing signals with CNN. The model achieved 91% accuracy when identifying IEEE 802.11a, IEEE 802.11n, IEEE 802.11ax, IEEE 802.11ac, and

unlicensed LTE signals. A WaveNet model-adapted neural network was created by authors in [61] to distinguish between 802.11n, 802.11ac, and 802.11ax Wi-Fi signals. Raw power time series data were gathered for both standalone and coexisting signals at different throughputs. The approach had a high classification accuracy of between 90 and 98%. Ten wireless technologies, including Wi-Fi, ZigBee, and Bluetooth, were classified in the 2.4GHz ISM band in [62]. Experimentally, raw IQ samples were collected in an indoor lab. A DL multi-task neural architecture was created by researchers for identifying signals by way of their modulation properties. [63] researchers classified separate and coexisting Bluetooth, Wi-Fi, and microwave signals using a pre-trained, InceptionV3, CNN-based model. ComBlock's commercial, off-the-shelf modules generated signals in the 2.4GHz ISM band. The model's overall accuracy was 98% for 800 testing samples. Researchers in [64] utilized CNN to identify various wireless signals based on their modulation. Constellation diagrams were generated for each signal category, and then used for training and testing several pre-trained CNN-based models, including AlexNet, VGG-16, and VGG-19. Classification accuracy was higher than 85% for signals with SNR greater than 5 dB. Accuracy was extremely low for signals with SNR less than 3 dB. An improved DL model (i.e., multilayer perceptron neural architecture) was proposed in [62, 65] to classify received signals based on their modulation. Signals were classified with accuracy higher than 95% when SNR was greater than 0 dB. Researchers in [66] applied deep residual network (ResNet), convolutional long short term deep neural network (CLDNN), CNN, and RNN on the RadioML dataset. The models successfully classified 11 wireless technologies with SNRs ranging from -20 dB to 18 dB. AutoML was employed to reduce time for training and tuning hyper-parameters of the models. CNN accuracy was highest (i.e., 85% for signals with SNR>2 dB), and RNN was the lowest. Authors in [67] proposed a dilated CNN scheme wherein a one-dimensional modulation signal was converted into a two-dimensional asynchronous delay histogram. Subsequently, the histogram was input to CNN

centered on dilated convolution kernel. The model showed improved accuracy for low SNR signal classification. [68] researchers proposed five CNN models, including ResNet18, SqueezeNet, GoogleNet, MobileNet and RepVGG, for wireless modulation recognition. The SqueezeNet model achieved the highest accuracy of 97.5%, given SNR was +8 dB. Moreover, using weighted ensemble learning improved classification accuracy at low SNR. The ensemble learning model had 52.7% accuracy at SNR of -20 dB and 77% at SNR of -2 dB.

3.2.5 ML-based Algorithms

Although DL approaches achieve high accuracy models with the advantage of simple feature pre-processing or even raw data input, they also require large-scale training datasets, resulting in high implementation costs and significant computational time. As a result, ML techniques, such as SVM in [37, 69] and Random Forest (RF) in [43, 70], have been widely used in related research for identifying various standards' wireless signals. Researchers have demonstrated promising results using SVM with reduced-size datasets [43]. Hierarchical clustering and nearest neighbor classifiers were employed in [71] to classify 802.11b, 802.11g, and Bluetooth signals. The model classified resulting cluster centroids using bandwidth, frequency, and temporal characteristics. A similar method introduced by [72] successfully clustered Wi-Fi and ZigBee, employing unsupervised learning with accuracy ranging between 80 and 90%. Individual and coexisting IEEE 802.11b/g/n, 802.15.4, 802.15.1, and Bluetooth Low Energy (BLE) technologies were categorized by authors in [73] for the 2.4 GHz ISM band. Researchers used a variety of ML algorithms, including decision trees (DT), RF, and SVM, and demonstrated 90 to 97% identification accuracy for signals with SNR greater than 0 dB. A noise robust SVM classification model was developed by researchers [74] to identify various wireless signals based on their modulation. The method was founded on selecting noise-insensitive features from a large

feature set to ensure that the trained classifiers were robust to SNR variations. Features were selected by normalizing variances among all features, such that features with large variances were eliminated from the initial set. The model achieved classification accuracy above 92% when SNR varied between 5 and 20 dB. [75] authors proposed a low-complexity technique to classify numerically simulated wireless signals having 2ASK, QPSK, and 16QAM modulations. Signals simulated with SNRs varied from 0 to 30 dB. The proposed approach used an SVM-model trained by features extracted through principal component analysis (PCA). The proposed model was able to identify signals based on their modulation with 99.83% accuracy. Authors in [76] classified various digitally modulated signals using multi-layer perceptrons (MLP), radial basis function (RBF), adaptive neuro-fuzzy inference system (ANFIS), decision tree (DT), and naïve Bayes (NB), SVM ML-algorithms. Optimal parameters for each model were obtained by utilizing a genetic algorithm (GA). Simulated signals were generated in the presence of additive white Gaussian noise (AWGN) with an SNR ranging between −10 dB and 30 dB. SVM achieved the highest classification accuracy: greater than 90% over the entire SNR range..

3.3 Research Contribution Compared to Literature

The FB approaches detailed above are based on extracting specific features from a certain signal, and then identifying the signal using a classification model. The classification decision is performed by analyzing the probability distribution function (PDF) of feature vectors or minimizing the error between calculated and estimated values. These approaches have the advantages of being a) simple to implement and b) proven to provide near-optimal performance. However, they are sensitive to noise level and/or might require prior information about targeted signals [43]. Cyclostationarity-based and wavelet-based schemes require long observation intervals. The same is true for DL-based algorithms. Additionally, DL

algorithms are highly computationally complex and require increased time to converge. ML-based algorithms require further data preprocessing and rely on expert knowledge for understanding the data structure. Table 3.1 provides a summary of the recent algorithms proposed in the literature, along with the pros and cons of each technique.

The DMD-based algorithms developed in this work differ from the aforementioned techniques and recent studies thereof by two distinguishing features. First, the DMDF and DMD-BW identification techniques' accuracy is independent of SNR. Instead, the algorithm relies on tracking oscillation frequencies for various technologies, while, DMDA algorithm implements power normalization among received signals to reduce its dependence on SNR. Resulting accuracies were above 90%. Second, DMD algorithms were able to track the periodic preamble transmissions within a signal under poor channel conditions, while other algorithms track signal modulation requiring good channel conditions and SNR greater than 0 dB, in most cases, to achieve high accuracy.

Table 3.1. Recent Wireless Technologies Identification Schemes

Model	Cyclostationary-based	CDF-based	ML-based	DL-based
Identified technologies	GSM, LTE, CDMA, WCDMA, OFDM, WLAN, Bluetooth	GSM, LTE, UMTS, CDMA2000	2ASK, 4ASK, QPSK, 2FSK and 4FSK ITS-G5, LTEV2X, NR-V2X, BPSK, MSK, OFDM, IEEE 802.11b/g/n, 802.15.4, 802.15.1, and BLE	GSM, LTE, UMTS, IEEE 802.11a/ac/b/g/n/ax, 802.15.4, 802.15.1, DVB-T, Bluetooth, and ZigBee
Employed features	FFT spectrum, ACF, PSD, SCF, and cyclic frequency	CDF function	High order cumulants, Instantaneous Frequency, SCF, burst length, burst mean power, maximum envelope variation, and ripple	Image representation, IQ samples, RSSI, spectrogram features, power-frequency measurements

Pros	Low implementation cost. Low computational time and complexity	Highly Robust to timing and frequency mismatches. Low computational complexity.	Low implementation cost. Small data sets are sufficient for the algorithm. Low computational time.	Minor data preprocessing is required.
Cons	Affected by noise and SNR variation; require long signal observation time.	Accuracy is highly reduced for signals of SNR <2dB.	Require further data preprocessing and rely on expert knowledge for understanding data structure	High computational complexity, requiring large amounts of data; require long-signal observation time

3.4 Methodology

The DMD data-driven modeling algorithm serves as the foundation for identification schemes created for research reported in this dissertation. Three DMD-based wireless technology identification methods were developed: 1) DMD modes frequency bandwidth-based identification (DMD-BW); 2) DMD mode amplitude-based identification (DMDA); and 3) DMD mode oscillation frequency-based identification (DMDF). These methods identify and distinguish between various wireless technologies coexisting in a heterogeneous network and utilizing the resulted DMD eigenvalues and eigenvectors (i.e., DMD modes). Techniques employ DMD modes' features for identifying the time domain signature of a wireless signal. The proposed algorithms process raw power-measured signals, capturing specifically embedded periodic features within the targeted signals represented in pilot, preamble, synchronization, and control signals. The DMD-BW method uses the frequency spectrum bandwidth of DMD modes, while DMDA utilizes the amplitudes of DMD modes. DMDF, on the other hand, utilizes the slope of the frequency decay of the DMD modes. Each identification methodology was performed in three steps: 1) data formatting (Hankel stacking), 2) extracting DMD modes and eigenvalues by the standard DMD algorithm (Algorithm 3.1), and 3) Classify signals by applying the developed identification schemes.

3.4.1 Data Formatting

All DMD-based identification methodologies developed in this work perform data formatting as a first step in processing the available dataset. Timeseries-raw power signals are prepared as algorithm input during this stage. A mapping procedure, Hankel matrix staking method [31, 77] was used to transform a univariate time series data with length n into a multidimensional matrix of size (m x k). Equation (3.1) describes a time series signal of length n and fixed sampling time Δt:

$$Y = [y_1 \quad y_2 \quad y_3 \quad \cdots\cdots\cdots \quad y_n] \tag{3.1}$$

Data matrix X and its related one-time step evolution data matrix X′ were created using the Hankel matrix stacking approach:

$$X = \begin{bmatrix} y_1 & y_2 & y_3 & \cdots\cdots & y_k \\ y_2 & y_3 & y_4 & \cdots\cdots & y_{k+1} \\ \vdots & \vdots & \vdots & \vdots & \vdots \\ y_m & y_{m+1} & y_{m+2} & \cdots\cdots & y_{m+k-1} \end{bmatrix} \tag{3.2}$$

$$X' = \begin{bmatrix} y_2 & y_3 & \cdots\cdots & y_{k+1} \\ y_3 & y_4 & \cdots\cdots & y_{K+2} \\ \vdots & \vdots & \vdots & \vdots \\ y_{m+1} & y_{m+2} & \cdots\cdots & y_{m+k} \end{bmatrix}, \tag{3.3}$$

such that

$$m = n - k + 1\,, \tag{3.4}$$

where m is the number of stacks. Column vectors of data matrices were defined as snapshots, such that k was the number of snapshots.

$$X = [x_1 \; x_2 \ldots\ldots\ldots x_k] \tag{3.5}$$

$$X' = [x_2 \; x_3 \ldots\ldots\ldots x_{k+1}] \tag{3.6}$$

Figure 3.1 illustrates data formatting steps for GSM positive samples when forming data matrices X and X′, which were utilized by DMD to build a matrix containing GSM signals' captured features. The same steps were applied to LTE training signals. Note that the combination step is a row wise stacking for training signals.

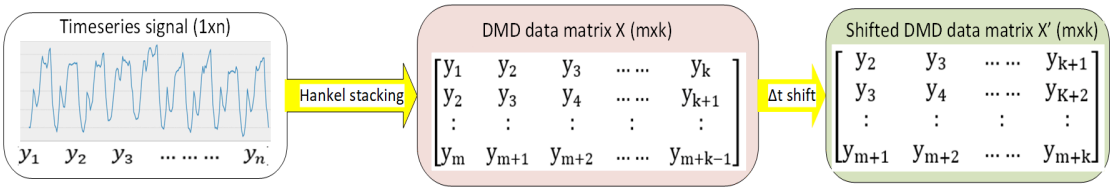

Figure 3.1. DMD data matrix formation using Hankel stacking.

3.4.2 Applying DMD Algorithm

In the second step, the standard DMD algorithm (Algorithm 3.1) was applied to the constructed data matrices X and X. DMD decomposes the data matrices into a DMD mode Φ and DMD eigenvalues Λ.

Algorithm 3.1: Standard DMD Algorithm

Input: signal y_1, k, m, r, and Δt
Output: Φ, Λ, and λi
Perform Hankel stacking:
1: Initialize Y11
2: for j = 1:m do
3: $Y_{11} = [Y_{11}\ y_1(:, j : end - m + j)]$
4: end for
Construct input matrices:
5: $X = Y_{11}(:, 1 : end - 1)$
6: $X' = Y_{11}(:, 2 : end)$
Compute SVD of X:
7: $X = \mathbf{U}\,\mathbf{\Sigma}\,\mathbf{V}^*$
Apply truncation:
8: $\mathbf{U}_r = \mathbf{U}(:, 1 : r)$
9: $\mathbf{\Sigma}_r = \mathbf{\Sigma}(:, 1 : r)$
10: $\mathbf{V}_r = \mathbf{V}(:, 1 : r)$
11: $\tilde{A} = \mathbf{U}_r^* \mathbf{X}'\mathbf{V}_r\ \mathbf{\Sigma}_r^{-1}$
12: $\tilde{A}\,\mathbf{W} = \mathbf{\Lambda}\,\mathbf{W}$
DMD modes matrix
13: $\mathbf{\Phi} = \mathbf{X}'\mathbf{V}_r\,\mathbf{\Sigma}_r^{-1}\mathbf{W}$
DMD eigenvalues
14: $\boldsymbol{\lambda}_r = \boldsymbol{diag}(\mathbf{\Lambda})$
Calculate DMD mode magnitudes:
9: $\boldsymbol{x_1} = \mathbf{X}(:, \mathbf{1})$
10: $\mathbf{mag} = \mathbf{\Phi}^{\dagger}\,\boldsymbol{x_1}$
15: Repeat for all signals

3.4.3 DMD-BW Identification Scheme

The developed DMD-BW technique utilized amplitude-frequency features of the DMD modes (i.e., DMD spectrum) to classify and differentiate between experimentally collected signals of Wi-Fi, Bluetooth, LTE, and GSM wireless technologies. Each wireless technology was associated with a unique DMD modes frequency bandwidth. Figure 3.2 highlights the outline of a DMD-BW identification scheme. Amplitudes of the DMD modes can be calculate as [31]:

$$A = \Phi^{\dagger} x_1 \ , \tag{3.7}$$

where † is the Moore–Penrose pseudoinverse. x_1 is the first-row vector of data matrix X. Oscillation frequency of the ith DMD mode can be defined as [33, 78]:

$$f_i = \left| imag\left(\frac{ln\,(\lambda_i)}{\Delta t}\right) \right| , \tag{3.8}$$

where λ_i is the eigenvalues associated with DMD modes.

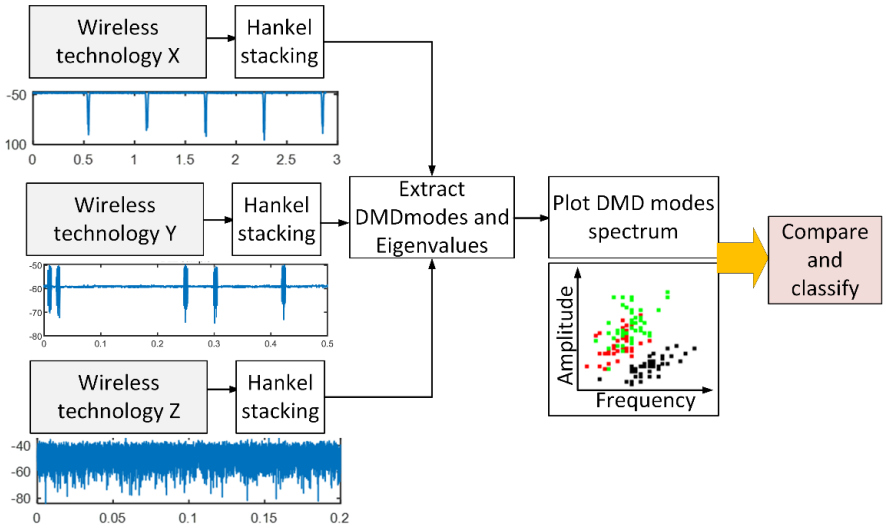

Figure 3.2. Outline of DMD-BW identification scheme.

3.4.4 DMDA Identification Scheme

Utilizing eigenvalue matrix Λ and DMD modes matrix Φ, DMDA technique calculates a template-features matrix F_x from a set of training samples of a certain technology x. As Figure 3.3 illustrates, we projected the features matrix F_x on

testing samples of different technologies, and then the technique classified the signal by evaluating the resultant DMD mode amplitudes. Utilizing the resultant DMD eigenvalues and modes [31, 78], we arrived at the following:

$$x_i = \Phi \Lambda^i b \,, \tag{3.9}$$

where i=1, 2, ..., k, and b are vectors containing the coefficients of the initial condition x_1 in the eigenvector basis, such that:

$$b = \Phi^{\dagger} x_1 \tag{3.10}$$

From Equation (3.9), two terms- Φ and Λ^i —are combined to define a new matrix:

$$F_x = \Phi \Lambda^i \tag{3.11}$$

Matrix F_x contains unique features of a wireless technology x, which is composed of eigenvalues and eigenmodes. This matrix represents a model describing a specific technology class feature in the DMD domain. DMD modes amplitude can be calculated as:

$$b_t = {F_x}^{\dagger} X_t \,. \tag{3.12}$$

Since b is a vector composed of complex values, its amplitude can be represented by:

$$S_t = b_t \, {b_t}^* \,, \tag{3.13}$$

where t represents a testing sample of a wireless technology and ${b_t}^*$ is the complex conjugate of b_t.

The resulting modes' amplitude determines the detected signal class. Given that the signal class includes similar features, subsequent mode amplitude derived from technology x training samples is anticipated to have larger values than other technologies. According to (3.12), power measurements in X_t affect the values of DMD modes amplitude. Therefore, power measurements of various signals should

be at comparable levels. Thus, before using DMDA for classification, signal power must be normalized. This was achieved at a minimum value of zero and a maximum value of one. The pseudo-code of the proposed DMDA technique is given in Algorithm 3.2.

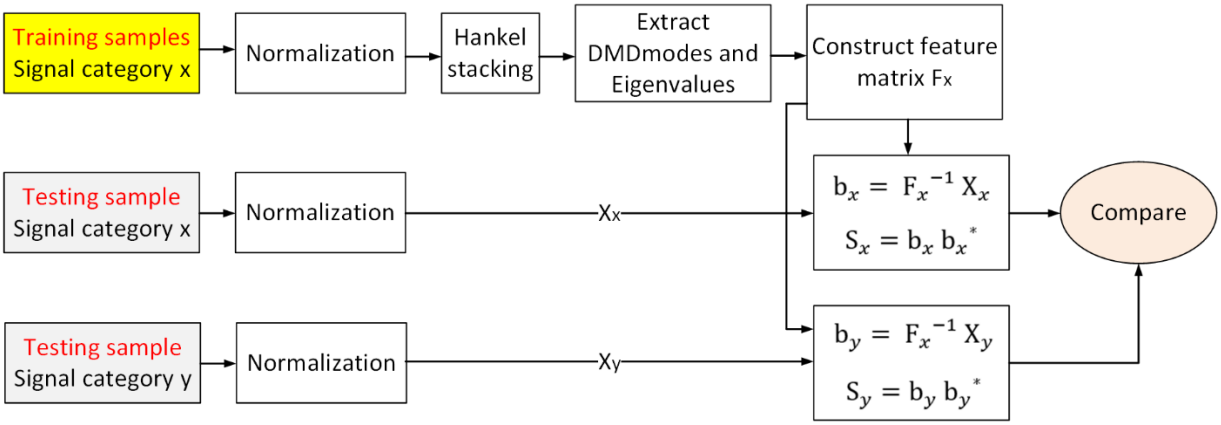

Figure 3.3. Outline of DMDA identification scheme.

Algorithm 3.2: Wireless Signal Features Matrix Formation (Matrix F)

Input: signal y1, k, m, r, and Δt
Output: F
Calculate required number of samples:
1: n = m + k-1
Extract required signal window:
2: $\boldsymbol{Y_1} = \boldsymbol{y_1}(\mathbf{1}:\boldsymbol{n})$
Perform Hankel stacking:
3: Initialize $\boldsymbol{Y_{11}}$
4: for j = 1 : m do
5: $\boldsymbol{Y_{11}} = [\boldsymbol{Y_{11}}, \boldsymbol{Y_{22}}, \ldots . \boldsymbol{Y_{nn}}]$
6: end for
Repeat for all training signals.
Combine to form data matrix:
7: $\boldsymbol{D} = \boldsymbol{y_1}(\mathbf{1}:\boldsymbol{n})$
Construct input matrices for DMD:
8: $\boldsymbol{X} = \boldsymbol{Y_{11}}(:, \mathbf{1}:\boldsymbol{end} - \mathbf{1})$
9: $\boldsymbol{X'} = \boldsymbol{Y_{11}}(:, \mathbf{2}:\boldsymbol{end})$
Apply DMD:
7: X = $\mathbf{U}\,\mathbf{\Sigma}\,\mathbf{V}^*$
8: $\mathbf{U_r}$ = $\mathbf{U}$(:, 1 : r)
9: $\mathbf{\Sigma_r}$ = $\mathbf{\Sigma}$(:, 1 : r)
10: $\mathbf{V_r}$ = $\mathbf{V}$(:, 1 : r)
11: $\tilde{A} = \mathbf{U_r^*}\,\mathbf{X'V_r}\,\mathbf{\Sigma_r^{-1}}$
12: $\tilde{A}\,\mathbf{W} = \mathbf{\Lambda}\,\mathbf{W}$
13: $\mathbf{\Phi} = \mathbf{X'V_r}\,\mathbf{\Sigma_r^{-1}W}$
Construct features matrix:
14: Initialize $\boldsymbol{F}$
15: for j = 1 : k do
16: $\boldsymbol{F} = [\boldsymbol{F}; \mathbf{\Phi\Lambda}^j]$
17: end for
Repeat for all signals

3.4.5 DMDF Identification Scheme

DMDF identification is based on analyzing the resulted DMD modes oscillation frequency for various signals. This was performed after extracting DMD modes matrix Φ and DMD eigenvalues by applying the standard DMD on data matrices X and X' (see Algorithm 3.3). Oscillation frequency of the i^{th} DMD mode was defined in Equation 3.8 [33, 78].

f_i represents the absolute oscillation frequency of a DMD mode. The suggested notion recommends comparing the oscillation trend of signals' DMD modes, which can be accomplished by rearranging the fi values for each signal class into descending order, and then plotting f_i against an index j, where j=1, 2, 3,..., r. The received signal is then classified using the resulting plots. An overview of this procedure can be found in Figure 3.4. To categorize the signals, we used the slope of the ensuing trends. The slope represents the decay of frequencies from extracted DMD modes. Algorithm 3.3 provides a detailed illustration of the suggested technique.

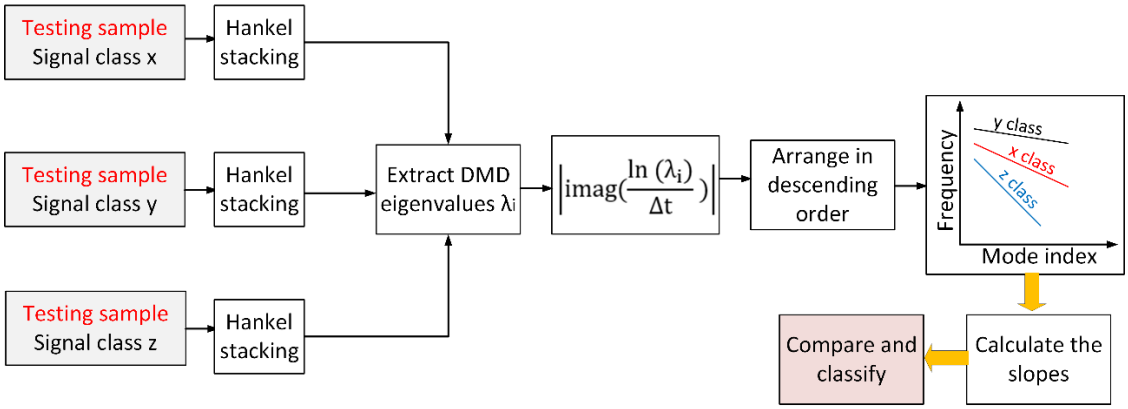

Figure 3.4. Outline of DMDF identification scheme.

Algorithm 3.3: DMDF technique

Input: signal y1, k, m, r, and Δt
Output: figure
Calculate required number of samples:
1: m = n = k-1
Extract required signal window:
2: $\boldsymbol{Y_1} = \boldsymbol{y_1}(\mathbf{1}:\boldsymbol{n})$
Perform Hankel stacking:
3: Initialize $\boldsymbol{Y_{11}}$
4: for j = 1 : m do

5: $\boldsymbol{Y_{11}} = [\boldsymbol{Y_{11}}, \boldsymbol{Y_{22}}, \ldots . \boldsymbol{Y_{nn}}]$
6: end for
Construct input matrices for DMD:
7: $\boldsymbol{X} = \boldsymbol{Y_{11}}(:, \mathbf{1}: \boldsymbol{end} - \mathbf{1})$
8: $\boldsymbol{X'} = \boldsymbol{Y_{11}}(:, \mathbf{2}: \boldsymbol{end})$
Apply DMD:
9: X = $\mathbf{U\,\Sigma\,V}^*$
10: $\mathbf{U}_r$ = $\mathbf{U}$(:, 1 : r)
11: $\mathbf{\Sigma}_r$ = $\mathbf{\Sigma}$(:, 1 : r)
12: $\mathbf{V}_r$ = $\mathbf{V}$(:, 1 : r)
13: $\tilde{A} = \mathbf{U}_r^* \mathbf{X'V}_r\ \mathbf{\Sigma}_r^{-1}$
14: $\tilde{A}\,\mathbf{W} = \mathbf{\Lambda\,W}$
15: $\mathbf{\Phi} = \mathbf{X'V}_r\,\mathbf{\Sigma}_r^{-1}\mathbf{W}$
Calculate eigenvalues and oscillation frequencies:
16: $\boldsymbol{\lambda_i} = \boldsymbol{diag}(\mathbf{\Lambda})$
17: $\mathbf{f_i}$= abs (imag (log ($\boldsymbol{\lambda_i}$/ Δt)))
18: $\mathbf{f_i}$= sort($\mathbf{f_i}$, descend);
Define index j:
19: j=[1:r];
20: figure: Plot (j, $\mathbf{f_i}$)
Repeat for all signals

3.5 Datasets and Experimental Setup

3.5.1 Wi-Fi Dataset

The Wi-Fi dataset used in this work was collected at the wireless laboratory located at the University of Oklahoma Tulsa campus. For signals with maximum throughputs of 956 Mbps, 340 Mbps, and 250 Mbps, the data set included 450 raw power time series measurements containing 90 million packets for 802.11ax, 802.11ac, and 802.11n, respectively. The collection included individual (or baseline) and coexisted signals in the 5 GHz ISM band with a minimum and constant noise level of less than -73 dBm. Three Wi-Fi network setups—each with a pair of access points (Tx) and station (Rx) equipment—were available.

An Asus RT-AX88U device was used To establish an 802.11ax network with 160 MHz of bandwidth on channel 36 (e.g., central frequency 5180 MHz).The device featured Orthogonal Frequency-Division Multiple Access (OFDMA) and 4x4 Multiple User Multiple-Input Multiple-Output (MU-MIMO) technology; it supported single-carrier data rate speeds of 4.8 Gbps on the 5 GHz band with 160 MHz channel bandwidth.

The 802.11n and 802.11ac networks were built using two pairs of Mikrotik Router boards (RB953GS) with R11e-2HPnD radio card boards. During coexistence, the networks shared the same channel with the 802.11ax network. LabVIEW software was used to extract time domain IQ components from raw power measurements of transmitted signals obtained by NI PXIe-5644R RF vector signal transceiver (VST). The platform included the NI PXIe-8133 1.73 GHz Quad-Core PXI Express embedded controller, NI PXIe-1082 8-Slot 3U PXI Express chassis, and VERT2450 antenna. VST is FPGA-based and capable of real-time signal processing and control. Measuring radio frequency (RF) can be broken into acquiring I/Q samples, transferring I/Q samples into a host PC, and performing a proprietary measurement algorithm based on LabVIEW. Real-time bandwidth IQ sampling rate was set to 10 MS/s. Figure 3.5 depicts the time domain properties of randomly selected samples with various duty cycles (DCs) for a 20ms time interval. Table 3.2 shows DC average values.

3.5.2 ZigBee/BLE Dataset

Experimental testing and data collection were conducted at the wireless laboratory at the University of Oklahoma Tulsa campus. A semi-anechoic chamber was used for testing to eliminate external noise. A heterogeneous wireless network was set up andcomposed of BLE and ZigBee subnetworks. The system was characterized by a pair of access points (Tx) and station (Rx) devices in each network. 220 separate (i.e., not sharing a baseline)raw power timeseries signals of each technology were collected, in addition to 220 coexisting signals in the 2.4 GHz ISM band. A CC2530 development kit board was used to create ZigBee traffic via channel 14 at a central frequency of 2.42 GHz. Two laptops equipped with nRF52840-BLE Bluetooth 5.3 chipsets were used for BLE communication. An NI vector network analyzer and PXIe-1075 chassis were used to record the transmitted signals' raw power measurements. Power measurements were gathered using a sampling frequency of 500 MHz. Transmitted signals were

recorded with an SNR range of 0 to 25dB for various transmitter and receiver locations and heights. To summarize, 660 timeseries signals containing 10.3 million packets were captured from three scenarios, namelyindividual BLE, individual ZigBee, and heterogeneous coexisting BLE. and ZigBee, comprised the dataset. For each case, 220 signals (i.e., 3.5 million packets) were collected. Time domain features of randomly selected signals are shown in Figure 3.6.

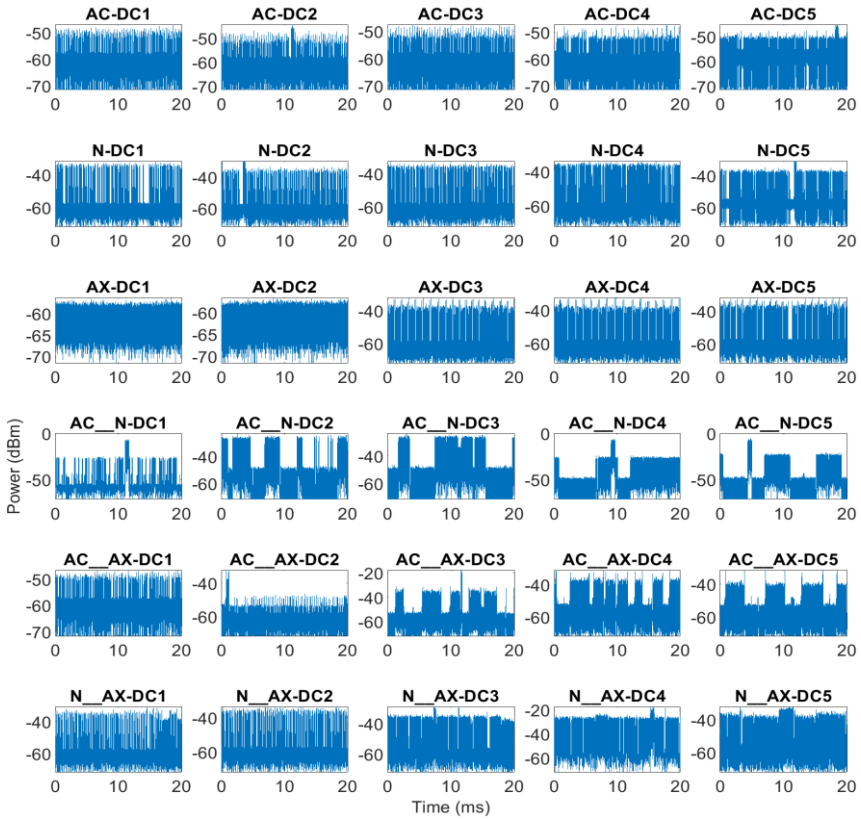

Figure 3.5. Raw power measurements of Wi-Fi signals with various duty cycles.

Table 3.2
Average Values of Wi-Fi Signals Duty Cycles

DC1	DC2	DC3	DC4	DC5
22%	40%	64%	80%	93%

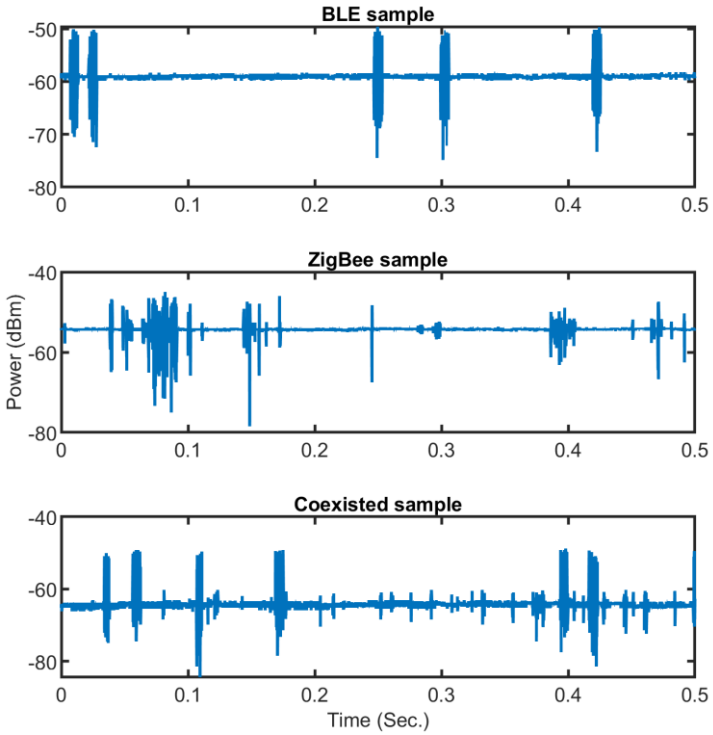

Figure 3.6. Experimentally collected ZigBee and BLE raw power signals.

3.5.3 GSM/LTE Dataset

A GSM and LTE dataset provided by [79] was used and consisted of GSM and LTE signals generated at various SNR levels with a combination of non-line-of-sight (NLOS) and line-of-sight (LOS) conditions. The experiment was performed in the Wireless Research Laboratory in Tubitak, Belgium. Researchers deployed an Agilent vector signal generator (VSG) E4438C as a transmitter. An Agilent PSA series vector signal analyzer (VSA) E4440A was employed as a receiver for capturing transmitted signals. GSM average received signal strengths ranged from -50 dBm to - 45 dBm, while LTE varied between -50 dBm and -40 dBm. Sampling time Δt was set to 0.78 μ s and 0.14 μ s for GSM and LTE, respectively. Figure 3.7 shows various samples of the available time series signals obtained from the dataset.

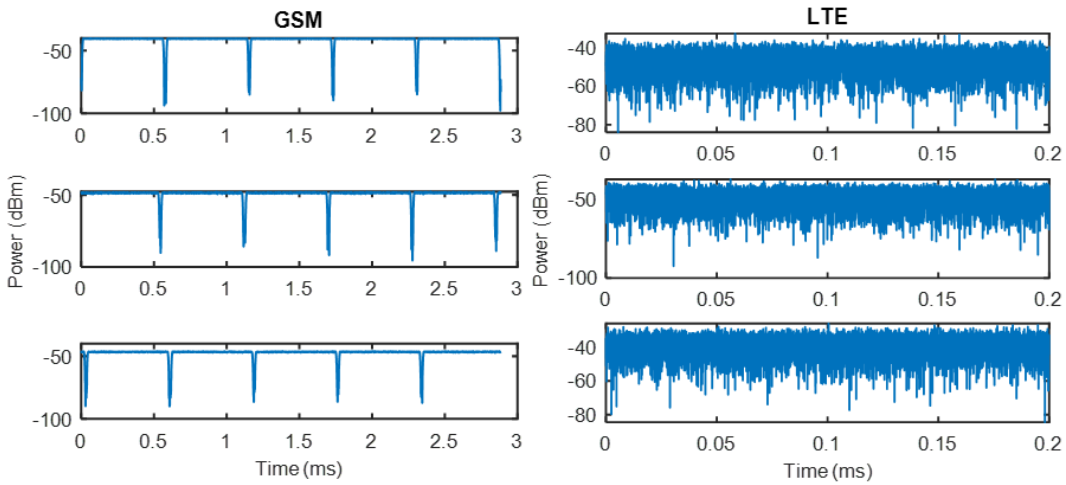

Figure 3.7. Samples of GSM and LTE raw power signals.

3.6 Signal Frame Format and Features

This section explains the signal model and frame structure of various wireless technologies included in the analysis. The inherent unique periodicity in each signal, which serves as the DMD-based algorithms' fundamental property for identification, is highlighted by the frame structure. More specifically, the developed algorithms analyze raw power-measured signals, capturing embedded periodic features within the targeted signals represented in pilot, synchronization, and control signals.

3.6.1 Wi-Fi

When highlighting the physical layer (PHY) frame structure of 802.11n, 802.11ac, and 802.11ax Wi-Fi standard signals in the 5 GHz bands, the 802.11 PHY employs burst packets for transmission. Both a preamble and payload are present in each packet. Preamble enables synchronization of time and frequency; estimates channel parameters for equalization; and gives receiver header details about the packet (e.g., configuration, format type, and data rates). Data from the user is transmitted in the payload.

Figure 3.8 shows packet formats for 802.11n, 802.11ac, and 802.11ax Wi-Fi standard signals. The 802.11n high throughput (HT) mixed format begins with

legacy preambles, including legacy Short Training sequence (L-STF), legacy Long Training sequence (L-LTF), and legacy Signal Description (LSIG), which can be decoded by legacy 11a/g devices. Legacy preambles are followed by the 11n specific HT preambles, and finally the user data. The 802.11ac frame format has the same beginning legacy preambles, followed by very high throughput (VHT) preambles, which are unique for 11ac devices. Like 11n and 11ac, the 802.11ax packet begins with a traditional preamble followed by a high efficiency (HE) preamble sequence that can only be decoded by 11ax devices. At the end of an 802.11ax frame, a packet extension (PE) with length of 8 or 16 μ s can be employed. The proposed DMD-based techniques are based on acquiring these periodic features to differentiate between targeted signals.

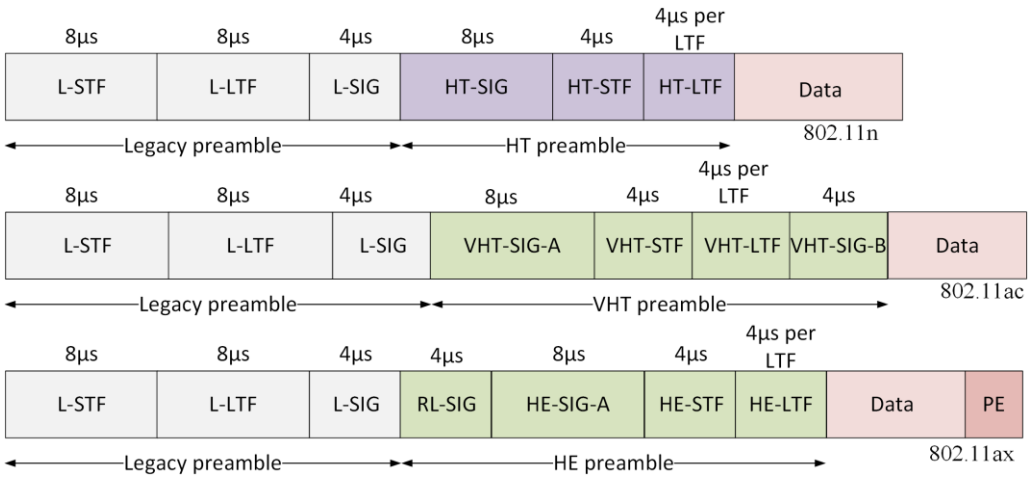

Figure 3.8. 802.11n, 802.11ac, and 802.11ax packet structure.

3.6.2 ZigBee

Data was transmitted via packets by the Zigbee IEEE 802.15.4 PHY. As indicated in Figure 3.9, each packet was composed of a preamble (32 bits) for synchronization; the start of packet delimiter, which is a unique bit sequence that indicates the start of the frame (8 bits); physical header containing information about the frame type; addressing mode; destination and source addresses (8 bits); and payload segment data unit containing actual data being transmitted (0 to 1016 bits) [80]. Figure 3.9 highlights the frame structure of ZigBee IEEE 802.15.4 PHY

and the periodic features within the frame, mainly represented in preamble, delimiter, and header sequences.

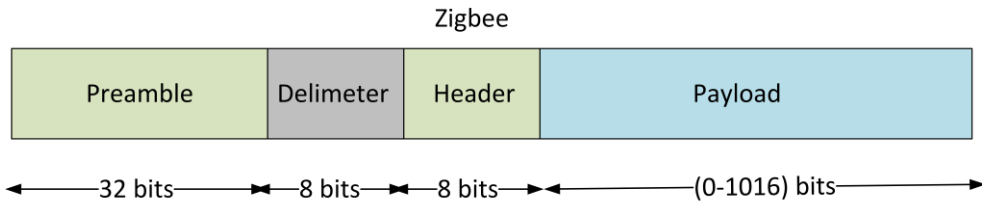

Figure 3.9. ZigBee signal packet structure.

3.6.3 BLE

According to the BLE v5.1 standard created by the Bluetooth SIG, a PHY transmitted packet has four parts: 1) the synchronization preamble (8 bits), 2) access address (32 bits), 3) protocol data unit (PDU)—advertisement or data packet (2-257 octets), and 4) cyclic redundancy check (CRC), which is used to identify packet errors (24 bits) [81]. Figure 3.10 highlights the frame structure of BLE v5.1 signals.

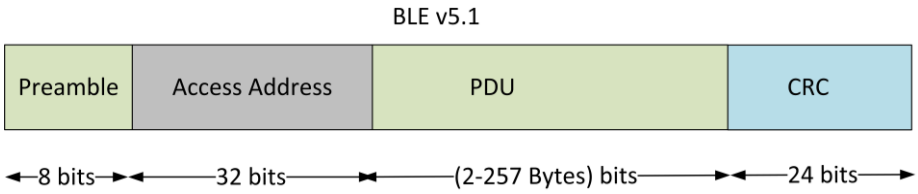

Figure 3.10. BLE v5.1 packet structure.

3.6.4 GSM

GSM frame structure is a time division multiple access (TDMA). Each frame consists of eight timeslots. Figure 3.11 shows timeslot-per-frame for a normal burst of GSM signal [40], which carries encrypted data transmitted between users. Periodicity of the pilot training signals, tail bits (TB), and guard bits (GB) were noted. A dedicated 26 bits for the training (i.e., pilot) signal utilized for channel estimation in each time slot were repeated in the same instance per slot. Since the duration of each timeslot is 577 μ s, the repetitive frequency of the pilot sequence is 1/577=1733 Hz. Guard and tail (i.e., synchronization) bits had the same value of

repetitiveness. Other signaling GSM bursts (i.e., frequency correction, synchronization, and access bursts) have similar repetitive sequences with the same 1733 Hz frequency, yet a different duration.

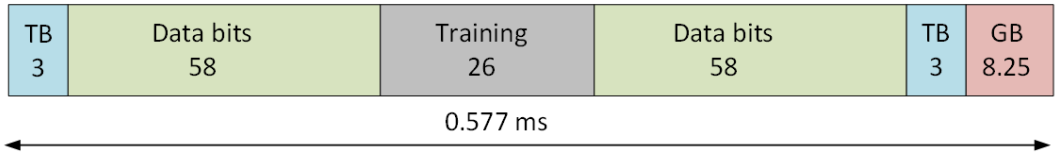

Figure 3.11. GSM timeslot structure for normal burst.

3.6.5 LTE

The detailed frame structure of LTE FDD downlink is avilable in Figure 3.12 [83, 84]. The LTE frame is divided into 10 subframes every 10ms, each with 1ms duration. Also, each subframe contains two timeslots (or resource blocks [RBs]) characterized by 0.5ms duration and six or seven OFDM symbols, depending on short- or long-cyclic prefix. The periodicity of various signals demonstrates a constant repetition for the following.

1. Reference/pilot signals (blue). Fixed location along the time axis on the first and fifth OFDM symbol of each RB. These are repeated once per RB (i.e., one time per 0.5ms),

2. PDCCH, PCFICH, PHICH (yellow, red, purple, respecitviely; see below). Exist at the beginning symbol of each subframe and are repeated once per subframe (i.e., one time per 1ms), and

3. PSS and SSS (green and orange, respecitvely). Repeated at fixed locations once every 5ms,

where PDCCH is Physical Downlink Control Channel; PCFICH is Physical Control Format Indicator Channel; PHICH is Physical HARQ Indicator Channel; PSS is Primary Synchronization Signal; and SSS is Secondary Synchronization Signal.

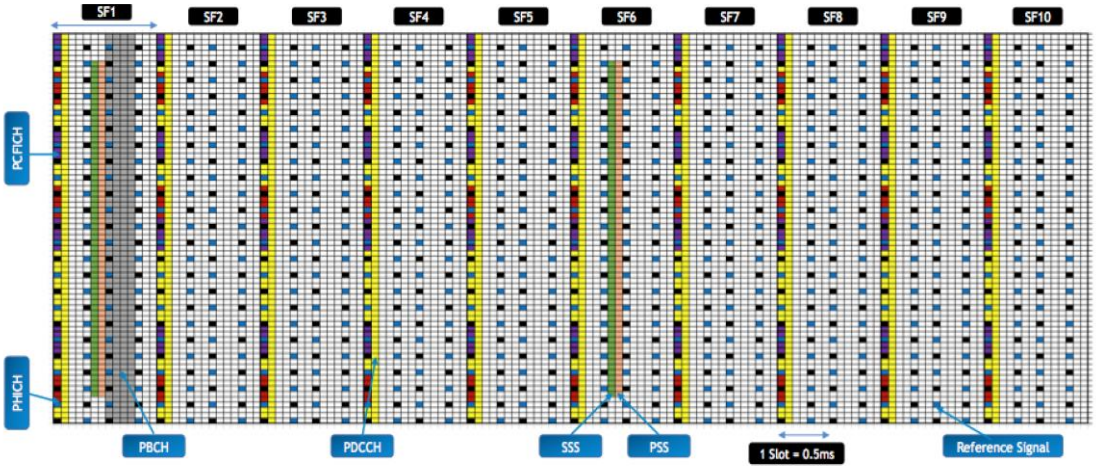

Figure 3.12. LTE FDD downlink frame structure.

3.7 Results and Discussion

3.7.1 Selection of DMD-based identification techniques' input parameters

As shown earlier, algorithms 1, 2, and 3 required four input parameters for carrying out the proposed classification algorithm, as follows.

1. Number of snapshots k. Inputting the entire captured raw signal into the algorithm results in unnecessarily long computational time. Instead, a minimum number of snapshots (i.e., number of column vectors of data matrices) should be used in data matrix X. Based on the discussion in the methodology section, for DMD to accurately capture the periodic features embedded in the signals, one must choose an adequate number of snapshots to represent an ample number of packet timeslots. The following formula was used to calculate the required k value:

$$k = \frac{N_{slot}\, x\, T_{slot}}{\Delta t}, \tag{3.14}$$

where N_{slot} is the number of the standard frame packets and T_{slot} is the duration of each packet. Empirically, it was found that N_{slot} = 4 was sufficient for DMD to capture repetitive sequence frequencies and assign a signal (see subsection 3.72).

2. Number of stacks m for Hankel matrix formulation. The Hankel matrix number of rows m significantly impacts DMD accuracy. The value of m is dependent on the length of the time series signal n. When m was smaller than n/2 or approximate to n, error increased and accuracy decreased. Therefore, the value of m follows the threshold [33, 78]:

$$\frac{n}{2} < m < n \tag{3.15}$$

The value of m was selected to be approximately 60% of the value of n:

$$m = 0.6\, n \tag{3.16}$$

3. Truncation value r. The optimal value of r can be found from the inflection point in the decay of the singular values of data matrix X [33], which are elements of the diagonal matrix Σ of the SVD process. For example, Figures 3.13 and 3.14 indicate the decay of the singular values of GSM signal. Singular values were normalized with respect to the first singular value. Based on the inflection point, six modes are ample to represent a GSM signal. This result confirms the significance of DMD, which required only a few numbers of extracted (i.e., dominant) modes for identifying a signal.

4. Number of samples n. This parameter represents the length of the timeseries signal, as indicated in (3.1). The value of n can be calculated using (3.4), given the value of m and k, as calculated in (3.14) and (3.16).

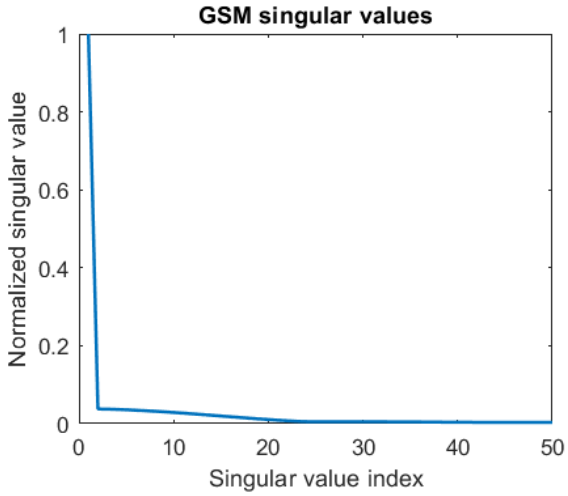

Figure 3.13. Decay of GSM signals singular values.

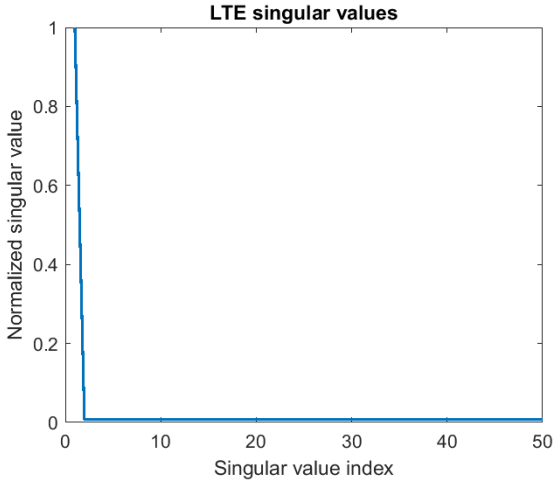

Figure 3.14. Decay of LTE signals singular values

3.7.2 GSM/LTE Identification

3.7.2.1 Applying DMD-BW Technique

The developed DMD-BW identification technique (see Figure 3.2) was applied to raw power timeseries signals of GSM and LTE signals. The technique differentiated/classified the targeted wireless technologies based on their DMD spectrum characteristics. It was found that each technology has its unique DMD spectrum. Figure 3.15 shows a sample of the resulted DMD spectrum for the

targeted technologies (i.e., DMD modes' amplitude versus their frequencies). Each wireless technology was associated with a unique DMD modes frequency bandwidth.

LTE signals had higher DMD spectrum bandwidth compared to GSM. As Figures 3.11 and 3.12 demonstrated, the frequencies of the periodic sequences of LTE- transmitted packets have the highest throughput, while GSM had the lowest (i.e., 9.6 kbps). Higher throughput means shorter transmission time and, consequently, higher periodic frequencies. The identification rule was empirically developed and expressed as:

$$BW_{LTE} > BW_{GSM}\ , \tag{3.17}$$

where BW_{LTE} and BW_{GSM} are the DMD modes' frequency spectrum bandwidth for LTE and GSM wireless technologies, respectively.

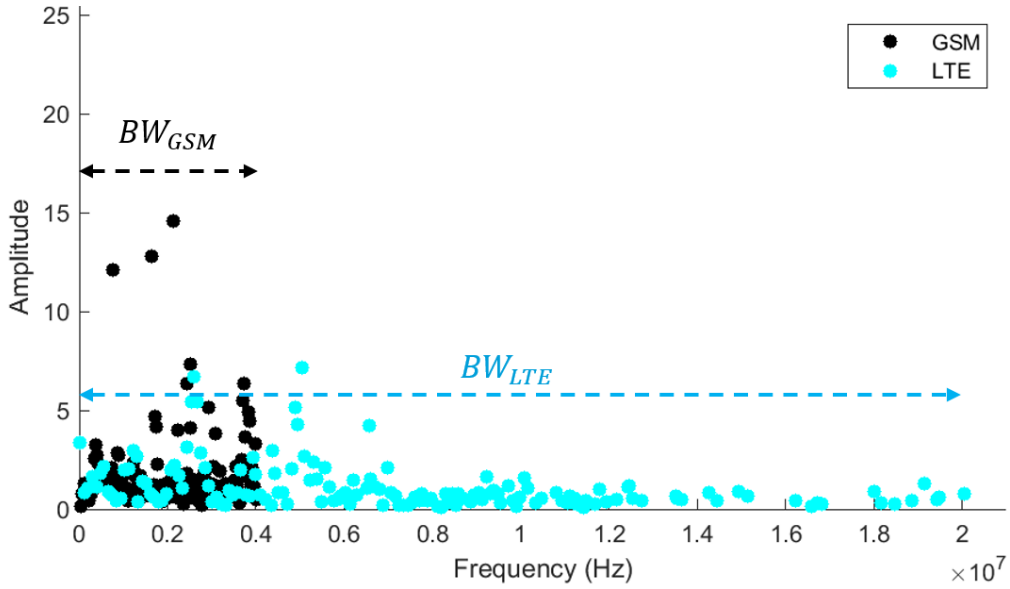

Figure 3.15. DMD frequency spectrum for a sample of LTE and GSM signals.

3.7.2.2 Applying DMDA Technique

This section describes results obtained using DMDA signal identification. DMDA evaluates the resultant DMD mode amplitudes. Figure 3.16 shows the resulting modes of two GSM and LTE testing samples for a various number of transmitted

timeslots (or packets) N_{slot}. The developed algorithm achieved better distinction as N_{slot} increased. Six resultant DMD mode amplitudes of GSM and LTE test samples were evaluated relative to features stored in matrix F, which was constructed using GSM training signals (see Figure 3.3). DMD mode amplitudes were evaluated by comparing maximum and average values. As expected, GSM test samples had higher amplitudes than LTE test samples due to common features matching with matrix F. Results confirm the ability of DMDA to identify signals with short time duration (i.e., only 4 packets/timeslots are sufficient). Regarding GSM, N_{slot} = 4 was empirically found to sufficiently capture the repetitive sequence frequency, as clearly shown in Figure 3.14. Given T_{slot} = 577 μ s and Δt = 0.78 μ s, k equals approximately 2950. For LTE, N_{slot} = 5 was empirically found to capture repetitive sequence frequencies. Given T_{slot} = 0.5ms and Δt = 0.14 μ s, k equals approximately 17850.

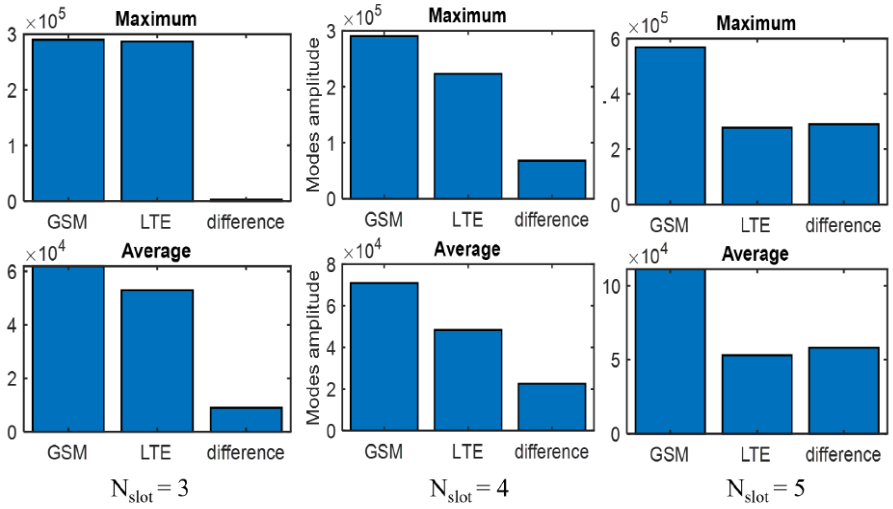

Figure 3.16. Resulted DMD modes amplitudes for testing samples with different values of N_{slot}.

3.7.2.3 Applying DMDF Technique

The DMDF identification method classifies signals based on evaluating the slope of DMD mode oscillation frequencies, as explained in Section 3.4.5. The technique was applied on all the available GSM and LTE samples, and then plotted the oscillation frequency trend for 20 modes (i.e., value of r was set to 40, and then

duplicate values were removed, as resultant eigenvalues were complex conjugates).

Figure 3.17 shows that LTE testing samples had a more pronounced, distinct trend (e.g., higher slope) than GSM testing samples. Figure 3.17 also demonstrates that only one GSM signal could potentially be misclassified. When observing this signal, it is obvious that the signal contained a high amount of noise when compared with other signals, which affected algorithm accuracy. The absolute value of slope α of the linearly fitted line for modes oscillation frequencies was utilized for identifying each signal class. The identification rule was developed as:

$$\alpha_{LTE} > \alpha_{GSM}\ , \tag{3.18}$$

where α_{LTE} and α_{GSM} are the absolute values of slope of the linearly fitted line for modes and their associated oscillation frequencies of LTE and GSM signals, respectively.

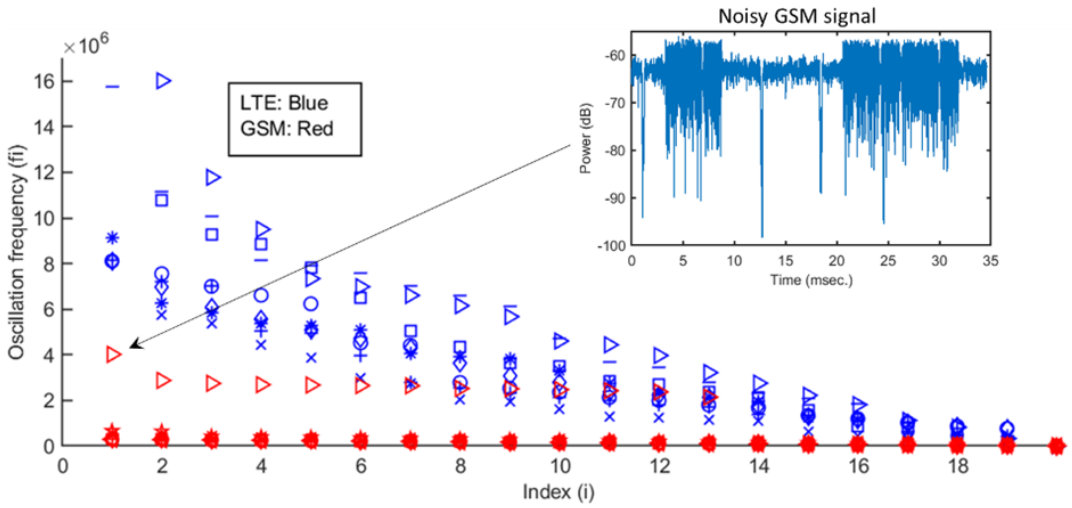

Figure 3.17. Oscillation frequency for LTE and GSM signals arranged in descending order.

3.7.3 Wi-Fi Standard Technology Identification

Classification was performed on both individual (or baseline) and various coexistence scenarios of 802.11n, 802.11ac, and 802.11ax Wi-Fi standard signals

in the 5 GHz ISM band. Processed time series raw power signals were collected in a shared heterogeneous deployment.

3.7.3.1 Individual signals Identification employing DMDA.

DMDA technique was applied for classifying/differentiating between individual (or baseline) 802.11n, 802.11ac, and 802.11ax Wi-Fi standard signals in the 5 GHz ISM band. Classified signals had the same duty cycle. In the available dataset, each technology contained 25 individual signals divided into five groups. Each group contained five signals having a specific duty cycle (see Table 3.2). In Figure 3.18, six resultant DMD mode amplitudes were evaluated for three random testing samples, regarding features stored in the 802.11ac feature matrix F_{ac}. Mode amplitudes were evaluated by comparing maximum and average values. Figure 3.18 indicates that the DMDA technique could clearly differentiate between the targeted signals. The 802.11ac signals had the highest amplitudes due to common features matching the feature matrix F_{ac}. The 802.11n signals had lower amplitude than 802.11ac, while the 802.11ax signals had the lowest amplitude. The identification rule was empirically developed and expressed as:

$$S_{ac} > S_n > S_{ax}\ , \tag{3.19}$$

where S_{ac}, S_n, and S_{ax} are the maximum mode amplitude for Wi-Fi-802.11ac, 802.11n, and 802.11ax signals, respectively.

3.7.3.2 Individual signals Identification employing DMDF.

When applying DMDF on the same dataset for each signal, the oscillation frequencies were plotted for 16 modes. Figure 3.19 shows the resulting modes oscillation frequencies of a randomly chosen signal for each duty cycle. More specifically, the absolute value of slope α of the linearly fitted line for modes oscillation frequencies (or dashed line) was utilized for identifying each signal

category. As Figure 3.19 indicates, the identification rule for all duty cycles can be defined as:

$$\alpha_{ac} > \alpha_n > \alpha_{ax} \ , \tag{3.20}$$

where α_{ac}, α_n, and α_{ax} are the absolute value of slope from the linearly fitted line for modes oscillation frequencies of Wi-Fi-802.11ac, 802.11n, and 802.11ax signals, respectively. This result indicated that the DMDF technique can extract unique features and accurately classify targeted signals.

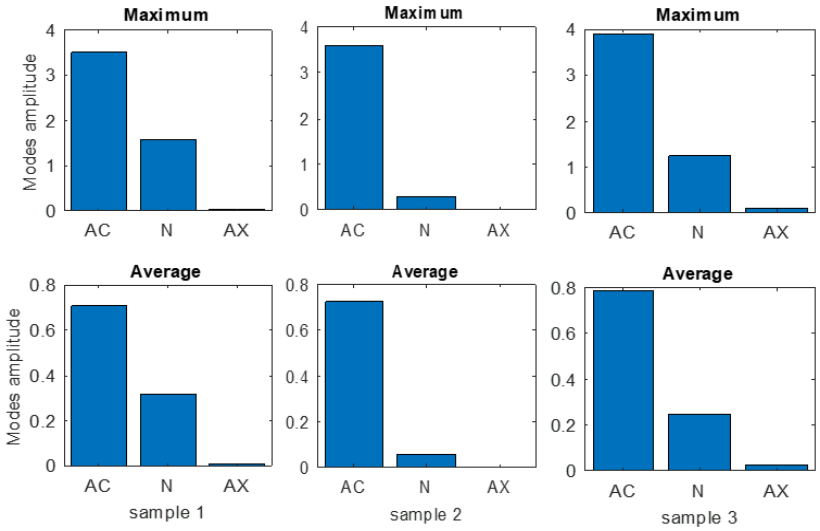

Figure 3.18. Individual Wi-Fi signals identification employing DMDA.

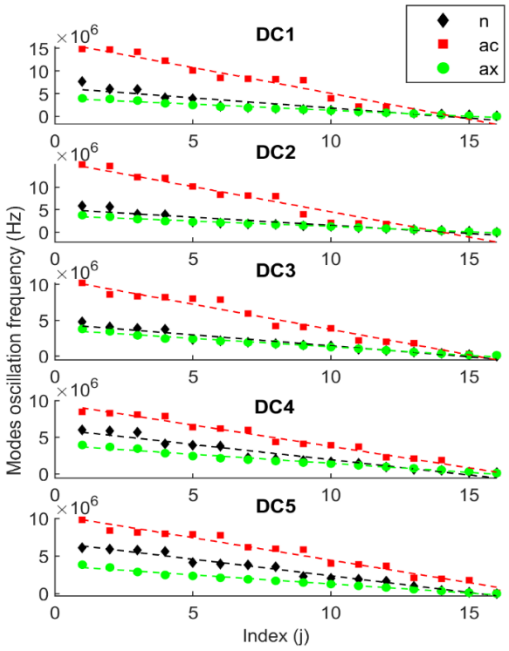

Figure 3.19. Individual Wi-Fi signals identification employing DMDF.

Conversely, the DMD-BW identification scheme was not able to differentiate/classify the signals as they had similar DMD frequency spectrum bandwidth without an ample separating margin for accurate classification.

3.7.3.3 Coexisting Signals Identification

Five coexistence scenarios were created, each coexisting two Wi-Fi signals having the same duty cycle. Each scenario was repeated according to duty cycles provided in Table 3.2. A DMDF technique was applied to differentiate between coexisting signals and individual signals of the same Wi-Fi technology. Figures 3.20, 3.21, and 3.22 compared the resulting modes oscillation frequencies of a randomly chosen signal from each coexistence scenario with individual signals having the same duty cycle. The slope of the linearly fitted line for modes oscillation frequencies (see dashed line) demonstrates that the coexisted signal has the lowest slope of all cases. Alternatively, DMDA was able to classify ac, n, and coexisted ac-n signals; however, it was not able to differentiate between ax and coexisted signals containing ax (e.g., coexisted ax-ac and ax-n signals), as they had similar amplitude values without an adequate separating margin for accurate classification.

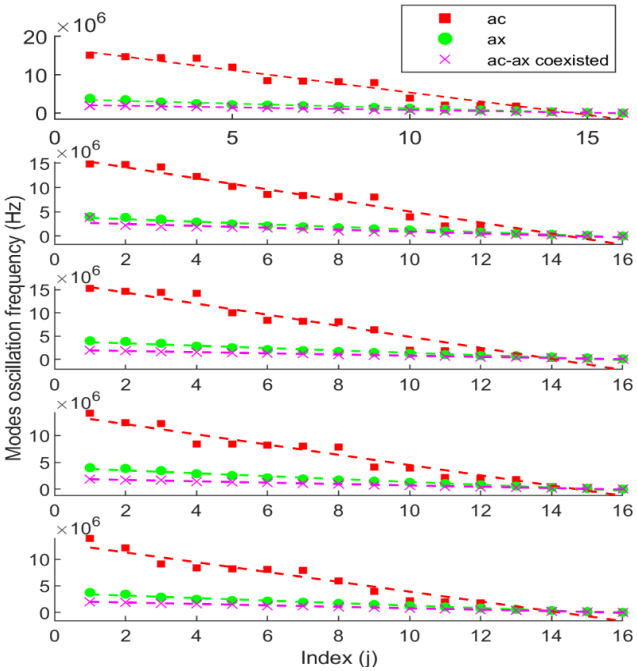

Figure 3.20. Identifying coexisted ac-ax Wi-Fi signals employing DMDF.

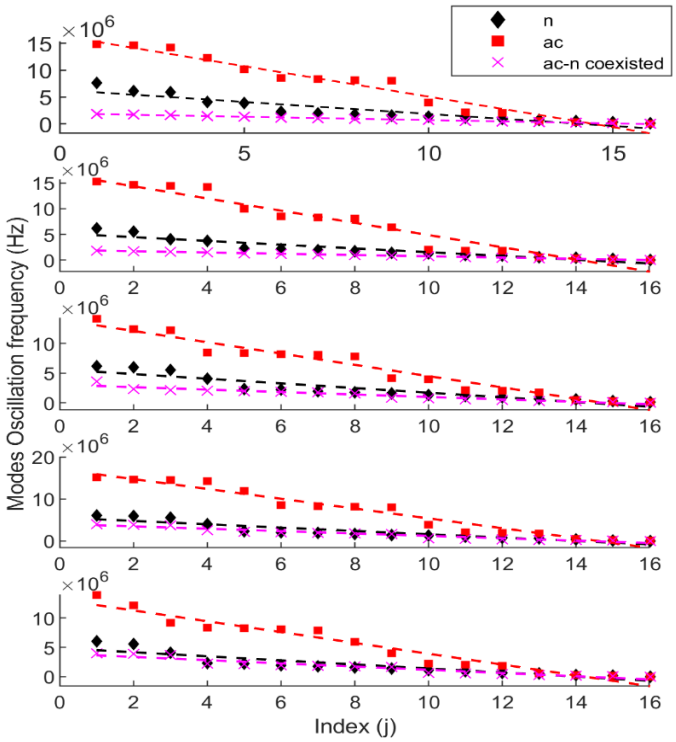

Figure 3.21. Identifying coexisted ac-n Wi-Fi signals employing DMDF.

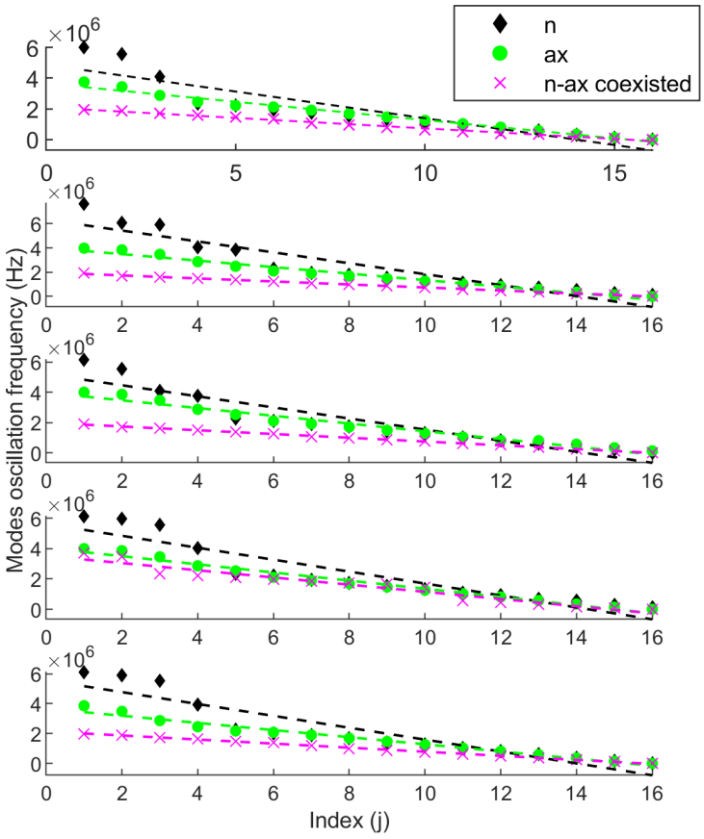

Figure 3.22. Identifying coexisted ax-n Wi-Fi signals employing DMDF.

3.7.4 ZigBee/BLE Identification

The developed DMD-based techniques were proposed to classify individual (i.e., non-sharing baseline) and coexistence scenarios for experimentally collected BLE and Zigbee signals in a shared heterogeneous deployment in the 2.4 GHz ISM band.

3.7.4.1 Applying DMD-BW Technique

The developed DMD-BW identification technique was applied to raw power timeseries signals of BLE and ZigBee. The technique differentiated/classified the targeted wireless technologies based on their DMD frequency spectrum bandwidth. It was found that each technology was associated with a unique DMD modes frequency bandwidth. Figure 3.23 shows a sample of resulted DMD spectrum for the targeted technologies (i.e., DMD modes' amplitude versus their frequencies). BLE signals had higher DMD spectrum bandwidth. An identification rule was empirically developed and expressed as:

$$BW_{BLE} > BW_{Zig.}, \tag{3.21}$$

Where BW_{BLE} and BW_{zig} are the DMD modes' frequency spectrum bandwidth for BLE and ZigBee wireless technologies, respectively.

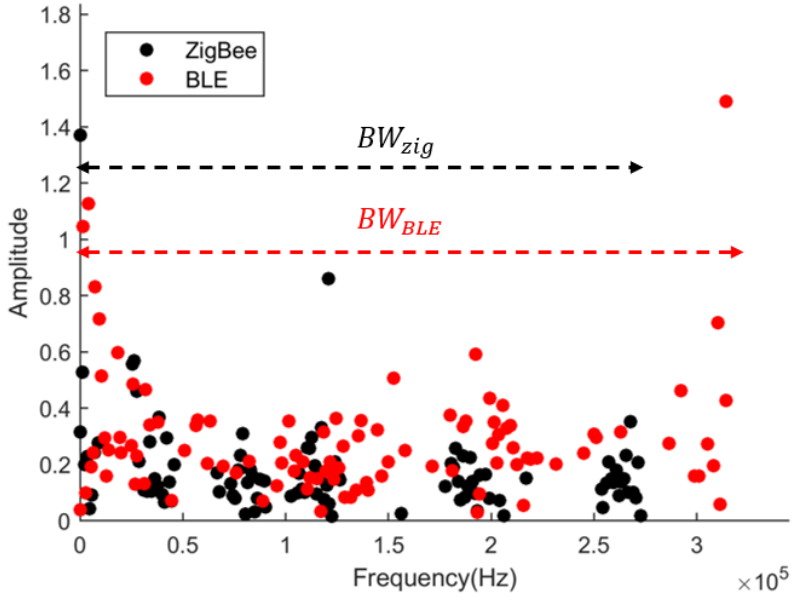

Figure 3.23. DMD frequency spectrum for a sample of LTE and GSM signals.

3.7.4.2 Applying DMDA Technique

In Figure 3.24, six resultant DMD mode amplitudes were evaluated for three random testing samples with regard to features stored in the Zigbee feature matrix F_{Zig}. Mode amplitudes were evaluated by comparing maximum and average values. Figure 3.24 indicates that DMDA technique was able to clearly differentiate between the targeted signals. As expected, ZigBee test samples had the highest amplitudes due to common features with F_{Zig}. BLE test signals had lower amplitude than ZigBee; the coexisted signal had the lowest amplitude. The identification rule was empirically developed and expressed as:

$$S_{Zig} > S_{BLE} > S_{co} \ , \tag{3.22}$$

where S_{Zig}, S_{BLE}, and S_{co} are the maximum mode amplitude for ZigBee, BLE, and coexisted ZigBee/BLE signals, respectively.

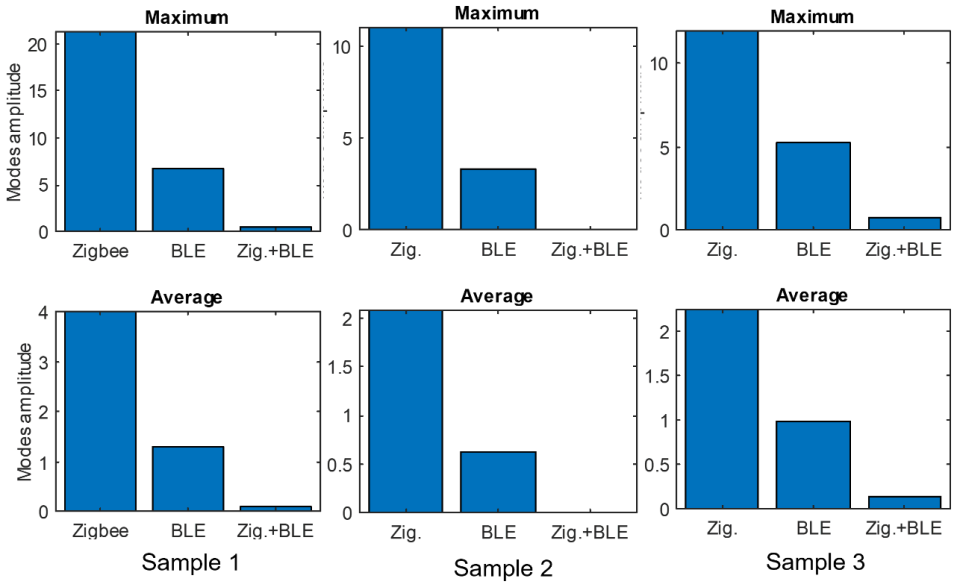

Figure 3.24. ZigBee-BLE identification employing DMDA scheme.

3.7.4.3 Applying DMDF Technique

Figure 3.25 shows the oscillation frequency trend for 10 unique DMD modes of two randomly chosen dataset samples. Each technology had a pronounced,

distinct trend (i.e., slope). The identification rule was empirically developed and expressed as:

$$\alpha_{zig} > \alpha_{BLE} > \alpha_{co} \ , \tag{3.23}$$

where α_{ac}, α_{n}, and α_{ax} are the absolute value of slope from the linearly fitted line for modes oscillation frequencies ZigBee, BLE, and coexisted ZigBee/BLE signals, respectively.

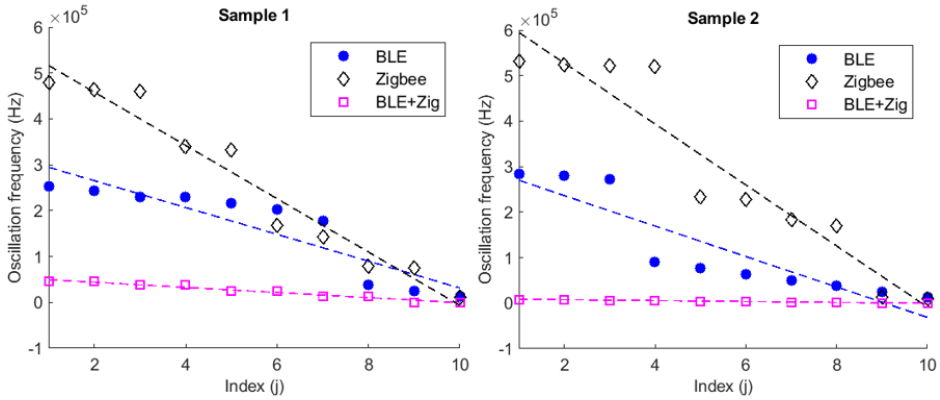

Figure 3.25. ZigBee-BLE identification employing DMDF scheme.

3.8 Evaluating Performance of Developed Techniques

3.8.1 GSM/LTE Identification

The performance of the developed DMD-based techniques was evaluated leveraging classification accuracy and processing time required to classify a signal.

DMD-BW technique classified the signals by thresholding the value of DMD modes frequency bandwidth. The selected thresholding values are indicated in Table 3.3. The technique correctly classified signals with a high overall accuracy of 95%. Classification accuracy of GSM and LTE was 95% and 100%, respectively. The processing time required to identify a signal was approximately 1.5 seconds.

Concerning DMDA, signals were classified by comparing the maximum value of DMD modes amplitude, as indicated in Figure 3.16. GSM signals had higher modes amplitude than LTE signals. Classification accuracy of both GSM and LTE was 90%.

The processing time required to identify a signal was approximately 1.5 seconds. The time required to train the DMDA model with four GSM signals was approximately 20 seconds.

By employing a DMDF scheme—where GSM acquires lower slope than that of LTE—the DMDF technique achieved 90% accurate detection for GSM and 100% for LTE. The DMDF technique required no training and only 3 seconds to identify a signal.

The developed techniques were compared to [42], which utilized second-order cyclostationarity to calculate spectral correlation functions (SCFs). Resulting SCFs were utilized as an input to SVM for classifying various signals, including GSM and LTE. The method achieved 78% accurate detection for GSM and 100% for LTE signals. In addition, the techniques' performance was compared with [52, 53], which distinguished GSM signals from LTE signals by applying CDF analysis using the same dataset used in the analysis reported herein. The magnitude of GSM signals follows a Rician distribution, while the magnitude of LTE signals follows a Rayleigh distribution. Using a distribution fitting the MATLAB tool and a CDF calculation, GSM and LTE were classified based on their respective CDFs. Results achieved 80% accurate detection for GSM and 70 %n for LTE. Table 3.4 provides a comprehensive summary of the overall classification accuracy for the compared techniques.

Specific baseline methods were selected for evaluation and comparison due to their relevance in approach and recency to the developed DMD-based methods. Specifically, cyclostationary methods track the periodicity of pilot signals embedded in their transmission. Although this approach is similar to the developed methods, the one proposed in this dissertation requires fewer samples with less complexity for facilitating accurate identification.

Table 3.3
DMD Modes' Frequency Bandwidth Threshold Values Used for GSM/LTE Classification

Threshold (MHz)	class
BW < 6	GSM
BW > 10	LTE

Table 3.4
GSM/LTE Classification Models Accuracy

Identification Technique	DMD-BW	DMDA	DMDF	Cyclostationarity	CDF
Overall Accuracy	95%	90%	95%	89%	75%
Processing time	1 sec	1 sec	2 sec	5 sec	1 sec
Training time	No training	1 min.	No training	No training	No training

3.8.2 Wi-Fi 802.11n/ac/ax classification

DMDA classified the signals by thresholding the maximum value of DMD modes amplitude. DMDF classified the signals by thresholding the values of slopes. Selected thresholding values are indicated in Table 3.5.

Regarding individual signals classification, the DMDA technique correctly classified ac signals with 84% accuracy, n signals with 88% accuracy, and ax signals with 92% accuracy. DMDF achieved superior accuracy, correctly classifying signals with an overall accuracy of 98.6 %. DMDF classification accuracy of n, ac, and ax signals was 96%, 100%, and 100%, respectively.

When classifying individual and coexisted signals of the same technology (as Figures 3.20, 3.21, and 3.22 indicate), DMDF technique achieved 93.3% accuracy for classifying n, ac, and coexisted n-ac signals; 93.3% for classifying n, ax, and coexisted n-ax signals; and 97.3% for classifying ax, ac, and coexisted ax-ac signals. DMDA was able to classify n, ac, and coexisted n-ac signals with 82% accuracy.

CNN, ResNet, and WaveNet are indicative of recently studied and published deep learning architectures used for wireless signal identification. These

approaches are somewhat relevant to our developed algorithms since data training and model development are part of both approaches. As such, we selected the aforementioned models to compare and evaluate the developed DMD-based techniques. Comparing results with the WaveNet DL model utilized in [61], researchers achieved lower classification accuracies of 96%, 98%, and 98% for n, ac, and ax individua signals, respectively. For coexisted signals, the [61] technique achieved 90% accuracy for classifying coexisted ax-n and 91% for coexisted ax-ac signals. The DMDF technique proposed in this work not only achieved higher accuracy, alsocomputational time was extensively reduced by approximately 85%.

In addition, a developed CNN architecture and ResNet9 CNN model [85] were trained to classify the collected signals. Gramian angular summation field (GASF) transformation [86] was used to extract features. GASF was utilized to encode the collected, one-dimensional (1D) raw power timeseries signals into two-dimensional (2D) texture images for inputting into CNN classifier models. Generated images were 300x300 pixels. Because signal power measurements are distinct and to alleviate the effect of diverse SNR values between technologies, a preprocessing normalization step was performed on signals before applying the transformation. Training was conducted on 50% of the dataset for both individual and coexisting scenarios with batch size of eight images, using a cross-entropy loss function along with an Adagrad optimizer [87]. The learning rate was set to 0.001. Models were implemented, trained, and tested in the open-source Pytorch software library. The developed CNN was structured with six transformation layers, and the network was convolutional with batch normalization and ReLU activation layers, a pooling layer, and dense fully connected (FC) layers. The final FC layer was the output layer, which computed scores for each of the three class labels. The label with the highest score was the one predicted by the model. Figure 3.26 depicts the complete structure and Kernel filter sizes K of the developed CNN network.

Table 3.6 shows the evaluation and comparison of model performance in terms of overall classification accuracy, processing time required to identify a signal, and model training time. For CNN models, the best accuracy was attained for 50 epochs. It should be noted that CNN models are expected to have higher accuracy for larger training samples when compared with the sample trained and reported herein. However, these results are at the expense of additional time required to train the models.

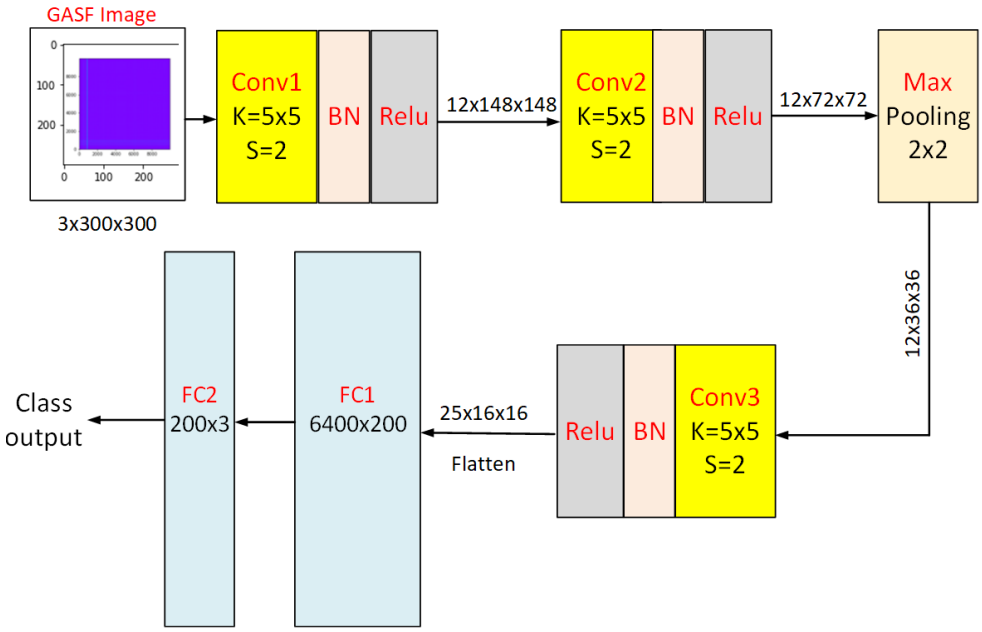

Figure 3.26. CNN network developed for classifying wireless signals.

Table 3.5
DMD Modes' Frequency Bandwidth Threshold Values
Used for ZigBee/BLE Classification

DMDA threshold	DMDF threshold	Class
S < 0.1	220,000 < α < 280,000	ax
0.1 < S < 1.5	280,000 < α < 550,000	n
S > 1.5	α > 550,000	ac
-	α < 220,000	Coexisting signal

Table 3.6
Performance Evaluation for Various Implemented Models to Classify Wi-Fi Signals

Model	Overall accuracy (individual)	Overall accuracy (coexistence)	Processing time	Training time
DMDA	88%	82%	0.5 sec.	1 min.
DMDF	98.6%	94.6%	3 sec.	No training required
WaveNet	97.3%	91%	0.4 sec.	14 hrs
CNN	71%	70%	2 sec.	6 min.
ResNet9	80%	78%	2.5 sec.	20 min.

3.8.3 ZigBee/BLE Classification

DMD-BW technique classified the signals by thresholding the value of DMD modes frequency bandwidth. The selected thresholding values are indicated in Table 3.7. The technique correctly classified signals with an overall accuracy of 85%. Classification accuracy of ZigBee and BLE was 78% and 92%, respectively. The processing time required to identify a signal was approximately 1.3 seconds.

Concerning DMDA, signals were classified by thresholding the maximum value of DMD modes amplitude, as indicated in Table 3.8. The technique correctly classified signals with an overall accuracy of 86.3%. Classification accuracy of ZigBee, BLE, and coexisted signals was 86%, 81%, and 91%, respectively.

Applying DMDF scheme, signals were classified by thresholding values of the slopes, as indicated in Table 3.8. DMDF achieved an overall classification accuracy of 87.6%. Classification accuracy of ZigBee, BLE, and coexisted signals was 91%, 85.5%, and 86.4%, respectively.

The performance of DMD-BW, DMDA, and DMDF techniques were evaluated using overall classification accuracy, processing time required to identify a signal, and model training time. Both techniques were compared with the developed CNN model and ResNet-9 model for validation (see subsection B). CNN-based models

training was conducted on 50% of the dataset with a batch size of eight images, using a cross-entropy loss function along with an Adagrad optimizer. The learning rate was set to 0.001. Model accuracy was calculated using the same set of testing samples. Table 3.8 provides a comparison of implemented model performance. Results showed that the developed DMD-based techniques achieved high performance for classifying various individual and coexisting wireless signals. In most cases analyzed during and compared for this work, DMD-based techniques had the advantage of high accuracy and short training/processing time required to identify a signal. The DMDF scheme outperformed all compared techniques and did not require training. DMDF also achieved the highest accuracy and shortest processing time for identifying a signal.

Table 3.7
DMD Modes' Frequency Bandwidth Threshold Values
Used for ZigBee/BLE Classification

DMD-BW threshold	DMDA threshold	DMDF threshold	Class
BW ≤ 28	10 < S < 30	33,000 < α < 70,000	ZigBee
BW > 28	2 < S < 8	11,000 < α < 31,000	BLE
-	0.01 < S < 1	900 < α < 9,000	Coexisting signal

Table 3.8
Performance Evaluation for Various Implemented Models to
Classify ZigBee and BLE signals

Model	Overall accuracy	Processing time	Training time
DMD-BW	85%	1.3 sec.	No training required
DMDA	86.3%	0.5 sec.	1 min.
DMDF	87.6%	3 sec.	No training required
CNN	72%	2.1 sec.	12 min.
ResNet9	80%	2.5 sec.	40 min.

3.9 Computational Complexity

Four algorithms (e.g., CNN, ResNet, WaveNet, and cyclostationary) were implemented to confirm the computational advantage of this work's developed techniques over others. DMD-based techniques' computational complexity is attributed to the SVD calculation [31]. Notably, the proposed algorithm was successfully implemented using a truncated SVD solution. Doing so limited its complexity to $O(rn^2)$. Truncation value r was less than 10, and n was limited to less than five wireless packet samples. However, the implemented three-layer CNN model complexity was $O(knd^2)$ per convolutional layer, where d is the layer dimension [88]. Furthermore, the implemented nine-layer ResNet complexity was $O(knd^2)$ per layer. The implemented WaveNet had a very high exponential complexity $O(2^L)$, where L is the number of layers of the network (i.e., large number) [89]. Finally, cyclostationary complexity was $O(2n[4 + 2\log2h + 4n + 2h + h\log2(4n/h)])$, where h is the FFT number of points [37]. In comparison, the approach developed for this dissertation required fewer signal samples and achieved higher accuracy with less computational time, as demonstrated in Tables 3.4, 3.6, and 3.8.

3.10 Conclusion

Three novel techniques for wireless technology identification—the first to employ a DMD algorithm for identifying signals—were explained in this chapter. The DMD-BW technique identifies signals by evaluating the values of the resulting DMD modes' frequency spectrum bandwidth. The DMDA technique is based on evaluating a template-features matrix obtained for a specific signal class, and then classifying signals under evaluation according to the values of the resulting projected DMD mode amplitude. The DMDF technique classifies signals based on evaluating the slope of the DMD modes oscillation frequency trend. The proposed techniques were implemented on experimental datasets captured under various channel conditions. When compared with various similar techniques

implemented in the literature, results showed that DMD-based algorithms had lower complexity and achieved higher performance. The developed algorithms can differentiate and classify wireless signals with high accuracy by employing short observation intervals (e.g., four-time slots or packets), which enable them to be implemented in real-time for identifying various operating wireless technologies coexisting in heterogeneous networks. The DMDF scheme outperformed all compared techniques, as it is a direct identification scheme (i.e., no training required). This technique achieved the highest accuracy—greater than 90% for most cases—in the shortest time—less than one second—required to identify a signal. The proposed DMD-based identification algorithms showed promising performance in accurately identifying three wireless technologies simultaneously operating in the same environment.

Chapter 4 CIPN identification employing DMD

4.1 Background

According to [90], more than 50% of newly diagnosed cancer cases are adults aged 60 and above. Researchers in [91] predict that the incidence of cancer among older adults will increase by 67% by 2030. Elderly cancer patients are at a high risk of developing toxicities associated with chemotherapy, with over 50% of patients over age 60 experiencing severe, disabling, or even fatal treatment-related toxicities [92-94]. For example, when compared to younger cancer patients, older patients who undergo chemotherapy are more likely to suffer from grade 4 life-threatening toxicity, experience treatment disruptions (e.g., discontinuations due to toxicity), and die from complications related to treatment [95, 96]. Consequently, even low-grade chemotherapy toxicities (≤grade 2) are considered clinically significant in older adults and can be the motive for modifying or discontinuing chemotherapy [97].

Peripheral neuropathy is a common chemotherapy-related toxicity experienced by adult patients, regardless of their age. Neuropathy could damage one or more peripheral nerves [98]. CIPN is characterized by various sensory and motor symptoms, such as numbness, tingling, reduced sense of feeling in toes, pain, weakness, balance disturbances, and shortages in motor skills [99]. CIPN is one of the most disturbing side effects of chemotherapy for cancer patients [100]. Symptoms typically increase in severity during treatment and may partially reduce after its completion [101]. However, some patients experience chronic CIPN symptoms that continue even after treatment [102,103]. Symptoms might last for months following cancer treatment with unknown cessation [104].

Additionally, affected CIPN individuals frequently fall while walking, resulting in harm, hospitalization, or even death [105]. In the US, CIPN has impacted over 20 million individuals [106], with over 60% of cancer survivors reporting side effects from neuropathy [98, 104]. Patients with neuropathy have a 23-fold greater risk of falling [107].

Given the ever-increasing number of cancer patients and survivors, managing the side effects of cancer treatment is critical. Understanding how gait cycles and walking behaviors are affected for cancer patients suffering CIPN is essential for preventing falls and fall-related injuries [108]. Postural control systems (i.e., gait) are necessary for safe walking. Uterine cancer is likely to impact such systems, thus imposing an increased fall risk. Clinical studies comparing healthy controls and patients with diabetes suffering from neuropathy show that the latter have slower walking speeds, shorter steps, and more variable gaits [109,110]. Peripheral neuropathy in patients with Parkinson's disease causes individuals to walk with considerably shorter strides, more variable stride lengths, and slower walking speeds with increased fall risk [111].

In a typical gait, foot plantar pressure transfers from heel to toe in a spatiotemporal pattern with each step. When viewed across steps, some degree of intra-individual variability in pressure pattern is normal; however, nervous system pathology increases variability beyond an individual's pre-morbid range. The goal of this research was capturing the pattern of plantar pressure variability as it changes with the development of foot weakness resulting from neurotoxic chemotherapy treatment. This work reports plantar pressure variation measured at regular treatment visits compared to assumed baseline signals collected during the first visit. DMD-data driven modeling was used to capture characteristic features of plantar pressure variations between steps at three plantar regions for various walking trials. For gait assessment, patients repeated several 20-ft. walks at a self-selected, usual pace across a high-resolution Tekscan® Strideway™ sensor-impregnated walkway. Analyses and modeling aided in early identification

of CIPN toward optimizing chemo-dose titration and supportive care referrals. This information can improve quality of life for women during and after cancer treatment. This dissertation postulates that plantar pressure variation between steps (i.e., gait fluctuations) provides critical and required information for identifying CIPN and predicting fall risk. Persistent deviation from an individual's pre-chemotherapy, baseline variability could be used for clinical research and in treatment clinics to detect the onset of CIPN and high risk of fall.

4.2 Related Work

In published studies, walking behavior was characterized by various spatial and temporal parameters of gait, including stride length, step width, speed, and single- or double-support, as well as swing time, average, and peak pressure variation. Gait features characterization was performed using statistical analysis and data driven-based techniques.

4.2.1 Statistical Analysis-Based Techniques.

Researchers in [112] employed one-way ANOVA with Tukey's post-hoc statistical analysis to identify cancer survivors with and without neuropathy. Plantar pressure variability analysis included gait speed, average step length/width, and average step length/ width standard deviation (i.e., step length/width variability). Study participants included males and females at an average age of 55 years. Each individual completed two walking trials at their comfortable pace across a 6m Zeno™ pressure-sensitive walkway. Results indicated that cancer survivors with neuropathy had significantly less step length variability and more step width variability when compared with healthy controls. Researchers in [113] calculated repeatability and variability between various visits for plantar pressure measurements recorded for patients at various ages and of different gender. Data were acquired using a pressure mat system (Matscan, Tekscan Inc., Boston, MA, US). Average and peak pressure were analyzed in the forefoot (FF), midfoot (MF), and rearfoot (RF) regions. Plantar pressure variability was determined by

coefficient of variation (CV). The study concluded that although average pressure variability did not differ between age groups, peak pressure variability differed across foot regions and age groups.

Researchers in [114] proposed a method for identifying characteristic gait features using sensor-based gait analysis for patients with Huntington's disease (HD). Forty-three patients with HD and a cohort of age- (average 50 years old) and gender-matched healthy controls performed a standardized 4 × 10m overground gait test [80] on a 10m-long corridor at free walking speed. Gait parameters (e.g., stride length and gait velocity, as well as stride, stance, and swing time) were collected using sensor-based, wearable SHIMMER sensors (Shimmer Research Ltd., Dublin, Ireland). Other features were extracted using methods formulated in [115, 116]. Gait variability was evaluated by each parameter's CV. Results indicated that stride length and gait velocity were reduced by 15% and 19%, respectively, while stride time and stance time increased by 7% and 2%, respectively. CV coefficient increased by 17% for stride length and 41% for stride time. Researchers in [117] proposed a new foot-type classification method based on calculating bitmap index (BI) in static and dynamic conditions. Healthy volunteers were asked to perform footprint tests with full load, as well as plantar pressure distribution measures, using a Jasenco, JSP-C5 pressure plate.

A Pedar-X system (Novel Inc., Munich, Germany), in-shoe plantar pressure distribution measuring system was used for various research studies to measure pressure features within gait cycle. Researchers in [118] investigated the effect of previously diagnosed foot ulcers on plantar pressure variation during gait of patients with diabetic neuropathy. Plantar pressure variability was determined by CV. Neuropathic subjects presented higher variations than control subjects, mainly at the lateral forefoot, midfoot, and rearfoot. Another study [119] evaluated potential fatigue-related gait instability for the elderly to minimize injury due to fall risk. Peak pressure, contact time, and pressure-time integrals were measured for nine regions of the foot. Participants completed a 60-min. brisk walk on a

treadmill with median calculated for contact time, peak pressure, and pressure-time integrals in each plantar region, in addition to their asymmetry and variability. Results showed a significant increase in peak pressure and pressure-time integral at the medial and lateral arch regions, as well as central metatarsal regions. Plantar pressure variability at the medial arch was significantly increased, although asymmetry decreased. Contact time was significantly increased at all plantar regions. A similar work [120] calculated symmetry, variability, and laterality indices among 15 healthy volunteers and 14 patients suffering from diabetes and distal symmetrical polyneuropathy. Various gait features from force-time signals of gait cycle were extracted and analyzed. Results indicated that all indices were significantly greater in the diabetic cohort. Researchers in [121] analyzed variation in plantar pressure distribution due to foot deformation in diabetic patients. All participants completed walking trials at three different speeds (slow, normal, and fast walking) across a 4.5 m walkway, foot scanning system (3dMD LLC, Atlanta, GA, USA). Their plantar pressure distributions were also measured using a Pedar in-shoe system. Peak plantar pressure and pressure time integral variation in the toes, metatarsal heads, medial and lateral midfoot, and heel areas were statistically analyzed. Researchers in [122] developed a method for differentiating between stroke patients and healthy adults by analyzing changes in the center of pressure (COPx) in the medial-lateral axis. Participants were instructed to walk 5 m on flat ground at a comfortable pace while wearing insole pressure sensors, which measured ground reaction force (GRF). COPx data was then calculated and used to draw a polar gaitogram. The difference between the areas inside the two closed curves in the polar gaitogram, area ratio index (ARI), and slope of the tangential line common to the two closed curves were used as identification features. Researchers in [123] differentiated between Parkinson's disease (PD) patients' and healthy subjects' (HS) gait features using dynamic and kinematic analysis. Gait-related data were collected using an instrumented force-sensitive insole placed in subjects' shoes while they

walked at normal pace. Kinematic features showed statistically significant differences among the two groups for gait speed and time-up/go-test, as well as for selected indices (e.g., standard deviation and interquartile range of swing, stance, and double support time). Dynamic features did not show any statistically significant difference.

4.2.2 Data-driven Techniques.

Researchers in [124] proposed a potential solution for ML application to identify patients with diabetic neuropathy (DN) and diabetic foot ulceration (DFU). Eight conventional ML models were trained using features extracted from muscle electromyography (EMG) and ground reaction forces (GRF) data. The K-nearest neighbor (KNN) algorithm achieved the highest identification accuracy (98%). A developed convolutional neural network (CNN) was employed [125] for classifying non-diabetes mellitus (DM) and five DM severity grades from plantar thermal images. Model performance surpassed pre-trained neural networks, such as AlexNet and Cruz-Vega, with 98% classification accuracy and 0.96 F-score. Researchers [126] evaluated the fall risk of elderly individuals while walking by detecting foot weakness. Their method was based on extracting 44 multidimensional features related to the foot center of pressure (COP). Participants were allowed to walk a 20 m-long corridor at a normal pace while wearing an in-shoe plantar pressure sensing system. To classify subjects as high risk (HR) or low risk (LR), seven ML classifiers were utilized, including logistic regression, KNN, SVM, decision tree (DT), RF, gradient boosting decision tree (GBDT), and AdaBoost. [127] reearchers utilized CNN to identify subjects by capturing changes in individualss unique gait signatures. A plastic optical fiber (POF)-distributed, floor sensor system was used to capture spatiotemporal gait samples caused by varying ground reaction force (GRF) of a subject while walking. Researchers in [128] used a DMD-based method to analyze gait cycle of healthy control human gait with and without use of a cane by identifying dynamical

mapping between an upper limb and its contralateral lower limb. Dynamic variables for upper limb include the angular positions and velocities of the shoulder, elbow, wrist, and cane; lower limb variables include contralateral hip, knee, and ankle angles, which are measured with a motion-analysis, camera-system recording.

Researchers have reported significant changes in gait characteristic for CIPN patients walking on level ground at a self-selected speed. [112, 129] reported increased stride time. [129, 130] reported a significant decrease in gait speed among the patient group. An increased double support time was reported in [129, 131, 132]. Increased step width variability was reported in [129]. Similar changes were also noted among patients with diabetes and diabetic neuropathy [133, 134]. Peripheral neuropath associated with PD highly impacted walking balance and gait parameters [135].

4.2.3 Research Contribution Compared to Literature.

The aforementioned studies differ from the approach examined in this work in the following ways. To collect gait data, many researchers have utilized in-shoe pressure and insole sensors. However, the reliability of gait analysis results from most of these devices is low, because pressure sensors are usually only installed in the main parts of the insole, which limits their coverage. Consequently, the accuracy of the collected data is highly dependent on the location and installation of the sensors. Improper installation can lead to errors and noise in the data, which compromises the accuracy of the proposed scheme.

Most earlier studies utilized statistical approaches, measuring mean, median, standard deviation, symmetry/asymmetry index, and variability index or CV to model walking behavior. Employing statistical methods for gait analysis is less efficient, as the nature of the problem is complex and nonlinear. Furthermore, these methods are highly sensitive to noisy data that may lead to performance degradation. For example, earlier studies limited their performances to averaging

motion kinematics, reducing the scope of temporal analysis that a technique could achieve. Cited papers considered and processed pressure peaks (i.e., one or multiple points in a foot template [space]), while the approach reported in this work tracks pressure distribution across the foot, as well as temporal variability per pressure sensor. Furthermore, novel approaches may be effective in detecting changes in walking behavior at later stages of a disease. Notably, early detection of changes in walking behavior due to CIPN requires more advanced methods to better characterize gate cycle dynamics and identify any slight change in the dynamics due to neuropathy. Recognizing this paradigm, ML and DL techniques have recently been introduced. However, ML techniques require additional data preprocessing and expert knowledge to understand the data structure. DL techniques have high training costs, as such models require large training datasets to generate accurate results. [128] researchers employed DMD to analyze angular positions and velocities extracted from video recordings; however, these should initially be processed to generate said parameters. Video processing could possibly include uncertainties due to many factors that could affect recording or processing quality. [128] processed a significantly reduced spatial domain of only 12 parameters to describe a gait cycle. The spatial resolution of the investigation reported herein was significantly higher.

The system used for data collection in the analysis performed for this dissertation employs a pressure mat for data collection, which (when calibrated) provides stable and repeatable measurements with less variability. This approach tracks pressure distribution across the foot, as well as temporal variability per pressure sensor. Pressure levels were measured directly from the interaction of a foot with a mat. Given CIPN occurs, its effect was expected to directly influence the amount of pressure exerted on the mat. A DMD approach has several advantages. First, it has high accuracy for complex non-linear systems, which makes it a suitable method for gait analysis and CIPN identification. Additionally, it can extract and analyze spatiotemporal patterns from high-dimensional data. DMD

can also identify dominant modes of motion in a system and separate them from noise and other irrelevant data. Finally, DMD can be used for real-time gait analysis, as it requires minimal data preprocessing and no model training. These features save time and resources.

4.3 Methodology

4.3.1 Subjects and Data Collection

Data collection was performed at the University of Oklahoma Health Sciences Center's Stephenson Cancer Center (SCC) Rehab Research Laboratory (OUHSC IRB #11473). Thirty-two women aged 40 to 85 scheduled to begin neurotoxic chemotherapy enrolled in a CIPN observational study and were measured before their first infusion. Patients wearing standard slipper-socks were instructed to perform repeated walks at a self-selected, usual pace across a 20-ft, high-resolution (3.88 sensels/cm^2) Tekscan® Strideway™ (Tekscan, Inc; Boston, MA) [136]. Collected data represented a spatial-temporal plantar pressure map, as indicated in Figure 4.1. Because diabetic neuropathy places women at risk for chemo neuropathy, the current longitudinal study included more than 50% of the women who were diagnosed with diabetes for baseline measurements. Table 4.1 shows demographic and clinical characteristics of patients participating in the study's data collection.

The Tekscan™ Strideway device is a modular human gait analysis system widely used by many health organizations for physiotherapy and rehabilitation applications [137, 138, 139]. The device consists of hundreds of embedded force sensors that collect detailed spatiotemporal parameters of a gait cycle. The assembled system covers an area of approximately 4 m^2 and is wired through a USB cable to a nearby computer equipped with Strideway software. The program automatically reads data collected from the physical sensors in the mat, and then performs calculations to derive various gait parameters (e.g., step/gait time, cadence, velocity, and walked distance). The system provides reliable measures

for human gait plantar pressure. During the tests, the software stores and visualizes performed steps a heat-map, which shows locations of the performed steps on the mat, as well as each step's pressure intensity.

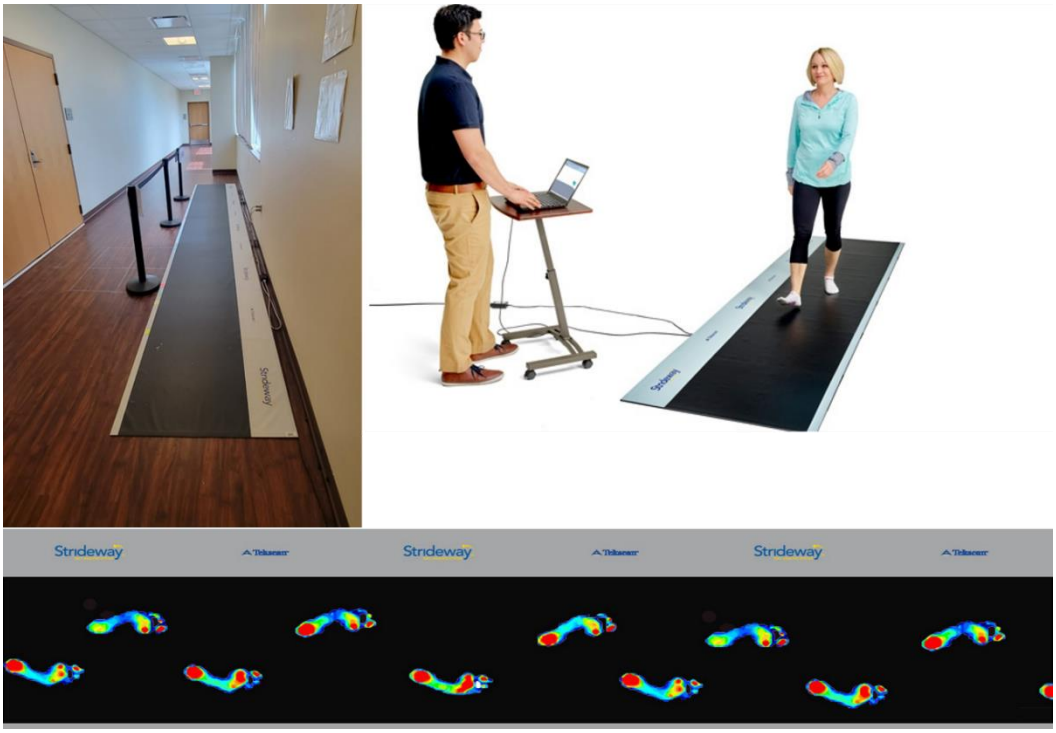

Figure 4.1. Tekscan™ Strideway® [136] at the OUHSC SCC Rehab Research Laboratory.

Table 4.1
Demographic Characteristics of Patients Participating in the Study's Data Collection

	Sensory & Motor with Numbness	Sensory & Motor without Numbness&	Motor Only	No Symptoms
Age (years) Mean ± SD	63.09 ± 10.07	55.5 ± 4.94	46.5 ± 16.26	60
White/Not Hispanic or Latino	11 (91.667)	2 (100.0)	0 (0)	1 (100)
White/Hispanic or Latino	0 (0.0)	0 (0.0)	2 (100)	0 (0)
Black/African American/Not Hispanic or Latino	1 (8.33)	0 (0.0)	0 (0)	0 (0)

Weight	176.26 ± 53.56	158.12 ± 3.99	212.46 ± 36.55	164.35 ± 1.68
Height	65.42 ± 2.35	63.5 ± 0.71	66.5 ± 2.12	65
BMI	29.05 ± 9.03	27.66 ± 0.62	32.97 ± 4.54	27.35 ± 0.31
Skeletal Muscle Mass	56.95 ± 9.29	52.41 ± 4.73	68.19 ± 10.86	50.38 ± 0.98
Cancer Type number (%)				
Breast	2 (16.67)	0 (0.)	1 (50)	0 (0)
Uterine	6 (50)	0 (0)	0 (0)	1 (100)
Ovarian	4 (33.33)	1 (50)	1 (50)	0 (0)
Peritoneal	0 (0)	1 (50)	0 (0)	0 (0)
Not Diabetic	4 (33.33)	2 (100)	2 (100)	0 (0)
Pre-Diabetic	3 (25)	0 (0)	0 (0)	0 (0)
Diabetic	5 (41.66)	0 (0)	0 (0)	1 (100)
Onset of NTX number (%)				
After 1 Cycle of Chemo	8 (66.67%)	2 (100%)	2 (100%)	
After 2 Cycles of Chemo	3 (25%)	0 (0%)	0 (0%)	
After 1 or 2 Cycles of Chemo	1 (8.33%)	0 (0%)	0 (0%)	

4.3.2 Plantar Pressure Variation Analysis and Modeling

Figure 4.2 illustrates the modeling and methodology developed for analyzing step-to-step plantar pressure variation, which involves examining the intra-step plantar pressure variability within the heel, metatarsal, and big toe foot segments. The methodology can be described in the following steps.

1. First, patients' walking-phase plantar pressure spatial-temporal raw data is read as an input, which represents a heat map for plantar pressure intensity measured by Tekscan sensors.
2. Next, the data is converted into a 2D image consisting of pixels (2D matrix), wherein each pixel represents a pressure value measured by a sensor (see Figure 4.3).
3. Each footstep is then extracted from the image and segmented into various regions using a novel image processing-based technique developed for this work (see Figure 4.6).
4. Subsequently, temporal signals are formed by horizontally concatenating timeseries pressure signals for multiple individual sequential footsteps, as described in Figures 4.4 and 4.5. Individual timeseries signals for a foot segment were constructed from the spatial-temporal raw data output of the Tekscan device. Raw data are in the form of a spatial-temporal tensor (3D-matrix) with two dimensions for spatial location (X, Y-axes) and a third dimension (Z-axis) consisting of multiple frames (each 0.02 sec) for temporal dimension. Required temporal signals are constructed by summing the values of activated pixel pressure values per frame.
5. Finally, a standard DMD algorithm (see Algorithm 3.1) is applied to the formed temporal signals to extract DMD eigenvalues and DMD modes, and then model/analyze plantar pressure variation for CIPN identification.

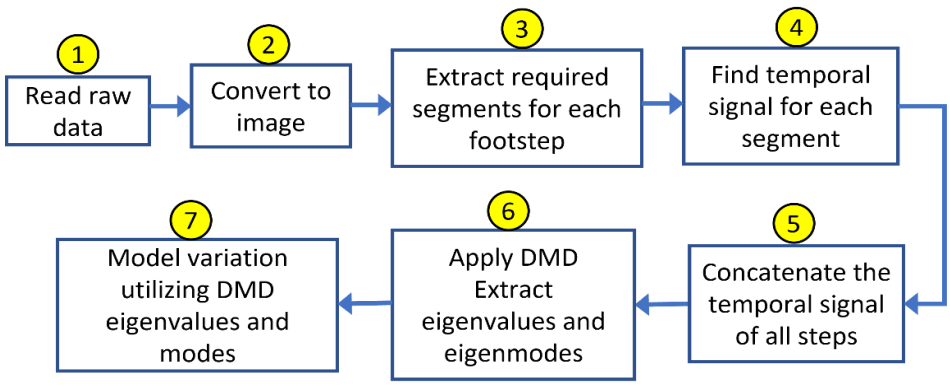

Figure 4.2. Developed methodology of plantar pressure variability analysis and modeling.

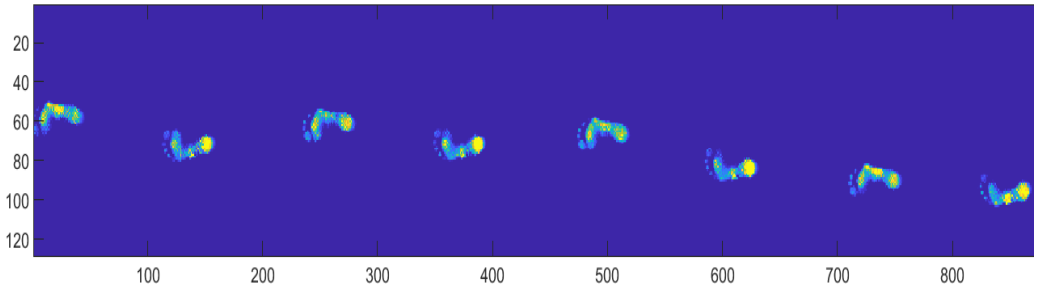

Figure 4.3. Raw plantar pressure map measured by Tekscan strideway.

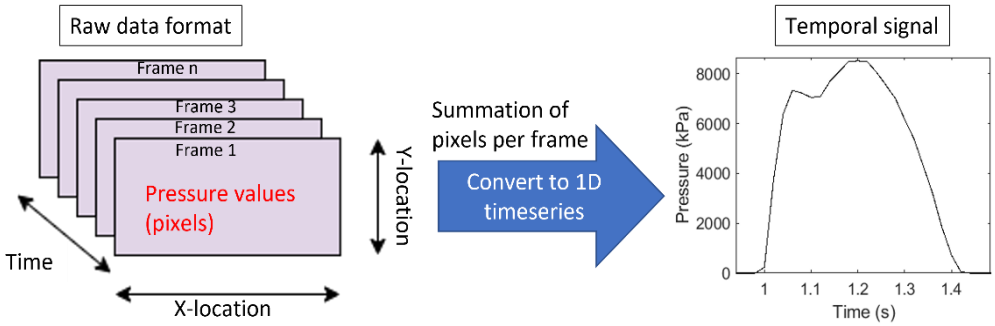

Figure 4.4. Constructing temporal signals from raw data tensor for a foot segment.

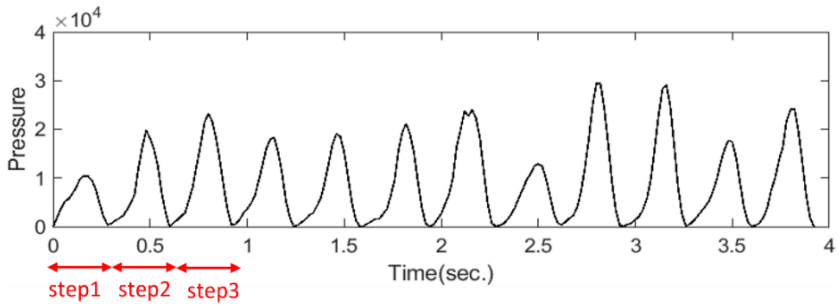

Figure 4.5. Concatenated temporal signals of left foot heel sequential steps.

4.3.2.1 Footstep Plantar Pressure Segmentation

The analysis performed for this dissertation focused on variation in plantar pressure for three plantar regions: heel, metatarsal, and big toe. The midfoot segment was excluded from analysis, as it was reported to have high variation at usual walking conditions [113] and may not provide a clear indication of characteristic feature changes in pressure variations across steps and among visits.

An innovative footstep segmentation software (MATLAB-based) was developed to generate accurate foot segments. Figure 4.6 shows an example of a

footstep segmented with the newly developed algorithm. Using a set of geometrical operations to process an extracted image for a phase trial pressure map afforded the opportunity to extract every footstep, and then segment it into anatomically relevant regions/segments. Figure 4.6 highlights the multi-phase segmentation process.

The developed segmentation method has the following advantages.

1. The generated template is adaptive, adjusting dimensions to fit each footstep.
2. The algorithm is fully automated and does not require user interaction.
3. The algorithm extracts required segments with high accuracy in a short processing time (i.e., approximately 1 second per step).

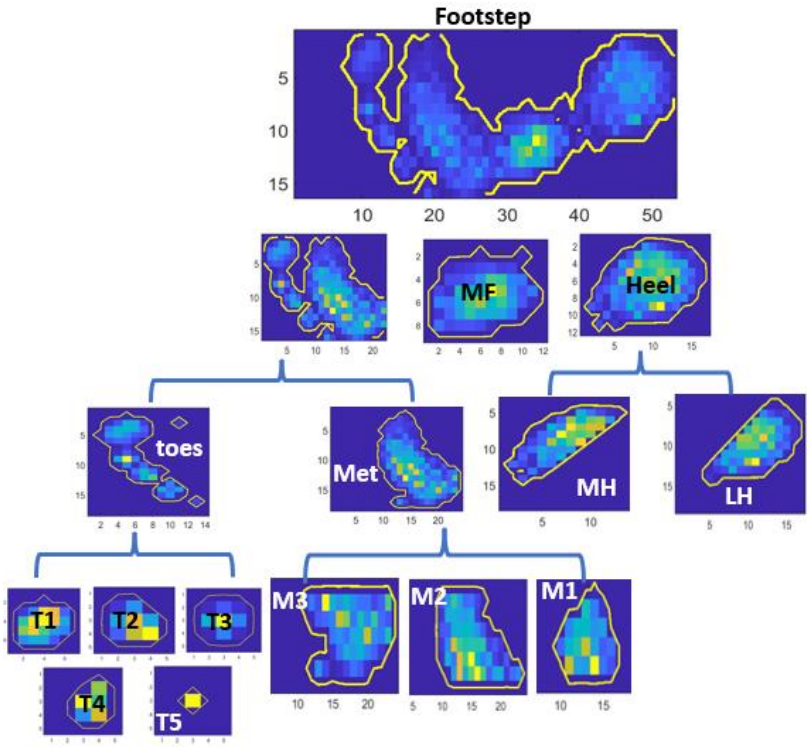

Figure 4.6. Footstep segmentation using the developed scheme.

4.3.2.1.1 Extracting and Identifying Single Footstep (Right or Left Foot)

The first step in the segmentation process is extracting each footstep and identifying it as left foot (LF) or right foot (RF). To extract a single footstep, a zero-

value isolation between pixels was used, as illustrated in Figure 4.7. The processed image appears as a matrix with pixel values along each column summed into a one row vector. Scanning the resulted vector along the x-axis from right to left shows the beginning pixel location of a footstep (i.e., the first pixel with a value greater than zero) and the ending pixel of a footstep (i.e., the last pixel location with value greater than zero). By capturing the locations of the start and end pixels of a footstep, the data of a footstep can be easily cropped/extracted.

In addition, the sign of angle θ between the horizontal axis and the line joining between a footstep start point and mid-point were utilized to identify a foot (i.e., RF or LF), which is detailed in Figure 4.8. The LF is characterized by a negative angle, and the RF is characterized by a positive angel. Algorithm 4.1 in the appendix provides a comprehensive set of coding instructions for stage1 of the segmentation code.

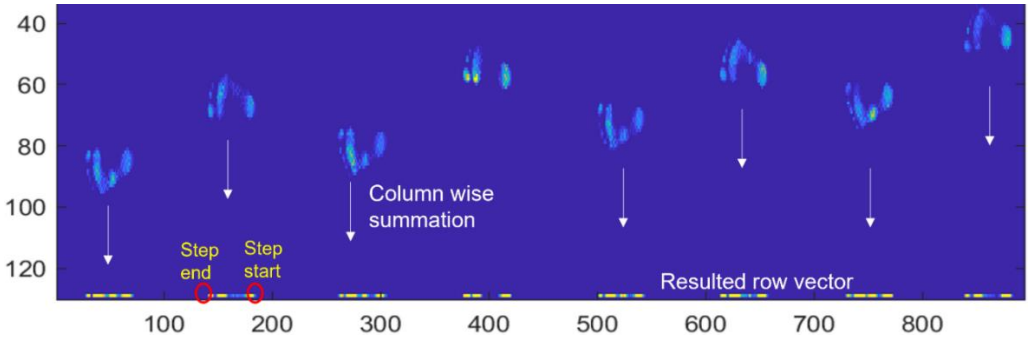

Figure 4.7. Individual step cropping procedure.

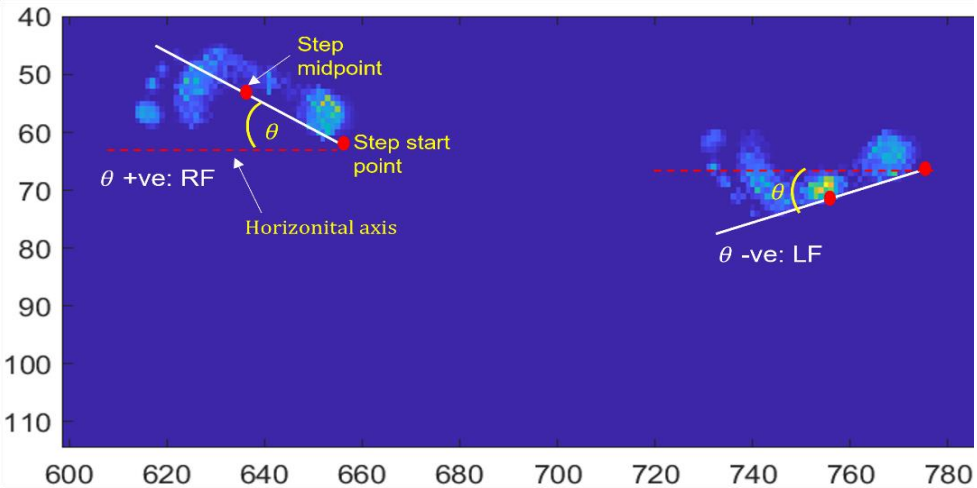

Figure 4.8. LF/RF identification procedure.

4.3.2.1.2 Extracting Footstep Main Three Segments

After extracting a footstep, it is segmented into three main parts. Based on [140, 141], the heel segment represents the first 30% of the footstep; the MF segment represents the next 21%; and, finally, the forefoot (metatarsal-toe) segment is the remaining 48%.

The segmentation algorithm is illustrated in Figure 4.9, as well as algorithm 4.2 in the appendix. A footstep is divided along the tangent line (baseline) of the lateral foot using the mentioned percentages. The tangent line is plotted such that its start and end match the footstep start and end points (pixels), which were determined in the previous stage. The segmentation process was performed according to the following steps.

1. Plot tangent line (baseline) to the footstep between the start and end point of the foot.
2. Plot two perpendicular lines to the baseline at the start and end points of the footstep.
3. Plot another two lines parallel to the perpendicular lines at distances d1 (heel line) and d2 (MF line), respectively, from the footstep start point, such that,

$$d_1 = (30/100)L \tag{4.1}$$

$$\text{and } d_2 = (52/100)L \ , \tag{4.2}$$

where L is the length of the baseline.

4. Plot a horizontal line from the center of the first pixel of each row.
5. Find the intersection points between the horizontal lines and two perpendicular lines (MF line and heel line). The intersection points indicate the exact location of the three main segments.

6. Crop the heel, MF, and forefoot segments from the intersection points located on the parallel lines.

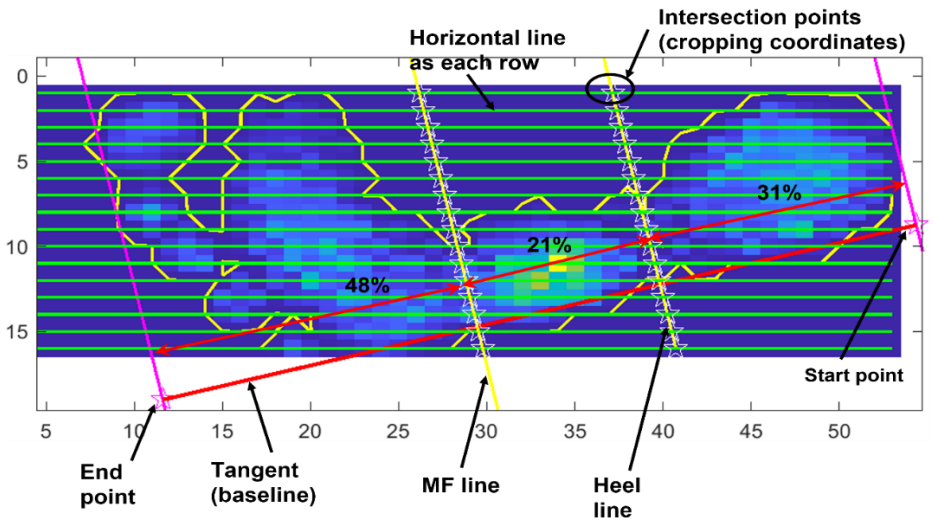

Figure 4.9. Geometric interpretation for cropping three main segments.

4.3.2.1.3 Splitting the Heel

Figure 4.10 highlights that the heel segment is bisected into two equal regions, namely medial heel (HM) and lateral heel (HL). Bisection is performed along the centerline of the heel segment, drawn from the center point and parallel to the baseline. Detailed coding of the process is shown in algorithm 4.3 in the appendix.

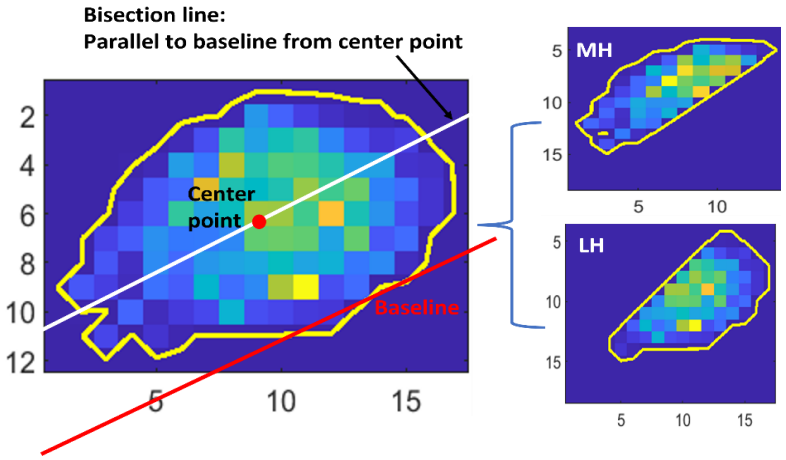

Figure 4.10. Heel segmentation into MH and LH.

4.3.2.1.4 Toes-Metatarsal Isolation.

The proposed method for isolating the toes-metatarsal segments involves identifying the group of low-pressure pixels (i.e., valley) located between the toes and metatarsal. This group of pixels is detected using a threshold value, as illustrated in Figure 4.11, as well as algorithm 4.4 in the appendix. The pixels are then replaced by zeros. Cropping coordinates for segment extraction are determined by the location of these zeros. Cropping is performed on the original image before thresholding.

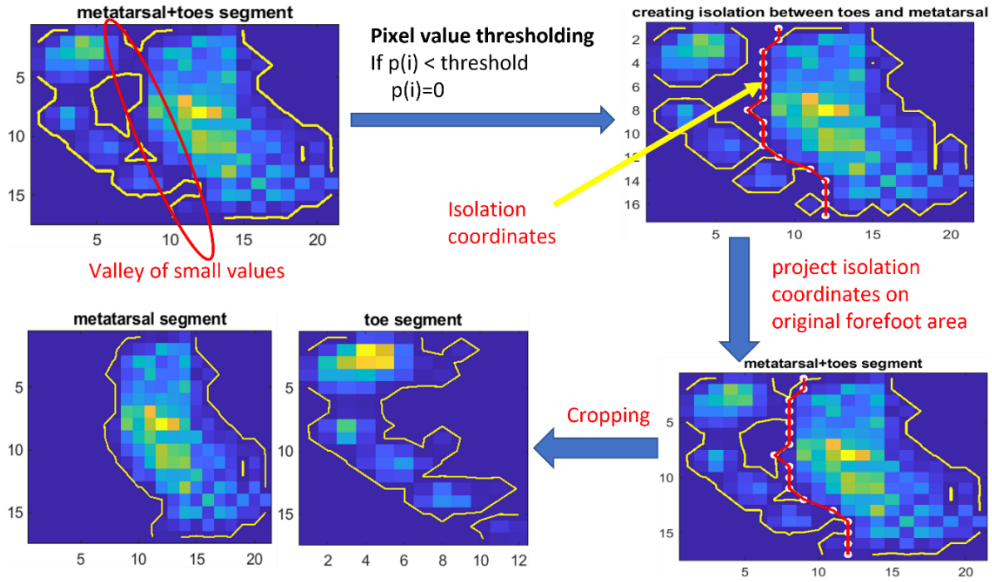

Figure 4.11. Proposed toes-metatarsal isolation method.

4.3.2.1.5 Toes and Metatarsal Segmentation.

Figure 4.12 shows that the extracted metatarsal segment is divided into three equal parts (M1, M2, and M3) through vertical trisection. The toe segment consists of five toes (T1, T2, T3, T4, and T5), each extracted and cropped using the algorithm detailed in Figure 4.13 and algorithm 4.5 in the appendix. The algorithm involves capturing the coordinates of the pixel indicating the peak pressure within each toe, and then cropping this pixel and its neighboring pixels to extract a toe.

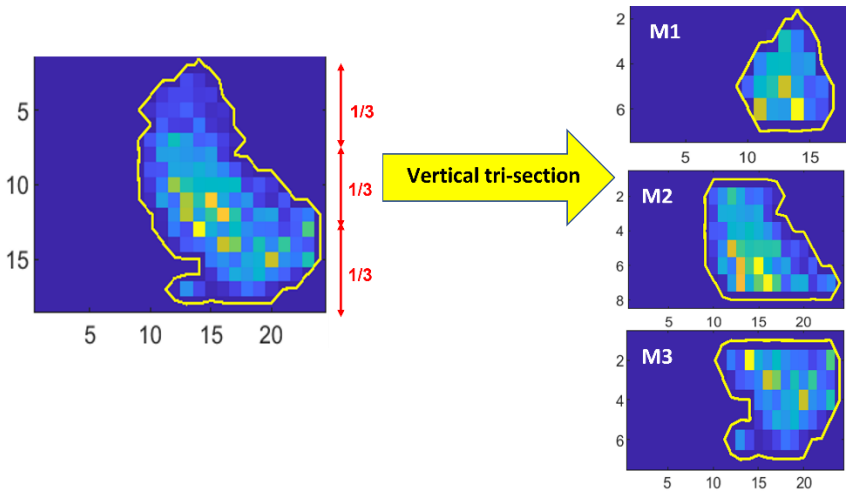

Figure 4.12. Metatarsal segmentation.

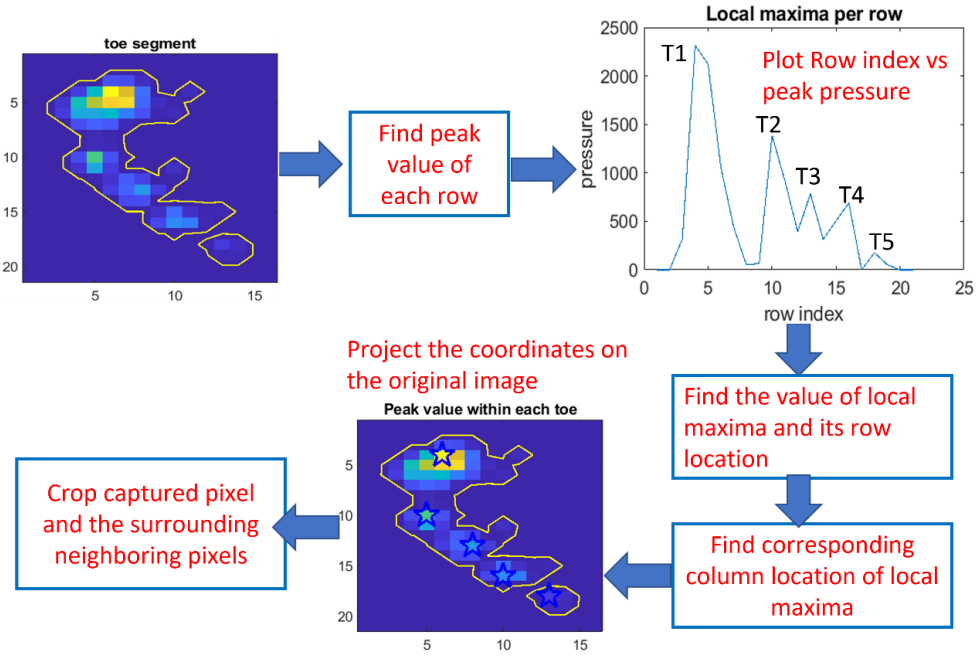

Figure 4.13. Toes segmentation.

4.3.2.1.6 Temporal Signals Generation

The developed algorithm extracts and stores the temporal signals for four footstep segments (i.e., heel, midfoot, metatarsal, and toes), in addition to the temporal signal for the entire footstep. This task is accomplished by applying the temporal extraction method discussed earlier in Figure 4.4 after extracting each segment. Figure 4.14 illustrates a sample of a generated temporal signals for one footstep, indicating the contribution of each segment to the overall footstep signal.

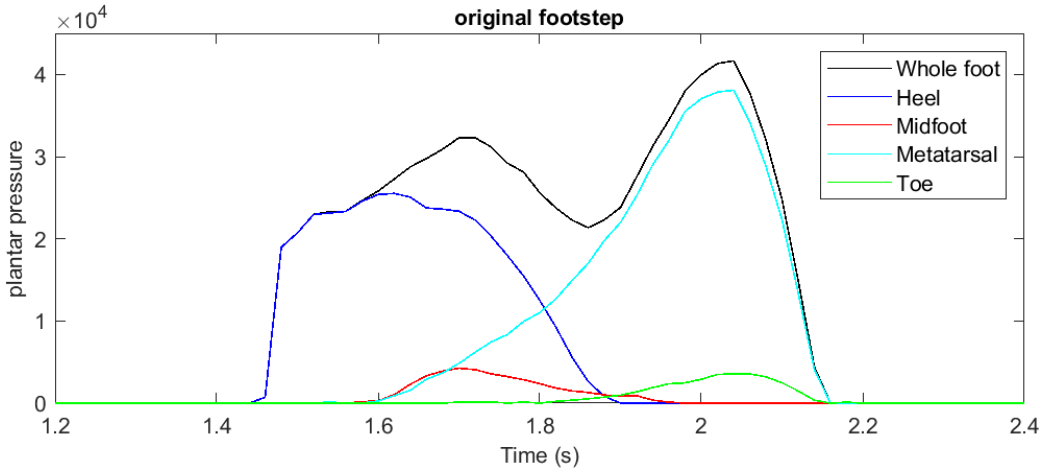

Figure 4.14. Temporal signals for main foot segments generated by the developed algorithm.

4.3.2.2 DMD Modes Φ Interpretation for Plantar Pressure Variation Analysis

DMD dynamic modes are characteristic eigenvectors whose direction does not change following transformation. These modes describe how each element of the timeseries measurement vector y_k are dynamically related. The magnitude of a DMD mode (i.e., absolute value) provides a measure of mode participation/influence in the system dynamics. DMDmode magnitude provides a quantitative measure for determining dominant modes (i.e., more represented in the decomposition).

The proposed algorithm utilizes DMD modes magnitude to model change in plantar pressure variation when comparing a specific patient's baseline visit (visit 1 or V1) with their successive visits. When applying algorithm 3.1 on a timeseries signal for a specific foot segment, the 30 highest magnitude DMD modes were selected and evaluated for importance. Figure 4.15 details an overview of the developed method. Dominant DMD modes represent components (i.e., vectors) with greatest influence on step-to-step plantar pressure variation. In other words, a change in DMD mode characteristics indicates a change in walking behavior.

4.3.2.3 DMD Eigenvalues λ_i Interpretation for Plantar Pressure Variation Analysis

DMD discrete eigenvalues describe the growth/decay and oscillatory characteristics of the corresponding DMD dynamic mode. DMD eigenvalues can be realized by the complex-cartesian coordinate plane, as indicated in Figures 3.23, 3.24, and 3.25. DMD eigenvalues are in the vicinity of the unitary circle. DMD modes corresponding to eigenvalues inside the unit circle are decaying modes; modes corresponding to eigenvalues outside the unit circle are flourishing modes; and those corresponding to eigenvalues on the circle are stable, oscillatory modes.

In addition to modeling plantar pressure variability using DMD modes, DMD eigenvalues were utilized to characterize plantar pressure variations during successive patient visits. This method was based on extracting and comparing the 30 dominant DMD eigenvalues, and then plotting them and their centroid (i.e., average) on the complex plane. Dominant eigenvalues were defined as DMD eigenvalues corresponding to the 30 DMD modes of highest amplitude. Figure 4.16 provides an overview of the developed, DMD eigenvalues-based method.

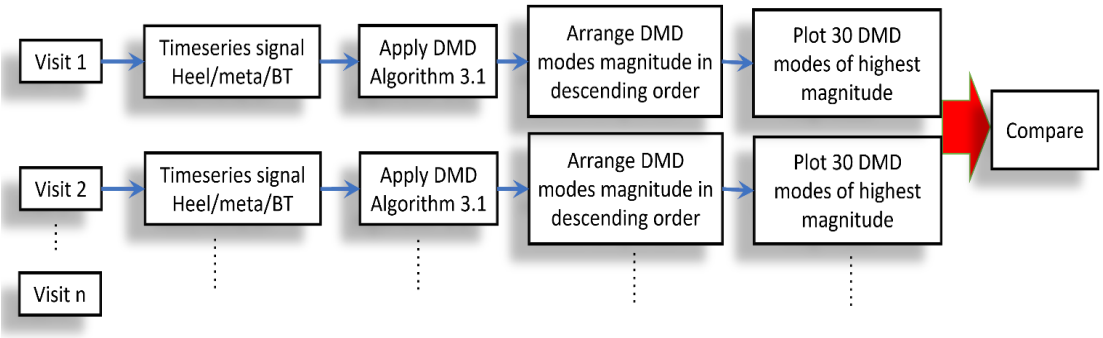

Figure 4.15. Plantar pressure variation characterization employing DMD modes magnitude.

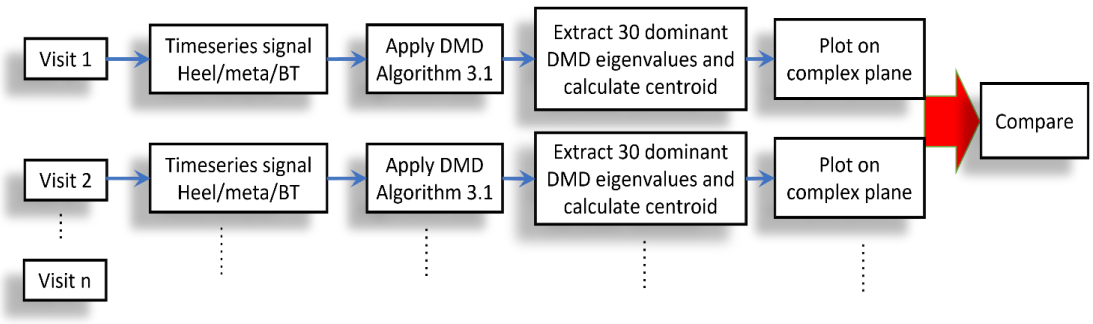

Figure 4.16. Plantar pressure variation characterization employing DMD eigenvalues.

4.4 Results and Discussion

This section presents the outcomes of employing the developed DMD-based approaches that were discussed as part of the methodology (see Section 4.3). The dataset comprises footstep plantar pressure measurements from 17 patients, each of whom were evaluated at several visits. The objective was to utilize DMD to characterize variations in plantar pressure among consecutive visits, and then compare them with the partient's baseline visit (i.e., first visit).

4.4.1 Applying DMD Modes Magnitude-Based Technique

For study participants, first technique was applied to capture changes in plantar pressure variation in the heel, metatarsal, and big toe segments (see Section 4.3.2.2). Dominant DMD modes' magnitude deviation from the baseline signal obtained during a patient's initial visit (V1) served as a defining characteristic of the severity of change in walking behavior. Descriptive results are listed in Table 4.2.

4.4.1.1 Heel Signals Analysis

Figure 4.17 provides a sample of constructed temporal heel signals for one participant. Figure 4.18 lists resulting DMD modes magnitude comparison for all available visits for two randomly selected participants. The magnitude of the most dominant DMD modes (i.e, first 15 modes) for LF greatly decreased as visits progressed. When compared with LF, the magnitude of DMD modes RF signals had a lower reduction as visits progressed. The second patient (Patient 2) had a very slight change in RF DMD modes magnitude between visits.

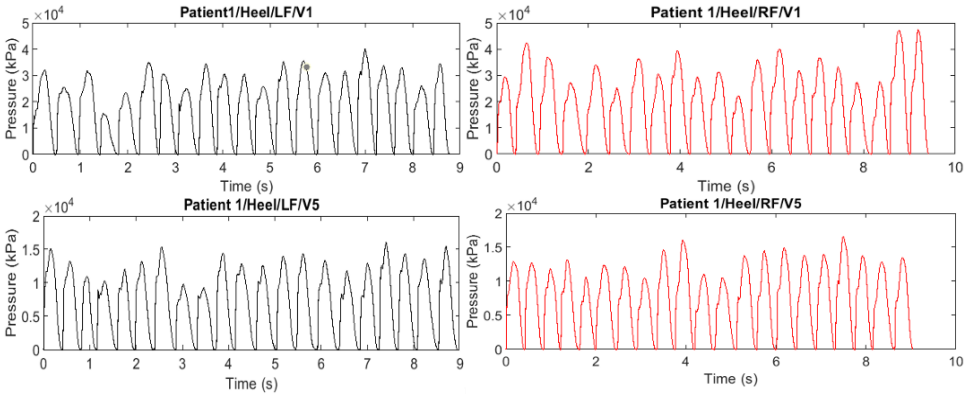

Figure 4.17. Samples of heel timeseries signals.

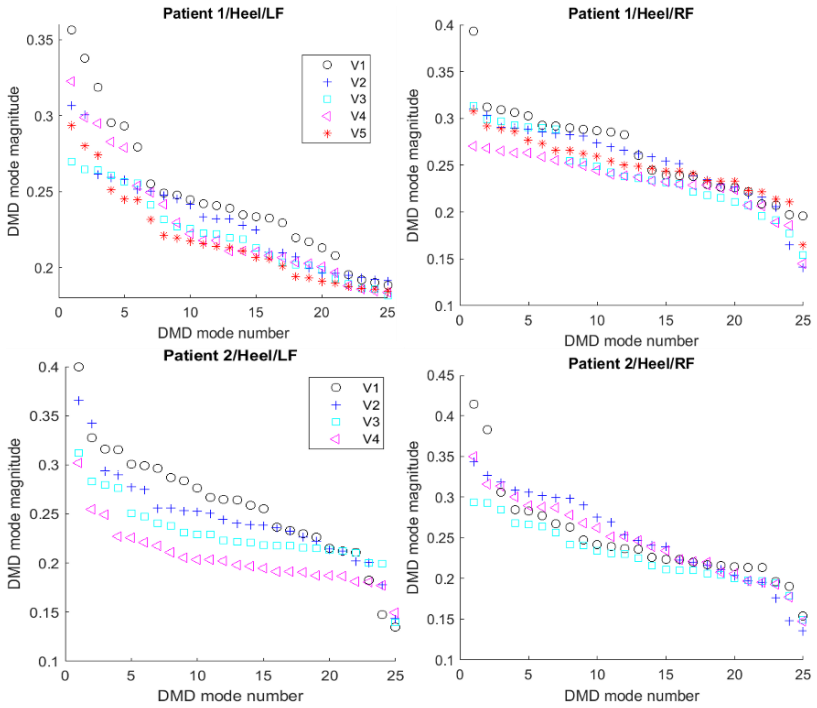

Figure 4.18. Samples of heel DMD modes magnitude comparison for various visits.

4.4.1.2 Metatarsal Signals Analysis

Figures 4.19 and 4.20 visualized metatarsal temporal signals and resulted DMD modes from available visits for the same group of participants selected for heel analysis. Figure 13 indicates that LF modes magnitude had a similar trend for heel segment, while the RF modes had less variation between visits.

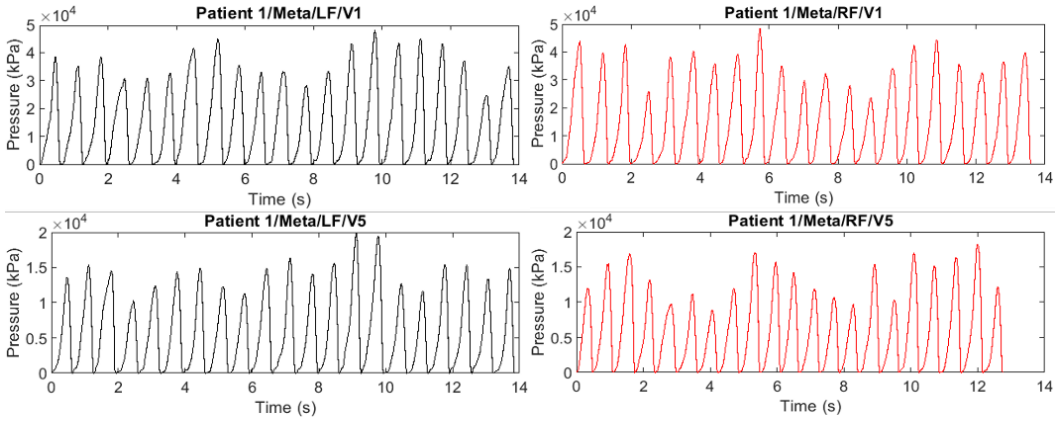

Figure 4.19. Samples of metatarsal timeseries signals.

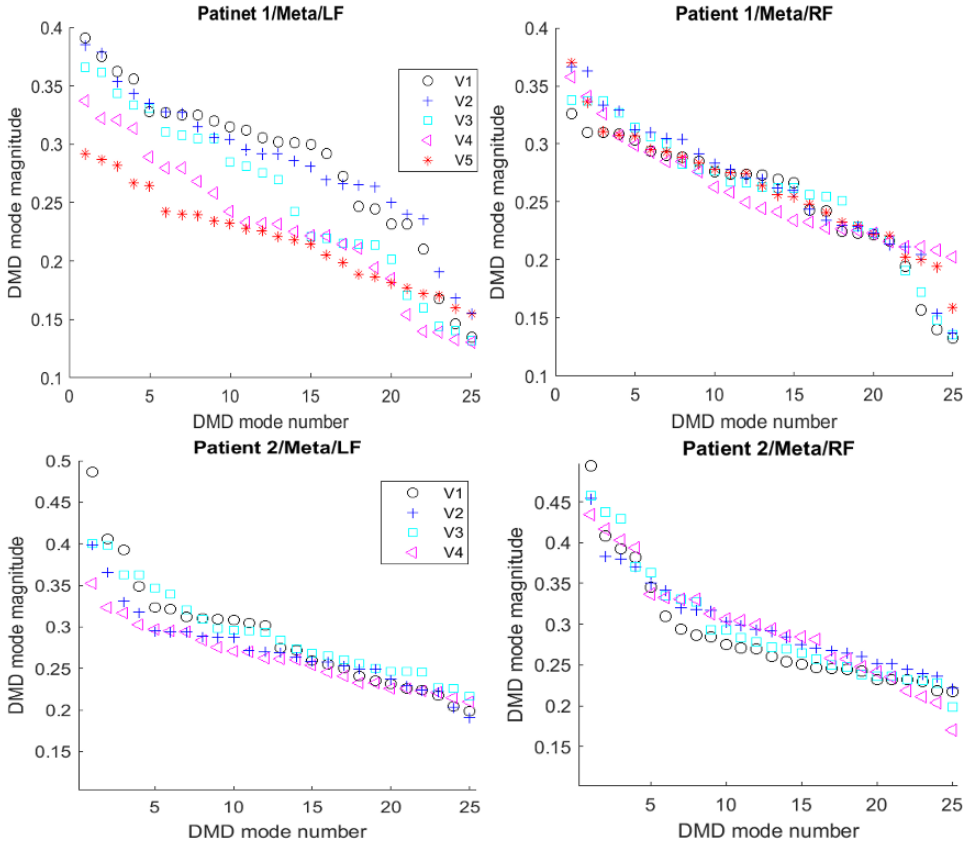

Figure 4.20. Metatarsal DMD modes magnitude comparison for various visits.

4.4.1.3 Big toe (BT) Signals Analysis

Figures 4.21 and 4.22 visualize BT temporal signals and resulted DMD modes from available visits for participants selected for heel and metatarsal analysis. Patient 1 RF had a greater reduction in DMD modes magnitude among visit progression when compared with LF DMD modes magnitude. Conversely, patient 2 RF had a slightly higher DMD modes magnitude.

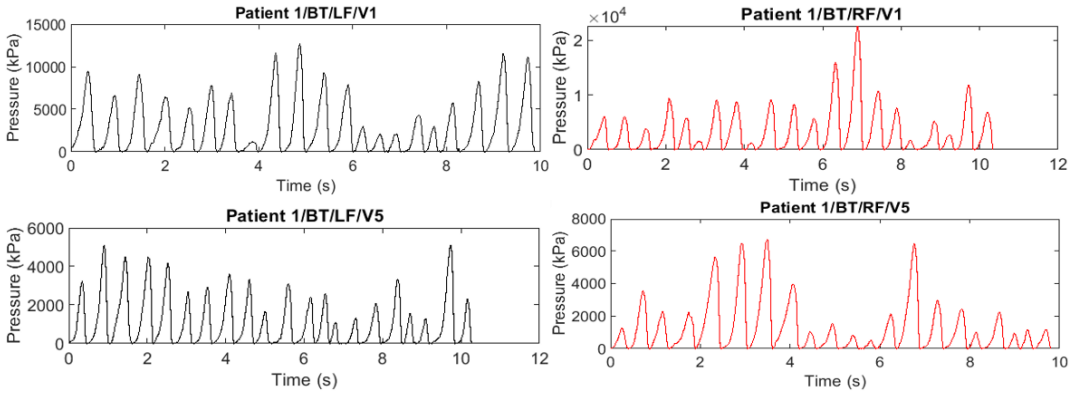

Figure 4.21. Samples of BT timeseries signals.

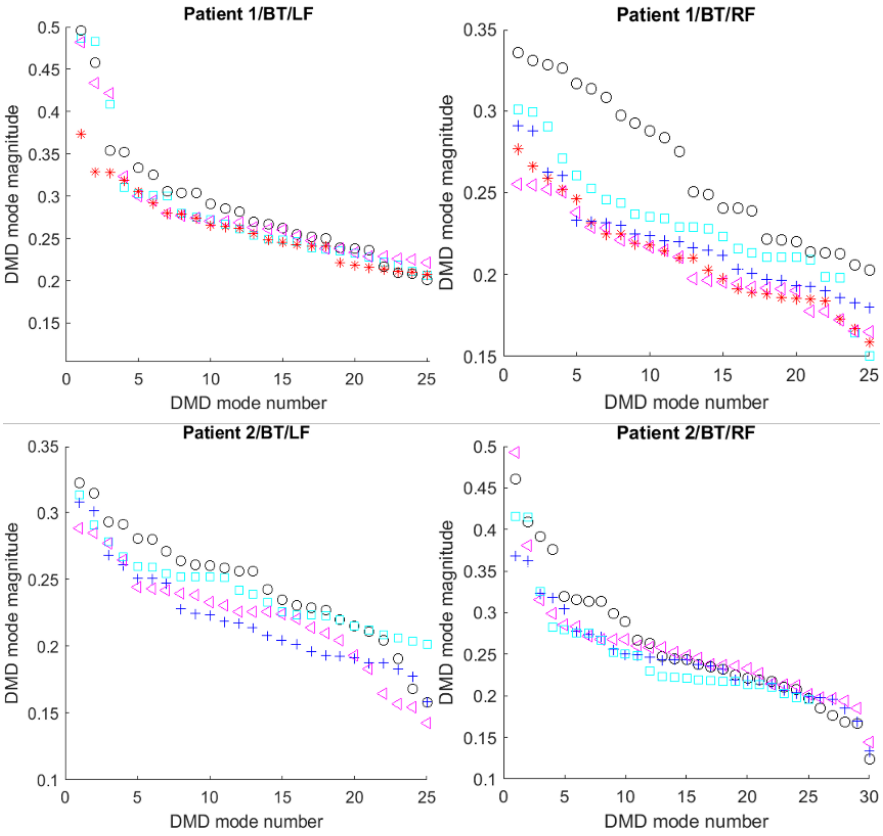

Figure 4.22. Samples of heel DMD modes magnitude comparison for various visits.

4.4.2 Applying DMD Eigenvalues-Based Technique

As previously discussed in the methodology section (see Section 4.3.2.3), this method is based on evaluating the centroid of 30 DMD eigenvalues corresponding to the most dominant DMD modes. The method was applied on timeseries signals of the extracted segments for available patients in the dataset. Figures 4.23, 4.24, and 4.25 demonstrate DMD eigenvalue results for two randomly selected patients.

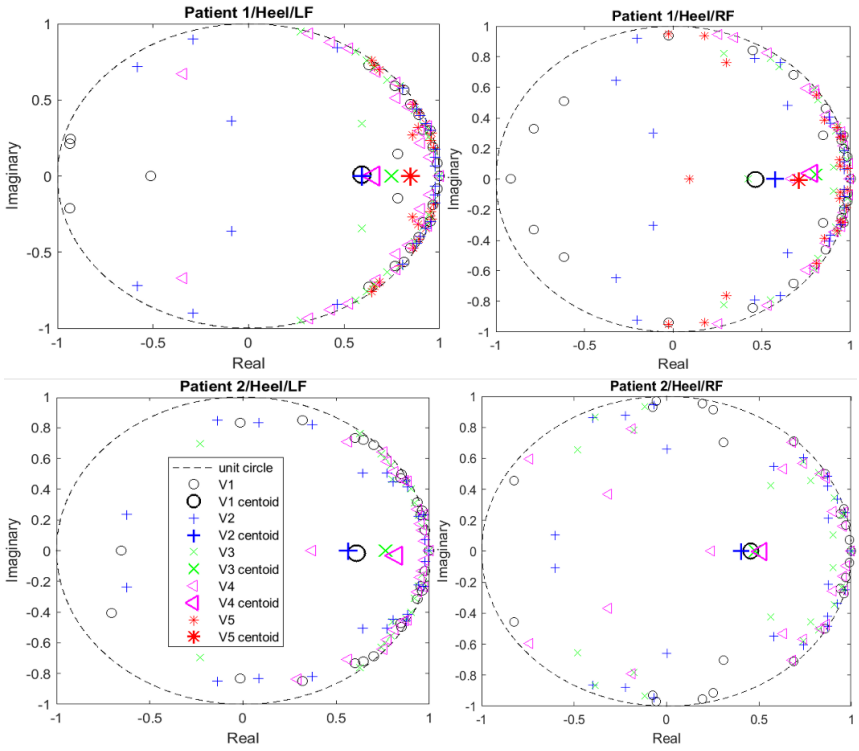

Figure 4.23. Heel DMD eigenvalue comparison for various visits.

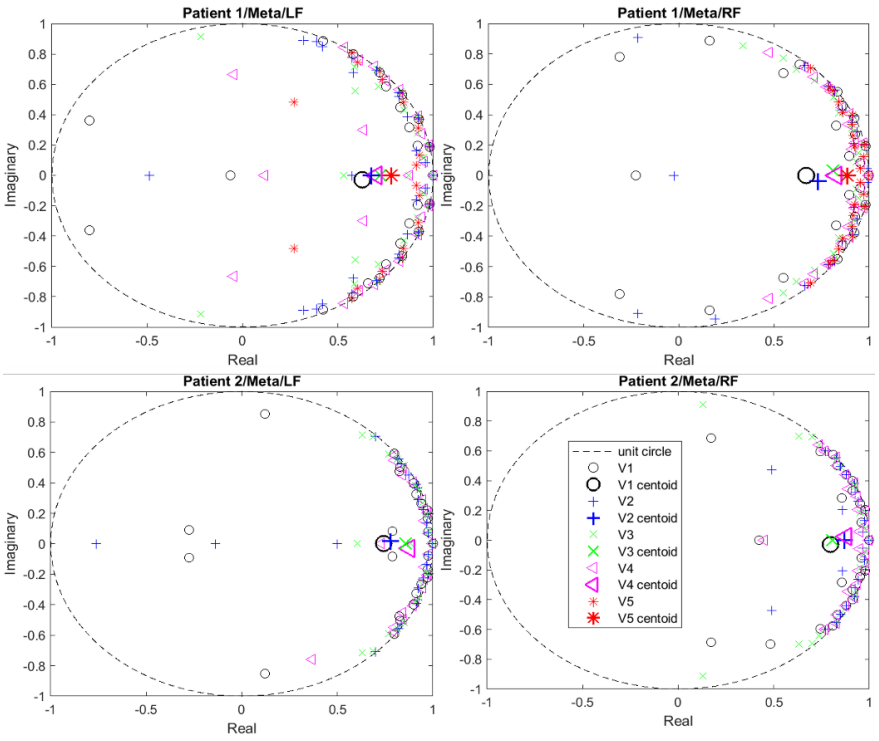

Figure 4.24. Metatarsal DMD eigenvalue comparison for various visits.

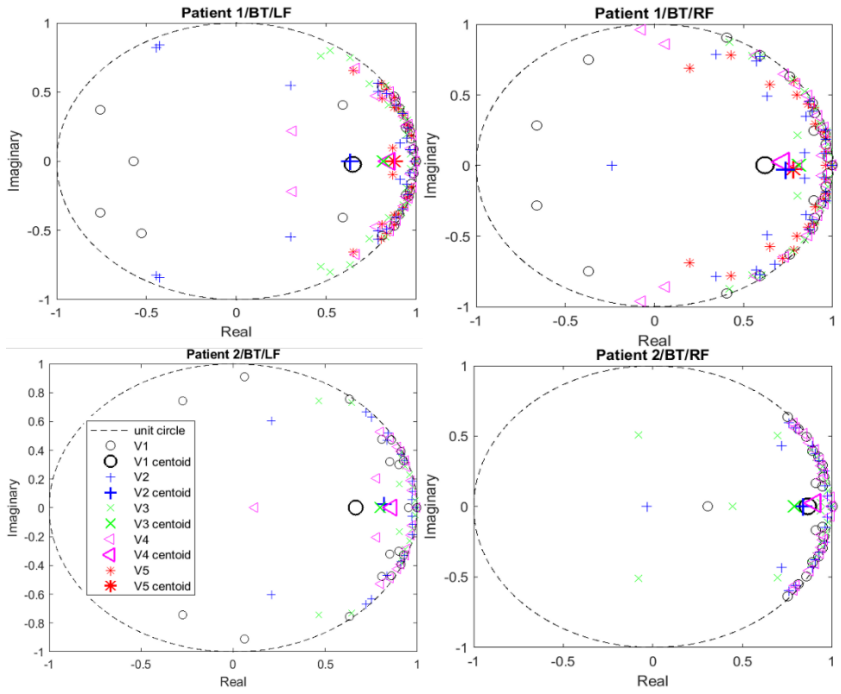

Figure 4.25. Big toe DMD eigenvalue comparison for various available visits.

4.4.3 Detailed Results and Discussion

Table 4.2 provides detailed results for DMD modes amplitude and eigenvalue variation per second and last visits for 17 patients. Percent change was calculated

using V1 data as the baseline. Plantar pressure variation change per visit was calculated using the following formula:

$$\%Change = \frac{\sum_{V_k} X_i - \sum_{V_1} X_i}{\sum_{V_1} X_i} * 100 \ , \quad (4.3)$$

where X_i is the DMD modes magnitude/eigenvalue for a specific visit V. K is the visit number, such that k > 1, and V_1 indicates the first visit (i.e., baseline).

Results presented in Table 4.2 and Table 4.3 show that as chemotherapy treatment progressed, the strength of dominant DMD modes for both LF and RF reduced. In other words, the effect of the most dominant DMD modes on foot dynamics weakened in comparison to the less dominant modes, as indicated by the reduction in their magnitude values. When compared to baseline modes obtained from V1, V2 reduction ranged between approximately 1% and 16% for both LF and RF; V2 demonstrated the least drop. The majority of participants' subsequent visits had a larger inclination in DMD modes' amplitude, attaining least strength on the most recent visit. Overall reductions varied between 1% and 22% for RF and between 12% and 36% for LF. For the examined foot segments, most patients demonstrated greater percentage decrease in LF than in RF. The average and standard deviation of the change in DMD modes magnitude from V2 to the most recent visit is shown in Table 4.4.

Results presented in Table 4.2 confirmed that the dominant DMD-eigenvalues shifted toward the unit circle, resulting in an increase in oscillation period and a decrease in decay over the course of chemotherapy treatment. The attested lower decay rate and longer oscillation periods indicates increased mode dynamics with less amplitude. This change in the DMD modes characteristics is due to increased walking instability as a result of chemotherapy treatment. A change in eigenvalues (e.g., between 2% and 34.8% for the LF and between 5% and 21% for the RF) was found during V2. The most significant changes were associated with the last visit. Eigenvalues varied between 10% and 61% for RF and between 20% and 169% for

LF. The LF demonstrated higher change in eigenvalues than that of RF for most participants. The average and standard deviation of the change in dominant DMD eigenvalues are shown in Table 4.5.

Table 4.2
Percentage Change in Plantar Pressure Variability
Captured by Employed DMD-based Schemes

		Heel				Metatarsal				BT			
		Mode Mag.		DMD eig.		Mode Mag.		DMD eig.		Mode Mag.		DMD eig.	
		LF	RF	LF	RF	LF	RF	LF	RF	LF	RF	LF	RF
CIP 05	V2	-13	-5.2	9.2	21.1	-4.5	0.2	3.6	10.2	-2	-13	1.7	12
	V5	-25	-18.6	16.6	41.8	-20.5	-8.5	35.8	9	-18	-25	30	39
CIP 06	V2	-9	0.6	10.5	14	-0.4	-4	13.5	1	-12.3	-4	2	4.5
	V6	-17	-16.5	18.5	30	-12	-14	22	14	-11.5	-13	12	9
CIP 08	V2	-4.5	-12	10.4	19.8	-6.5	-3.8	21.7	13.5	-7	-11.2	18	16
	V3	-16.5	-29	30.6	60.9	-30	-11	26	21	-22	-19	30	22
CIP 09	V2	-6.3	-3.2	34.8	19.8	-7.2	-6	18	23	-15	-6.8	48	5.5
	V4	-6.3	-5.3	41.7	33	-9.2	-10.2	27	25	-16.8	-8.8	54	17.3
CIP 012	V2	-11	-11	9.7	8.2	-11	-5.5	16.2	6.2	-10	-12.5	10	12.9
	V3	-19.2	-12.8	27	29.3	-17	-12	12	27	-18	-17	21.4	18.3
CIP 013	V2	-5.7	-1.2	2	1.5	-11.4	-2.5	1.2	3	-16.1	-2.6	10	1
	V4	-34	-4.6	31	8	-18.3	-5	8	4	-17.1	-4.8	13	3.3
CIP 016	V2	-3.5	-3	7.2	20	-4	-1.6	10	9	-4	-14	4	8
	V6	-19.2	-40	32	22.3	-22	-8.2	26.3	23.2	-9.5	-17.8	36	23
CIP 017	V2	-3	-1.6	4	6	-4	-1	3.3	6.5	-4	-4.7	3	5
	V3	-3.6	-3.8	2.5	5.5	-5.2	-2.5	2.5	7.2	-5	-5.5	4.5	2
CIP 023	V2	-2.2	-5.5	2.7	4	-8.1	-0.5	6	2.6	-2.5	-10.2	7	9
	V5	-3.3	-5.5	16	14.4	-8	-0.6	14	14	-2.6	-10.2	13	18.4
CIP 024	V3	-0.8	-4.6	22	25	-4.7	-2	15.7	27.4	-7	-11	22.2	26
	V4	-4.7	-9	32	25	-15.	-15.6	25.5	24	-8.5	-17.5	26	31

CIP 025	V2	-5.2	-4	18	8.9	-6.8	-6.4	10	7	-2.8	-3.84	4	9.6
	V6	-15	-10.6	32	22	-15.2	-14	22	23	-14	-13	36.4	23
CIP 026	V2	-6.2	-1.8	3	4.3	-8	-6	2.5	11	-3	-5	7	8.2
	V5	-12	-17	19.2	27.8	-22.5	-15	44.7	20.2	-16.32	-12.2	32.5	21
CIP 028	V2	-5.6	-6.7	4.5	1.6	-1.6	-3.33	3.4	11	-4.4	-5.5	11.6	8
	V6	-18.8	-15	34	18	-17	-12.21	15	15	-15.6	-11	19.6	18.6
CIP 029	V2	-5.6	-4.5	-1.5	12.8	-6.5	-5	13.6	2.4	-6.8	-5.3	5.5	10.8
	V5	-13	-9.2	14.4	15	-12.4	-13	19.6	18.8	-20	-10.2	15.5	16
CIP 030	V2	-7.2	-2	3.5	2	-3.4	-1.2	3	7	-3.4	-2.8	0.8	2.1
	V6	-13.2	-9.3	32	11.7	-11	-7.6	21.6	13	-10.6	-9.2	28	14
CIP 031	V3	-5.3	-6.7	5	2	-5.6	-6.7	3.5	10	-5.6	-5.6	12.6	6
	V6	-22.4	-16.2	32	17	-22.4	-15.3	16	15	-16	-11.2	20	19.6
CIP 032	V2	-9	-1.2	14.5	6	-1	-4	8.5	8	-2.2	-5.6	8	9
	V6	-17	-16	22	15	-16.3	-12.3	20	15	-16	-13	21	20

Table 4.3
Overall Percent Change in Dominant DMD Modes and Eigenvalues Per Patient Among Visits

		DMD mag.	**Eigenvalues**	**DMD mag.**	**Eigenvalues**
CIP 05	AVG	-12.7	18.4	-11.1	21.1
	STD	7.6	12.3	7.4	11.5
CIP 06	AVG	-8.8	12.1	-7.8	11.5
	STD	5.6	5.2	4.6	7.1
CIP 08	AVG	-14.4	22.8	-14.3	25.5
	STD	9.3	7.1	7.9	16.1
CIP 09	AVG	-10.4	36.5	-7	20.5
	STD	4.6	12.4	2.3	7.6
CIP 012	AVG	-14.4	16.1	-11.8	17
	STD	3.8	6.3	3.4	8.8
CIP 013	AVG	-15.5	12.1	-4	3.4
	STD	7.7	9.8	1.5	2.2
CIP 016	AVG	-11.2	27.2	-13.8	20.5
	STD	6.5	11	12	6.6
CIP 017	AVG	-4.1	3.3	-3.2	5.4
	STD	0.8	0.7	1.6	1.7
CIP	AVG	-6.7	9.2	-6.3	12.6

023	STD	3.1	5	3.6	5.5
CIP	AVG	-6.8	23.9	-10	26.4
024	STD	4.4	4.9	5.5	2.3
CIP	AVG	-10.1	21.7	-9.3	19.2
025	STD	3.3	8.9	2.7	5.8
CIP	AVG	-10.6	20.5	-9.8	17.2
026	STD	5.4	13.5	4.4	6.4
CIP	AVG	-10.9	17	-9.4	11.9
028	STD	4.7	7.9	3.1	4.7
CIP	AVG	-10.7	11.7	-9.3	12.4
029	STD	3.9	5.8	3.3	4.3
CIP	AVG	-8.6	15.4	-5.8	9.3
030	STD	3	9.3	2.9	4.9
CIP	AVG	-11.9	15.4	-10.3	12.5
031	STD	7.2	6.7	4.8	4.3
CIP	AVG	-9	15.2	-8.1	12.5
032	STD	5.7	4.6	4.2	4.8

Table 4.4
Percent Change in Dominant DMD Modes' Magnitude For All Patients

		Heel		meta		BT	
		LF	RF	LF	RF	LF	RF
Second visit	AVG	-6.1	-4.3	-5.5	-3.5	-6.4	-7.2
	STD	3	3.2	3.1	2.2	4.3	3.7
Last visit	AVG	-15.3	-13.5	-15.2	-10.3	-14	-12.8
	STD	7.8	8.5	8.3	4.3	5.1	5

Table 4.5
Percent Change in Dominant DMD Eigenvalues For All Patients

		Heel		Meta		BT	
		LF	RF	LF	RF	LF	RF
Second visit	AVG	8.4	10.3	6.4	3.8	10.32	9.24
	STD	8.7	7.2	3.7	2.5	11.6	6
Last visit	AVG	36	24.5	22.1	17.6	24.7	18
	STD	10.5	13.7	10.8	7	12.1	9.1

4.4.4 Conclusion

The impact of neurotoxic chemotherapy treatment on plantar pressure variation among female uterine cancer patient footfall was investigated. Heel, metatarsal, and big toe areas of a visit-to-visit, foot plantar pressure variation was modeled and analyzed. Data was gathered from patients walking on a 20-ft high-resolution

Tekscan Strideway mat scan system. An innovative image processing-based segmentation technique was used to quickly and accurately extract studied footstep areas. Plantar pressure fluctuation between baseline and successive visits was successfully modeled and quantified using a DMD modeling technique. The magnitude of dominant DMD modes (i.e., eigenvectors) and DMD eigenvalues was utilized to quantify variation. Results demonstrated that the instability in walking behavior grew as chemotherapy treatment progressed. As a result of treatment, the dominating frequency domain DMD components had higher oscillation periods and lost strength. Findings support the hypothesis that the developed CIPN from chemotherapy treatment increases variability of plantar pressure and instability in walking behavior. Overall, the implementation of DMD in this study provides a promising approach for analyzing complex data sets and could have important applications in the field of rehabilitation for improving the quality of life for cancer patients undergoing chemotherapy treatment.

Chapter 5 Conclusion

5.1 Conclusion

The exponential growth of available experimental, simulation, and historical data from modern systems (e.g., medical and wireless networks) has created a persistent need for effective data mining and analysis techniques. Such systems can be characterized as high-dimensional, nonlinear dynamical schemes that exhibit rich multiscale phenomena in both space and time. The primary objective of this work was to characterize, identify, and predict the behavior of a system. Characterization and identification required finding patterns in the data, and prediction entailed predicting system dynamics. The field of data-driven modeling and analysis of complex systems is rapidly advancing and holds massive potential for revolutionizing the engineering, biological, and physical sciences. Modeling techniques generate low-dimensional representations of the system using extracted measurements, and then subsequently evaluate spatial-temporal structures in the data to characterize the system. These techniques enable modeling of complex systems without requiring knowledge of the dynamic equations governing the system's operation.

This dissertation proposed the implementation of DMD, which is a fully data-driven technique for characterizing dynamical systems from extracted measurements. Contextual application was in the fields of wireless communication and CIPN identification for cancer patients. DMD employes SVD to reduce high-dimensional measurements collected from a system and compute eigenvalues/eigenvectors of a linear approximated model. By estimating the underlying dynamics within a system, DMD provides a powerful tool for system characterization without requiring knowledge of the governing dynamical equations.

Three novel techniques based on DMD were developed for wireless coexistence analysis, with potential applications in wireless communication. The DMD-BW technique identified signals by evaluating the values of the resulting DMD modes' frequency spectrum bandwidth. A DMDA technique was based on evaluating a template features matrix obtained for a specific signal class, and then classifying signals under evaluation according to the values of the resulting projected DMD mode amplitude. The DMDF technique classified signals based on evaluating the slope of the DMD modes oscillation frequency trend. These techniques can differentiate various wireless technologies, including GSM and LTE signals in the cellular domain, IEEE802.11n, ac, and ax in the Wi-Fi domain, as well as Bluetooth and Zigbee. By capturing embedded periodic features transmitted within the signal, the proposed DMD-based technique identifies the time domain signature of a signal. Additionally, a DMD-based scheme was developed to capture the pattern of plantar pressure variability as it changes proportional to the development of neuropathy as a result of the effects of neurotoxic chemotherapy treatment. The developed technique modeled gait pressure variations across steps at three plantar regions to characterize the development of CIPN in patients with uterine cancer. The technique utilized magnitude of dominant DMD modes (i.e., eigenvectors) and DMD eigenvalues for quantifying variation.

When compared with various similar techniques implemented in the literature (i.e., ML-, DL-, and statistical-based methods), results showed that DMD-based methods had lower complexity and achieved higher performance with the advantages of fast data processing, minimal required data preprocessing, and minimal required signal observation time intervals.

The novel DMD-based algorithms differentiated and classified wireless signals with high accuracy by employing short observation intervals (e.g., four-time slots or packets), which enabled them to be implemented in real-time to identify various operating wireless technologies coexisting in heterogeneous networks. The DMDF scheme outperformed all compared techniques, as it is a direct

identification scheme (i.e., no training required). This technique achieved the highest accuracy—greater than 90% for most cases—and the shortest time required—less than one second-to identify a signal. Also, plantar pressure fluctuation between baseline and successive visits was successfully modeled and quantified using a DMD modeling technique. Results demonstrated that walking behavior instability grew as chemotherapy treatment progressed. As a result of treatment, the dominating frequency domain DMD components had higher oscillation periods (reduced decay rate) and lost strength. Findings support the hypothesis that CIPN as a result of chemotherapy treatment increases variability of plantar pressure and instability in walking behavior.

5.2 Future Work

The study in this dissertation provides a promising method to further research for developing innovative techniques to identify and characterize complex signals. The findings have important implications in the field of wireless identification, as further investigation can be conducted to evaluate the scalability of the developed algorithms for tracking additional wireless networks with more diverse coexistence scenarios. Moreover, this study provides a foundation for ongoing research related to plantar pressure analysis for CIPN identification. In particular, future investigations can explore the unique patterns of plantar pressure variability in the transfer of weight from step to step, which may be used for individual identification. Additional work can also be utilized to evaluate the level of asymmetry between the left and right foot, which could serve as a parameter to identify the advancement of neuropathy.

Bibliography

[1] H. T. Reda, A. Anwar, A. Mahmood and N. Chilamkurti, “Data-driven Approach for State Prediction and Detection of False Data Injection Attacks in Smart Grid,” in *Journal of Modern Power Systems and Clean Energy*, vol. 11, no. 2, pp. 455-467, March 2023.

[2] S. L. Brunton and J. N. Kutz, “Data-driven science and engineering: Machine learning, dynamical systems, and control,” Cambridge University Press, 2022.

[3] B. O. Koopman, "Hamiltonian systems and transformation in Hilbert space", *Proc. Nat. Acad. Sci. United States America*, vol. 17, no. 5, pp. 315-318, 1931.

[4] I. Mezić and A. Banaszuk, "Comparison of systems with complex behavior", *Physica D: Nonlinear Phenomena*, vol. 197, no. 1-2, pp. 101-133, 2004.

[5] P. J. Schmid, K. E. Meyer and O. Pust, "Dynamic mode decomposition and proper orthogonal decomposition of flow in a lid-driven cylindrical cavity", *Proc. 8th Int. Symp. Part. Image Velocimetry*, 2009.

[6] S. Lall, J. E. Marsden and S. Glavaški, "Empirical model reduction of controlled nonlinear systems", *IFAC Proc.*, vol. 32, no. 2, pp. 2598-2603, 1999.

[7] I. Mezić, "Analysis of fluid flows via spectral properties of the Koopman operator", *Annu. Rev. Fluid Mechanics*, vol. 45, pp. 357-378, 2013.

[8] N. Parmar, H. H. Refai, and T. Runolfsson, "A survey on the methods and results of data-driven Koopman analysis in the visualization of dynamical systems," *IEEE Transactions on Big Data*, vol. 8, no. 3, pp. 723-738, 2020.

[9] P. J. Schmid, K. E. Meyer and O. Pust, "Dynamic mode decomposition and proper orthogonal decomposition of flow in a lid-driven cylindrical cavity", *Proc. 8th Int. Symp. Part. Image Velocimetry*, 2009.

[10] A. Mauroy, I. Mezic, and J. Moehlis, "Isostables, isochrons, and Koopman spectrum for the action-angle representation of stable fixed point dynamics," *Physica D: Nonlinear Phenomena*, vol. 261, pp. 19-30, 2013.

[11] M. Budisic, R. Mohr, and I. Mezic, "Applied Koopmanism," *Chaos: An Interdisciplinary Journal of Nonlinear Sci.*, vol. 22, no. 4, 2012.

[12] A. Mauroy and I. Mezic, "On the use of Fourier averages to compute the global isochrons of (quasi) periodic dynamics," *Chaos: An Interdisciplinary Journal Nonlinear Sci.,* vol. 22, no. 3, 2012.

[13] G. Froyland, G. A. Gottwald, and A. Hammerlindl, "A computational method to extract macroscopic variables and their dynamics in multiscale systems," *SIAM Journal of Appl. Dynamical Syst.*, vol. 13, no. 4, pp. 1816-1846, 2014.

[14] E. M. Bollt and N. Santitissadeekorn, “Applied and computational measurable dynamics,” *Society for Industrial and Applied Mathematics*., vol. 18, pp. 64-93, 2013.

[15] Y. Susuki and I. Mezic, "A prony approximation of Koopman mode decomposition," *Proc. Decision and Control (CDC)*, 2015, pp. 7022-7027.

[16] S. Klus, P. Koltai, and C. Schütte, "On the numerical approximation of the Perron-Frobenius and Koopman operator," *Journal of Comput. Dyn.*, vol. 3, no. 1, pp. 51-79, 2016.

[17] P. J. Schmid, "Dynamic mode decomposition and its variants," *Annual Rev. of Fluid Mech.*, vol. 54, pp. 225-254, 2022.

[18] P. Schmid, L. Li, M. Juniper, and O. Pust, "Applications of the dynamic mode decomposition," *Theor. Comput. Fluid Dyn.,* vol. 25, pp. 249-259, 2011.

[19] Y. Liu, Q. Wu, B. Huang, H. Zhang, W. Liang, and G. Wang, "Decomposition of unsteady sheet/cloud cavitation dynamics in fluid-structure interaction via POD and DMD methods," *Intern. Journal of Multiphase Flow*, vol. 142, p. 103690, 2021.

[20] A. Goza and T. Colonius, "Modal decomposition of fluid-structure interaction with application to flag flapping*," Journal of Fluids and Struct.*, vol. 81, pp. 728-737, 2018.

[21] I. U. Haq, K. Fujii, and Y. Kawahara, "Dynamic mode decomposition via dictionary learning for foreground modeling in videos," *Comput. Vision and* Image Unders., vol. 199, p. 103022, 2020.

[22] S. Athisha, K. Keerthi Krishnan, and P. S. Sreelekshmi, "Separating Moving Objects from Stationary Background using Dynamic Mode Decomposition," *Intern. Journal of Scien. Res. in Network Security and Commun.*, vol. 6, no. 3, pp. 58-64, 2018.

[23] S. Tirunagari, N. Poh, M. Bober and D. Windridge, "Can DMD obtain a Scene Background in color?," *2016 Intern. Conf. on Image, Vision and Comput. (ICIVC)*, Portsmouth, UK, 2016, pp. 46-50.

[24] S. Tirunagari, N. Poh, D. Windridge, A. Iorliam, N. Suki and A. T. S. Ho, "Detection of Face Spoofing Using Visual Dynamics," in *IEEE Trans. on Inf. Forensics and Security*, vol. 10, no. 4, pp. 762-777, April 2015.

[25] S. Tirunagari, N. Poh, M. Bober and D. Windridge, "Windowed DMD as a microtexture descriptor for finger vein counter-spoofing in biometrics," *2015 IEEE Intern. Workshop on Inf. Forensics and Security (WIFS)*, Rome, Italy, 2015, pp. 1-6.

[26] B. W. Brunton, L. A. Johnson, J. G. Ojemann, and J. N. Kutz, "Extracting spatial-temporal coherent patterns in large-scale neural recordings using dynamic mode decomposition," *Journal of neuroscience methods*, vol. 258, pp. 1-15, 2016.

[27] S. Martínez, A. Silva, D. García-Violini, J. Piriz, M. Belluscio, and R. Sánchez-Peña, "Classification based on dynamic mode decomposition applied to brain recognition of context," *Chaos, Solitons & Fractals*, vol. 150, p. 111056, 2021.

[28] K. Fujii, N. Takeishi, B. Kibushi, M. Kouzaki, and Y. Kawahara, "Data-driven spectral analysis for coordinative structures in periodic human locomotion," *Scien. reports*, vol. 9, no. 1, p. 16755, 2019.

[29] N. J. Linden, D. R. Tabuena, N. A. Steinmetz, W. J. Moody, S. L. Brunton, and B. W. Brunton, "Go with the FLOW: visualizing spatiotemporal dynamics in optical widefield calcium imaging," *Journal of the Royal Society Interf.*, vol. 18, no. 181, p. 20210523, 2021.

[30] A. Arzani and S. T. Dawson, "Data-driven cardiovascular flow modelling: examples and opportunities," Journal of the Royal Society Interf., vol. 18, no. 175, p. 20200802, 2021.

[31] Kutz, J. Nathan, Steven L. Brunton, Bingni W. Brunton, and Joshua L. Proctor, Dynamic mode decomposition: data-driven modeling of complex systems, *USA: Society for Ind. and App. Math. (SIAM)*, 2016. Accessed on: Jan. 28, 2022. [Online]Available: https://epubs.siam.org/doi/book/10.1137/1.9781611974508

[32] Wu, Z., Laurence, D., Utyuzhnikov, S., & Afgan, I., "Proper orthogonal decomposition and dynamic mode decomposition of jet in channel crossflow," *Nuclear Eng. and Design*, vol. 344, pp. 54–68, 2019.

[33] P. J. Schmid and J. Sesterhenn, "Dynamic mode decomposition of numerical and experimental data, *Jour. of Fluid Mech.*, vol. 656, pp. 5-28, 2010.

[34] A. A. Kaptanoglu, K. D. Morgan, C. J. Hansen, and S. L. Brunton, "Characterizing magnetized plasmas with dynamic mode decomposition," *Phy. of Plasmas*, vol. 27, no. 3, p. 032108, 2020.

[35] J. H. Tu, "Dynamic mode decomposition: Theory and applications," Ph.D. dissertation, Princeton University, 2013.

[36] S. L. Brunton, "Notes on Koopman Operator Theory," Universität von Washington, Department of Mechanical Engineering, Zugriff, 2019.

[37] K. Tekbiyik, Ö. Akbunar, A. R. Ekti, A. Görçin and G. Karabulut Kurt, "Multi–Dimensional Wireless Signal Identification Based on Support Vector Machines," *IEEE Access*, vol. 7, pp. 138890-138903, 2019.

[38] X. Li, F. Dong, S. Zhang, and W. Guo, "A survey on Deep Learning techniques in wireless signal recognition," *Wireless Comm. and Mobile Comput.*, vol. 2019, pp. 1-12, 2019.

[39] N. Kato, B. Mao, F. Tang, Y. Kawamoto and J. Liu, "Ten Challenges in Advancing Machine Learning Technologies toward 6G," IEEE Wireless Comm., vol. 27, no. 3, pp. 96-103, June 2020.

[40] N. Bitar, S. Muhammad and H. H. Refai, "Wireless technology identification using deep Convolutional Neural Networks, In *Proc. 2017 IEEE 28th Annual Int. Symp. on Personal, Indoor, and Mobile Radio Commun. (PIMRC)*, Montreal, Canada, 2018, pp. 1-6.

[41] S. Sun, L. Gong, B. Rong and K. Lu, "An intelligent SDN framework for 5G heterogeneous networks," *IEEE Commun. Mag.*, vol. 53, no. 11, pp. 142-147, Nov. 2015.

[42] K. Tekbıyık, O. Akbunar, A. R. Ekti, G. K. Kurt and A. Gorcin, "On the Investigation of Wireless Signal Identification Using Spectral Correlation Function and SVMs," in *Proc. 2019 IEEE Wireless Commun. and Net. Conf. (WCNC)*, Marrakesh, Morocco, 2019, pp. 1-5.

[43] C. Skiribou and F. Elbahhar, "V2X wireless technology identification using time–frequency analysis and random forest classifier," *Sensors*, vol. 21, no. 13, p. 4286, 2021.

[44] Baiqin Liu and K. C. Ho, "Identification of CDMA signal and GSM signal using the wavelet transform," in *Proc. 42nd Midwest Symp. on Circ. And Sys*., Las Cruces, NM, USA, 1999, pp. 678-681.

[45] K. C. Ho, Haiqin Liu and Liang Hong, "On improving the accuracy of a wavelet based identifier to classify CDMA signal and GSM signal," in *Proc. 1999 IEEE Int. Symp. on Circ. and Sys.*, Orlando, FL, USA, 1999, pp. 564-567.

[46] K. C. Ho,W. Prokopiw, and Y. T. Chan, "Modulation identification by the wavelet transform," in *Proc. IEEE Mil. Commun. Conf. (MILCOM)*, vol. 2, Nov. 1995, pp. 886_890.

[47] L. Hong and K. C. Ho, "Identification of digital modulation types using the wavelet transform," in *Proc. IEEE Mil. Commun. Conf. (MILCOM),* vol. 1, Nov. 1999, pp. 427_431.

[48] M. Oner and F. Jondral, "Cyclostationarity based air interface recognition for software radio systems," in *Proc. 2004 IEEE Radio and Wireless Conf.*, Atlanta, GA, USA, 2004, pp. 263-266.

[49] E. Karami, O. A. Dobre and N. Adnani, "Identification of GSM and LTE signals using their second-order cyclostationarity," in Proc. IEEE Int. Inst. and Meas. Tech. Conf., Pisa, Italy, 2015, pp. 1108-1112.

[50] M. Kulin, T. Kazaz, I. Moerman and E. De Poorter, "End-to-End Learning from Spectrum Data: A Deep Learning Approach for Wireless Signal Identification in Spectrum Monitoring Applications," *IEEE Access*, vol. 6, pp. 18484-18501, 2018.

[51] G. C. Zanuz, J. M. Winter, I. Muller, J. L. T. Garzon, J. C. Netto and C. E. Pereira, "Identification of IEEE 802.11g and IEEE 802.15.4 signals using energy and cyclostationarity detection approach," in *Proc. 2016 1st Int. Symp. on Inst. Sys., Circ. and Trans. (INSCIT)*, Belo Horizonte, Brazil, 2016, pp. 55-60.

[52] Y. A. Eldemerdash, O. A. Dobre, O. Ureten and T. Yensen, "Fast and robust identification of GSM and LTE signals," in *Proc. 2017 IEEE Int. Inst. And Meas. Tech. Conf. (I2MTC)*, Turin, Italy, 2017, pp. 1-6.

[53] Y. A. Eldemerdash, O. A. Dobre, O. Ureten and T. Yensen, "Identification of Cellular Networks for Intelligent Radio Measurements," *IEEE Trans. on Inst. and Meas.*, vol. 66, no. 8, pp. 2204-2211, Aug. 2017.

[54] W. Xiao, Z. Luo, and Q. Hu, "A Review of Research on Signal Modulation Recognition Based on Deep Learning," *Electronics*, vol. 11, no. 17, p. 2764, Sep. 2022.

[55] Xia, H., Alshathri, K., Lawrence, V. B., Yao, Y. D., Montalvo, A., Rauchwerk, M., & Cupo, R., "Cellular Signal Identification Using Convolutional Neural Networks: AWGN and Rayleigh Fading Channels," in *Proc. 2019 IEEE Int. Symp. on Dyn. Spec. Access Net. (DySPAN)*, NJ, USA, 2019, pp. 1-5.

[56] K. Alshathri, H. Xia, V. Lawrence and Y. D. Yao, "Cellular System Identification Using Deep Learning: GSM, UMTS and LTE," in *Proc. 2019 28th Wireless and Opt. Commun. Conf. (WOCC)*, Beijing, China, 2019, pp. 1-4.

[57] H. Gu, Y. Wang, S. Hong, Y. Xu and G. Gui, "Deep Learning based Intelligent Recognition Method in Heterogeneous Communication Networks," in *Proc. IEEE/CIC Int. Conf. on Commun. (ICCC)*, Chongqing, China, 2020, pp. 478-482.

[58] M. Schmidt, D. Block and U. Meier, "Wireless interference identification with convolutional neural networks," in *Proc. 2017 IEEE 15th Int. Conf. on Ind. Inf. (INDIN)*, Emden, Germany, 2020, pp. 478-482.

[59] J. Fontaine, E. Fonseca, A. Shahid, M. Kist, L. A. DaSilva, I. Moerman, and E. De Poorter, "Towards low-complexity wireless technology classification across multiple environments," *Ad Hoc Net.*, vol. 91, p. 101881, 2019.

[60] E. Almazrouei, G. Gianini, N. Almoosa, and E. Damiani, "Robust computationally-efficient wireless emitter classification using autoencoders and Convolutional Neural Networks," *Sensors*, vol. 21, no. 7, p. 2414, 2021.

[61] R. J. Estes, D.Willis and H. H. Refai, "Classifying Wi-Fi from Raw Power Measurements using a Neural Network Adapted from WaveNet," in *Proc. ICC 2021 - IEEE Int. Conf. on Commun*., Montreal, Canada, 2021, pp. 1-6.

[62] J. Gong, X. Qin and X. Xu, "Multi-Task Based Deep Learning Approach for Open-Set Wireless Signal Identification in ISM Band," *IEEE Trans. On Cogn. Commun. and Net.*, vol. 8, no. 1, pp. 121-135, March 2022.

[63] M. He, S. Peng, H. Wang and Y. D. Yao, "Identification of ISM Band Signals Using Deep Learning," in *Proc. 2020 29th Wireless and Opt. Commun. Conf. (WOCC)*, NJ, USA, 2020, pp. 1-4.

[64] Ghanem, H.S., Al-Makhlasawy, R.M., El-Shafai, W., Elsabrouty, M., Hamed, H.F., Salama, G.M. and El-Samie, F.E.A, "Wireless modulation classification based on Radon transform and convolutional neural networks," *Journal of Ambient Intel. and Hum. Comp*., pp. 1-10, 2022.

[65] C. T. Fredieu, A. Martone, and R. M. Buehrer, "Open-set Classification of Common Waveforms Using A Deep Feed-forward Network and Binary Isolation Forest Models," in *Proc. 2022 IEEE Wireless Commun. and Net. Conf. (WCNC)*, Austin, TX, USA, 2022, pp. 2465-2469.

[66] K. S. Durbha and S. Amuru, "AutoML Models for Wireless Signals Classification and their effectiveness against Adversarial Attacks," in *Proc. 2022 14th Int. Conf. on Commun. Sys. & NET. (COMSNETS)*, Bangalore, India, 2022, pp. 265-269.

[67] R. Du, F. Liu, J. Xu, F. Gao, Z. Hu, and A. Zhang, "D-GF-CNN Algorithm for Modulation Recognition," *Wireless Personal Communications*, vol. 124, no. 2, pp. 989–1010, Jan. 2022.

[68] H.-K. Le, V.-S. Doan, and V.-P. Hoang, "Ensemble of Convolution Neural Networks for Improving Automatic Modulation Classification Performance," *Journal of Science and Tech. Issue on Inf. and Commun. Tech*., pp. 25–32, Jun. 2022.

[69] L. Wang and Y. Ren, "Recognition of digital modulation signals based on high order cumulants and support vector machines," in *Proc. 2009 ISECS Int. Colloq. on Comp., Commun., Cont., and Manag.*, Sanya, China, 2009, pp. 271-274.

[70] X. Wang, Z. Gao, Y. Fang, S. Yuan, H. Zhao, W. Gong, M. Qiu, and Q. Liu, "A signal modulation type recognition method based on kernel PCA and Random

Forest in cognitive network,” in *Proc. Intel. Comp. Method*., 2014, pp. 522-528.

[71] A. N. Mody et al., ” Recent advances in cognitive communications,” *IEEE Commun. Mag.*, vol. 45, no. 10, pp. 54-61, October 2007.

[72] N. Shetty, S. Pollin and P. Pawelczak, "Identifying Spectrum Usage by Unknown Systems using Experiments in Machine Learning,"in *proc. 2009 IEEE Wireless Communications and Networking Conference*, Budapest, Hungary, 2009, pp. 1-6.

[73] S. Grimaldi, A. Mahmood and M. Gidlund, “Real-Time Interference Identification via Supervised Learning: Embedding Coexistence Awareness in IoT Devices,” *IEEE Access*, vol. 7, pp. 835-850, 2019.

[74] Z. Wu, S. Zhou, Z. Yin, B. Ma and Z. Yang, "Robust Automatic Modulation Classification Under Varying Noise Conditions," *IEEE Access*, vol. 5, pp. 19733-19741, 2017.

[75] T. A. Almohamad, M. F. Mohd Salleh, M. N. Mahmud and A. H. Y. Sa’D, "Simultaneous Determination of Modulation Types and Signal-to-Noise Ratios Using Feature-Based Approach," *IEEE Access*, vol. 6, pp. 9262-9271, 2018.

[76] S. Ansari, K. A. Alnajjar, M. Saad, S. Abdallah and A. A. El-Moursy, "Automatic Digital Modulation Recognition Based on Genetic-Algorithm-Optimized Machine Learning Models," *IEEE Access*, vol. 10, pp. 50265-50277, 2022.

[77] Fujii and Y. Kawahara, “Dynamic mode decomposition in vector-valued reproducing kernel Hilbert spaces for extracting dynamical structure among observables,” *Neural Net.,* vol. 117, pp. 94-103, 2019.

[78] S. Zhou, G. Lin, Q. Qian, and C. Xu, "Binary classification of floor vibrations for human activity detection based on dynamic mode decomposition," *Neurocomputing*, vol. 432, pp. 227–239, Apr. 2021.

[79] Tekbıyık, O. Akbunar, A. R. Ekti, G. Karabulut Kurt, and A. G¨orc, Standard-based Wireless Signals. Accessed on: Feb. 2022. [Online] Available: https://data.mendeley.com/datasets.

[80] Chaari, Lamia, and L. Kamoun, "Performance analysis of IEEE 802.15.4 Zigbee standard under real time constraint," *Int. Jour. of Comp. Net. & Commun*., 2011.

[81] Bluetooth Low Energy–It Starts with Advertising. Accessed on: April. 2021. [Online] Available: https://www.bluetooth.com/blog/.

[82] GSM technical specification. Accessed on: Jan. 2022. [Online] Available: https://www.etsi.org/committee/3gpp.

[83] LTE Frame Structure Made Simple. Accessed on: Jan. 2022. [Online] Available: https://ourtechplanet.com/lte-frame-structure-made-simple/.

[84] Sung-won Kim and Kun-yong Kim, "Physical layer verification for 3GPP (FDD)," in *Proc. 2009 11th Int. Conf. on Adv. Commun.Tech.*, 2009, pp. 1095-1100.

[85] Using ResNet for image classification. Accessed on: March. 2021. [Online] Available: https://blog.jovian.ai/using-resnet-for-image-classification-4b3c42f2a27e.

[86] C. Yang, C. Yang, Z. Chen and N. Lo, "Multivariate Time Series Data Transformation for Convolutional Neural Network," in *Proc. 2019 IEEE/SICE Int. Symp. on Sys. Integ. (SII)*, Paris, France, 2019, pp. 188- 192.

[87] Duchi, John, Elad Hazan, and Yoram Singer, "Adaptive subgradient methods for online learning and stochastic optimization," *Journal of machine learn. res.*, no. 7, 2011.

[88] Vaswani, A., Shazeer, N., Parmar, N., Uszkoreit, J., Jones, L., Gomez, A.N., Kaiser, Ł. and Polosukhin, I., "Attention is all you need," in *Proc. Adv. in Neural Inf. Procss. Sys. 30 (NIPS 2017)*, CA, USA, 2017.

[89] S. Hussain, M. Javaheripi, P. Neekhara, R. Kastner and F. Koushanfar, " FastWave: Accelerating Autoregressive Convolutional Neural Networks on FPGA," in *Proc. 2019 IEEE/ACM Int. Conf. on Comp.-Aided Design (ICCAD)*, CO, USA, 2019, pp. 1-8.

[90] National Cancer Institute, Age and Cancer Risk. Accessed on: May. 2021 [Online] Available: https://www.cancer.gov/about-cancer/causes prevention/risk/age.

[91] B.D. Smith, G.L. Smith, A. Hurria, G.N. Hortobagyi, T.A. Buchholz, "Future of cancer incidence in the United States: burdens upon an aging, changing nation," *Journal of Clinical Oncology*, vol. 27, no. 17, pp. 2758–2765, Jun. 2009.

[92] A. Hurria, S. Mohile, A. Gajra, H. Klepin, H. Muss, A. Chapman, et al., "Validation of a prediction tool for chemotherapy toxicity in older adults with cancer," *Journal of Clinical Oncology*, vol. 34, no. 20, pp. 2366–2371, Jul. 2016.

[93] T. Kalsi, G. Babic-Illman, P.J. Ross, N.R. Maisey, S. Hughes, P. Fields, et al., "The impact of comprehensive geriatric assessment interventions on tolerance to chemotherapy in older people," *British Journal of Cancer*, vol. 112, pp. 1435, 2015.

[94] Bulls, Hailey W., et al., "A longitudinal examination of associations between age and chemotherapy-induced peripheral neuropathy in patients with gynecologic cancer," *Gynecologic Oncology*, vol. 152, no. 2, pp. 310-315, 2019.

[95] H.B. Muss, D.A. Berry, C. Cirrincione, D.R. Budman, I.C. Henderson, M.L. Citron, et al., "Toxicity of older and younger patients treated with adjuvant chemotherapy for node-positive breast cancer: the cancer and leukemia group b experience," *Journal of Clinical Oncology*, vol. 25, no. 24, pp. 3699–3704, Aug. 2007.

[96] S.M. Lichtman, A. Hurria, C.T. Cirrincione, A.D. Seidman, E. Winer, C. Hudis, et al., "Paclitaxel efficacy and toxicity in older women with metastatic breast cancer: combined analysis of CALGB 9342 and 9840," *Annals of Oncology*, vol. 23, no. 3, pp. 632–638 , Mar. 2012.

[97] T. Kalsi, G. Babic-Illman, P. Fields, S. Hughes, N. Maisey, P. Ross, et al., "The impact of low-grade toxicity in older people with cancer undergoing chemotherapy," *British Journal of Cancer*, vol. 111, pp. 2224, 2014.

[98] S. Quasthoff and H.P. Hartung, "Chemotherapy-induced peripheral neuropathy," *Journal of Neurology*, vol. 249, no. 1, pp. 9–17, Jan. 2002.

[99] T.F. Marshall, G.P. Zipp, F. Battaglia, R. Moss and S. Bryan, "Chemotherapy-induced-peripheral neuropathy, gait and fall risk in older adults following cancer treatment," *Journal of Cancer Res. and Prac.,* vol. 4, no. 4, pp. 134–138, Dec. 2017.

[100] M. Sasane, T. Tencer, A. French, T. Maro and K. Beusterien, "Patient-reported outcomes in chemotherapy-induced peripheral neuropathy: A review," *Journal of Supp. Oncology*, vol. 8, no. 6, pp. e15–e21, Dec. 2010.

[101] N.Kerckhove et al., "Long-term effects, pathophysiological mechanisms, and risk factors of chemotherapy-induced peripheral neuropathies: a comprehensive literature review," *Frontiers in Pharmacology*, vol. 8, pp. 86 , Feb. 2017.

[102] G.Cavaletti et al., "Chemotherapy-induced neuropathy," *Curr. Treat. Options Neurol.*, vol. 13, no. 2 , pp.180–190 , May 2011.

[103] A.A.Argyriou et al., "Chemotherapy-induced peripheral neurotoxicity (CIPN): an update," *Crit. Rev. Oncol. Hematol.*, vol. 82, no .1, pp .51–77, May 2012.

[104] M.Seretny et al., "Incidence, prevalence,and predictors of chemotherapy-induced peripheral neuropathy: a systematic review and meta-analysis," Pain, vol .155 ,pp .2461–2470 , Dec .2014.

[105] K.A.Hartholt et al., "Societal consequences of falls in the older population: injuries, healthcare costs,and long-term reduced quality of life," *Journal of Trauma Acute Care Surg*., vol .71,no .3 ,pp .748–753 , Sep .2011.

[106] National Institute of Neurological Disorders and Stroke, "Peripheral Neuropathy Fact Sheet," Accessed on: May 2022 [Online] Available: https://www.ninds.nih.gov/Disorders/Patient-Caregiver-Education/Fact-Sheets/Peripheral-Neuropathy-Fact-Sheet#3208_4.

[107] Kang et al., "Does the presence of cognitive impairment exacerbate the risk of falls in people with peripheral neuropathy? An application of body-worn inertial sensors to measure gait variability," *Sensors*, vol .20, no .5, p.p 1328, Mar. 2020.

[108] H.Reimann et al., "Neural control of balance during walking," *Front Physiol.*, vol .9 ,p.p1271-71 , Sep .2018 .

[109] U.Alam et al., "Diabetic neuropathy and gait: a review," *Diabetes Ther*., vol .8, no .6, p.p1253–1264 , Dec .2017.

[110] T.Roman de Mettelinge et al., "The impact of peripheral neuropathy and cognitive decrements on gait in older adults with type 2 diabetes mellitus," *Arch. Phys. Med. Rehabil*., vol. 94, no. 6, p.p 1074–1079, Jun. 2013.

[111] M.L.Beaulieu et al., "Peripheral neuropathy is associated with more frequent falls in Parkinson's disease," *Parkinsonism Relat. Disord*., vol.54, no .6, p.p 46–50 , Jun. 2018.

[112] Hsieh et al., "Gait variability is altered in cancer survivors with self-reported neuropathy," *Gait & Posture,* vol. 72, no. 2, p.p 206-210, Nov. 2019 .

[113] Franco et al., "Within and between-days repeatability and variability of plantar pressure measurement during walking in children, adults, and older adults," Advances in Rheumatology, vol. 58, p.p10-1186/s42358-019-0097-9, Dec. 2019.

[114] H. Gaßner, et al., "Gait variability as digital biomarker of disease severity in Huntington's disease," *Journal of neurology*, vol. 267, no. 6, pp. 1594-1601, Jun. 2020.

[115] J. Barth, et al., "Stride segmentation during free walk movements using multi-dimensional subsequence dynamic time warping on inertial sensor data," *Sensors*, vol. 15, no. 3, pp. 6419-40, Mar. 2015.

[116] A. Rampp, J. Barth, S. Schülein, K.G. Gaßmann, J. Klucken, and B.M. Eskofier, "Inertial sensor-based stride parameter calculation from gait sequences in geriatric patients," IEEE Transactions on Biomedical Engineering, vol. 62, no. 4, pp. 1089-97, Apr. 2015.

[117] X. Tang et al., “Study on foot-type classification for young adults based on static and dynamic plantar pressure distribution,” *Advances in Mech. Eng*., vol. 14, no. 5, p. 168781322210979, May 2022.

[118] T.A. Bacarin, I.C.N. Sacco, and E.M. Hennig, "Plantar pressure distribution patterns during gait in diabetic neuropathy patients with a history of foot ulcers," *Clinics*, vol. 64, pp. 113-120, 2009.

[119] G. Zhang, et al., "Plantar Pressure Variability and Asymmetry in Elderly Performing 60-Minute Treadmill Brisk-Walking: Paving the Way towards Fatigue-Induced Instability Assessment Using Wearable In-Shoe Pressure Sensors," *Sensors*, vol. 21, no. 9, pp. 3217, Apr. 2021.

[120] A.M. Tan, et al., "Comparing the applicability of temporal gait symmetry, variability and laterality in bilateral gait conditions: A feasibility study of healthy individuals and people with diabetic neuropathy," *Clinical Biomechanics*, vol. 91, pp. 105530, Jan. 2022.

[121] L.-Y. Zhang, Q.-L. Liu, K.-L. Yick, J. Yip, and S.-P. Ng, “Analysis of Diabetic Foot Deformation and Plantar Pressure Distribution of Women at Different Walking Speeds*,” Int. Journal of Env. Research and Public Health*, vol. 20, no. 4, p. 3688, Feb. 2023.

[122] J. S. Park and C. H. Kim, “Ground-Reaction-Force-Based Gait Analysis and Its Application to Gait Disorder Assessment: New Indices for Quantifying Walking Behavior,” *Sensors*, vol. 22, no. 19, p. 7558, Oct. 2022.

[123] L. di Biase, L. Raiano, M. L. Caminiti, P. M. Pecoraro, and V. Di Lazzaro, “Parkinson’s Disease Wearable Gait Analysis: Kinematic and Dynamic Markers for Diagnosis,” *Sensors*, vol. 22, no. 22, p. 8773, Nov. 2022.

[124] F. Haque, et al., "Machine Learning-Based Diabetic Neuropathy and Previous Foot Ulceration Patients Detection Using Electromyography and Ground Reaction Forces during Gait," *Sensors*, vol. 22, no. 9, pp. 3507, Apr. 2022.

[125] S. Muralidhara, et al., "Holistic multi-class classification & grading of diabetic foot ulcerations from plantar thermal images using deep learning," *Health Inf. Science and Sys*., vol. 10, no. 1, pp. 1-9, Jan. 2022.

[126] Z. Song, et al., "Fall Risk Assessment for the Elderly Based on Weak Foot Features of Wearable Plantar Pressure," *IEEE Trans. on Neural Sys. and Rehab. Eng*., vol. 30, pp. 1060–1070, 2022.

[127] A.S. Alharthi, A.J. Casson, and K.B. Ozanyan, "Spatiotemporal Analysis by Deep Learning of Gait Signatures from Floor Sensors," *IEEE Sensors Journal*, vol. 21, no. 15, pp. 16904–16914, Aug. 2021.

[128] A.M. Boudali, P.J. Sinclair, R. Smith, and I.R. Manchester, "Human locomotion analysis: Identifying a dynamic mapping between upper and lower limb joints using the Koopman operator," in *Proc. Annual Int. Conf. of the IEEE Eng. in Med. and Biology Society*, vol. 2017, pp. 1889-1892, Jul. 2017.

[129] M. Zahiri, et al., "Using wearables to screen motor performance deterioration because of cancer and chemotherapy-induced peripheral neuropathy (CIPN) in adults—toward an early diagnosis of CIPN," *Journal of Geriatric Oncology*, vol. 10, no. 6, pp. 960-967, Nov. 2019.

[130] S. Vallabhajosula, C.D. Deaterly, and T.A. Madzima, "Comparison of forward and backward gait characteristics between those with and without a history of breast cancer," *Gait & Posture*, vol. 74, pp. 162-168, Dec. 2019.

[131] K.M. Winters-Stone, et al., "Falls, functioning, and disability among women with persistent symptoms of chemotherapy-induced peripheral neuropathy," *Journal of Clinical Oncology*, vol. 35, no. 23, pp. 2604-2612, Aug. 2017.

[132] J. Beulertz, W. Bloch, A. Prokop, V. Rustler, C. Fitzen, L. Herich, F.T. Baumann, "Limitations in ankle dorsiflexion range of motion, gait, and walking efficiency in childhood cancer survivors," *Cancer Nursing*, vol. 39, no. 2, pp. 117-124, March 2016.

[133] G.E. Kang, et al., "Digital biomarkers of poor gait and balance in diabetic foot, measurable by wearables: A review of literature," *Journal of Clinical Med.*, vol. 11, no. 3, pp. 1113, Feb. 2022.

[134] N.D. Reeves, G. Orlando, and S.J. Brown, "Sensory-motor mechanisms increasing falls risk in diabetic peripheral neuropathy," *Medicina*, vol. 57, no. 5, pp. 457, Apr. 2021.

[135] M.F. Corrà, et al., "Peripheral neuropathy in Parkinson's disease: prevalence and functional impact on gait and balance," *Brain*, vol. 145, no. 3, pp. 966-978, Mar. 2022.

[136] "Pressure Mapping, Force Measurement & Tactile Sensors", Accessed on: Jan. 2023 [Online] Available: https://www.tekscan.com/.

[137] M. Kelly, P. Jones, R. Wuebbles, V. Lugade, D. Cipriani, and N.G. Murray, "A novel smartphone application is reliable for repeat administration and comparable to the Tekscan Strideway for spatiotemporal gait," *Measurement*, vol. 192, pp. 110882, Jun. 2022.

[138] S. Alphonsa, R. Wuebbles, T. Jones, P. Pavilionis, and N. Murray, "Spatio-temporal gait differences in facioscapulohumeral muscular dystrophy during single and dual task overground walking-A pilot study," *Journal of Clinical and Trans. Res.*, vol. 8, no. 2, pp. 166-172, Apr. 2022.

[139] M. Chiarello, J. Lee, M.M. Salinas, R.C. Hilsabeck, J. Lewis-Peacock, and J. Sulzer, "The Effect of Biomechanical Features on Classification of Dual-Task Gait," *IEEE Sensors Journal*, vol. 23, no. 3, pp. 3079-3089, Feb. 2022.

[140] I-J. Ho, et al., "Comparison of plantar pressure distribution between different speed and incline during treadmill jogging," *Journal of Sports Science & Med.*, vol. 9, no. 1, pp. 154-159, March 2010.

[141] U.K. Hofmann, et al., "Transfer of plantar pressure from the medial to the central forefoot in patients with hallux valgus," *BMC Musculosk. Dis.*, vol. 20, no. 1, pp. 1-8, Jan. 2019.

Acronyms

BLE Bluetooth Low Energy

BT Big Toe

BW Band Width

CDF Cumulative Distribution Function

CIPN Chemotherapy Induced Peripheral Neuropathy

CNN Convolutional Neural Network

DC Duty Cycle

DL Deep Learning

DMD Dynamic Mode Decomposition

GSM Global System for Mobile communication

HL Lateral Heel

HM Medial Heel

LF Left Foot

LTE Long-Term Evolution

MF Midfoot

ML Machine Learning

PHY Physical Layer

PDF Probability Density Function

Rx Receiver

ResNet Deep Residual Network

RF Right Foot

SNR Signal to Noise Ratio

SVD Singular Value Decomposition

Tx Transmitter

Appendix

Footstep segmentation Code

Algorithm 4.1: Footstep extraction and identification

Input: Data tensor T
Output: Steps_start_end, LF_num , RF_num
Convert 3D input data tensor to 2D matrix:
1: Footsteps=sum(T,3);
Average footstep length in pixels:
2: footlength=52;
Column wise summation for Footsteps matrix:
3: Cols_sum=sum(Footsteps,1);
Find the start and end location for each footstep:
4: while(i>1) do
5: if Cols_sum(i)>0 do
6: step_xs=i;
7: step_xe=abs(step_xs-footlength)+1;
8: steps=[steps;step_xs step_xe];
9: i=step_xe;
10: end if
11: i=i-1;
12: end while
Identifying and numbering LF and RF footsteps:
Select a test footstep:
13: test_step = 4;
14: foot_step=
Footsteps (:,Steps_start_end(test_step,2):Steps_start_end(test_step,1));
Plot the identification line:
15: x1=round((size(foot_step,2)/2));
16: x2=size(foot_step,2);
17: C1=foot_step(:,x1);
18: C2=foot_step(:,x2);
19: for i=size(C1,1):-1:1 do
20: if C1(i)>0 do
21: y1=i;
22: break
23: end if
24: end for
25: for ii=size(C2,1):-1:1 do
26: if C2(ii)>0 do
27: y2=ii;
28: break
29: end if
30: end for
calculate the angle of the identification line:
31: angle=atan((y2-y1)/(x2-x1))*180/pi;
32: if angle>0 do
33: RF_num=2:2:size(Steps_start_end,1);
34: LF_num=1:2:size(Steps_start_end,1);
35: else
36: LF_num=2:2:size(Steps_start_end,1);
37: RF_num=1:2:size(Steps_start_end,1);
38: end if

Algorithm 4.2: Extracting main three segments of a footstep

Input: footstep

Output:

```
1: Calculate and plot footstep tangent baseline:
2: x1=find(footstep(end,:)>0);
3: x2=size(footstep,2);
4: C1=footstep(:,x1);
5: C2=footstep(:,x2);
6: for i=size(C1,1):-1:1 do
7:     if C1(i)>0 do
8:         y1=i;
9:         break
10:    end if
11: end for
12: for ii=size(C2,1):-1:1 do
13:    if C2(ii)>0 do
14:        y2=ii;
15:        break
16:    end if
17: end for
18: coefficients = polyfit([x1, x2], [y1, y2], 1);
19: m = coefficients (1)+0.001;
20: c = coefficients (2);
21: angle_baseline=abs(atan((y2-y1)/(x2-x1))*180/pi);
22: plot(foot_step)
23: hold on
24: plot ([x1, x2], [y1, y2])
Calculate and plot the footstep start line:
25: mp=-1/m; %perpendicular slope
26: l2_x = size(footstep,2);
27: l2_y = size(footstep,1)/2;
28: l3_x = l2_x-4;
29: l3_y = mp * (l3_x - l2_x) + l2_y;
30: l4_x = l2_x+12;
31: l4_y = mp * (l4_x - l2_x) + l2_y;
32: plot([l3_x, l4_x], [l3_y, l4_y], 'm', 'LineWidth', 1.5);
Calculate and plot the footstep end line:
33: sum_foot_col=sum(footstep,1);
34: e2_x=find(sum_foot_col>0);
35: [e2_y,~]=find(footstep(:,e2_x)>0);
36: e3_x = e2_x-4;
37: e3_y = mp * (e3_x - e2_x) + e2_y;
38: e4_x = e2_x+12;
39: e4_y = mp * (e4_x - e2_x) + e2_y;
40: plot([e3_x, e4_x], [e3_y, e4_y], 'm', 'LineWidth', 1.5);
Calculate and plot the Heel line:
41: heel_x=(-0.31/cos(angle*pi/180))*(xs_i-xe_i)+xs_i;
42: heel_y=m*heel_x+c+5;
43: m_heel=-1/m;
44: x11 = 20;
45: y11 = m_heel * (x11 - heel_x) + heel_y;
46: plot([x11, heel_x], [y11, heel_y], 'y', 'LineWidth', 1.5);
Heel line intersections coordinates with lines parallel to baeline tangent:
47: x1=[1 size(footstep,2)];
48: Initiate heel_int=[]
49: for i=1:size(footstep,1) do
50:    y1=[i i];
51:    [xi_heel,yi_heel] = polyxpoly(x1,y1,[x11  heel_x],[y11 heel_y]);
52:    heel_int=[heel_int;[xi_heel yi_heel]];
```

```
53: end for
Calculate and plot the Midfoot line:
54: midfoot_x=(-0.21/cos(angle*pi/180))*(xs_i-xe_i)+heel_x;
55: midfoot_y=m*midfoot_x+c;
56: m_midfoot=-1/m;
57: x12 = 10;
58: y12 = m_midfoot * (x12 - midfoot_x) + midfoot_y;
59: plot([x12, midfoot_x], [y12, midfoot_y], 'y', 'LineWidth', 1.5);
60: Midfoot line intersections coordinates with lines parallel to baseline tangent:
61: Initiate midfoot=[];
62: for i=1:size(footstep,1) do
63:     y1=[i i];
64:    [xi_midfoot,yi_midfoot] = polyxpoly(x1,y1,[x12  midfoot_x],[y12 midfoot_y]);
65:     midfoot_int=[midfoot_int;[xi_midfoot yi_midfoot]];
66: end for
Heel segment cropping
67: heel_segment= zeros(size(footstep,1), size(footstep,2));
68: for i=1:size(heel_int,1) do
69: heel_segment(heel_int_round(i,2),heel_int_round(i,1):end)=
footstep(heel_int_round(i,2), heel_int_round(i,1):end);
70: end for
Midfoot segment cropping
71: mf_size_x=round((0.21/cos(angle*pi/180))*(xs_i-xe_i));
72: midfoot_segment= zeros(size(footstep,1), size(footstep,2));
73: for i=1:size(midfoot_int,1) do
74:midfoot_segment(midfoot_int_round(i,2),
midfoot_int_round(i,1):midfoot_int_round(i,1)+mf_size_x)
=footstep(midfoot_int_round(i,2), midfoot_int_round(i,1):midfoot_int_round(i,1)+mf_size_x);
75: end for
Metatarsal+Toe segments cropping
76: metatarsal_segment= zeros(size(footstep,1), size(footstep,2));
77: for i=1:size(midfoot_int,1) do
78:   metatarsal_segment(midfoot_int(i,2), midfoot_int(i,1))
=footstep(midfoot_int(i,2), 1:midfoot_int(i,1));
79: end for
```

Algorithm 4.3: Heel Segmentation

Input: heel_segment, baseline slope m
Output: up_heel_segment, low_heel_segment

```
Plot Heel bisection line:
1: cc=round((size(heel_segment,1)/2)-m*(size(heel_segment,2)/2));
2: x=1:size(heel_segment,2);
3: y=round(m*x+cc);
4: y(y>size(heel_segment,1))=size(heel_segment,1);y(y<0)=0;
5: plot(x,y,'r','LineWidth',2)
Crop upper Heel segment:
6: up_heel_segment=zeros(size(heel_segment,1),size(heel_segment,2));
7: for i=1:length(y) do
8: up_heel_segment(1:y(i),i)= heel_segment(1:y(i),i);
9: end for
Crop lower Heel segment:
10: low_heel_segment=zeros(size(heel_segment,1),size(heel_segment,2));
11: for i=1:length(y)
12: low_heel_segment(y(i)+1:end,i)= heel_segment(y(i)+1:end,i);
13: end
```

Algorithm 4.4: Metatarsal-toes isolation

Input: metatarsal_segment
Output: toe_segment, meta_segment

```
1: Threshold=100;
2: y_met_end=[1 1];
3: while(length(y_met_end) > length(unique(y_met_end))) do
4: isolate=metatarsal_segment;
5: isolate(isolate<threshold) = 0;
6: X_start=round(0.4*size(isolate,2));
7: [val,idx_max] = max(isolate(:,X_start:end),[],2);
8: X_max=idx_max+X_start-1;
9: Y_max=1:size(isolate,1);
10: Initiate met_end=[];
11: for i=1:size(isolate,1) do
12:    R=isolate(i,:);
13:    for j=X_max(i):-1:1 do
14:       if R(j)==0 do
15:          px=j;
16:          py=i;
17:          break
18:       end if
19:    end for
20:    met_end=[met_end;[px py]];
21: end for
22: met_end=met_end(:,1);
23: y_met_end=met_end(:,2);
24: Threshold=Threshold+100;
25: end while
Apply isolation coordinates on main area:
26: figure
27: imagesc(metatarsal_segment)
28: scatter(x_met_end,y_met_end,'w','filled');
Toes cropping:
29: toe_segment= zeros(size(metatarsal_segment,1), size(metatarsal_segment,2));
30: for i=1:size(metatarsal_segment,1)
31: toe_segment(y_met_end(i),1:x_met_end(i))=
metatarsal_segment(y_met_end(i), 1:x_met_end(i));
32: end for
33: toe_segment=toe_segment(:,1:12);
Metatarsal cropping:
34: meta_segment= zeros(size(metatarsal_segment,1), size(metatarsal_segment,2));
35: for i=1:size(metatarsal_segment,1) do
36: meta_segment(y_met_end(i),x_met_end(i):end)
   =metatarsal_segment(y_met_end(i), x_met_end(i):end);
37: end for
```

Algorithm 4.5: Toes cropping

Input: toe_segment
Output: T

```
1: max_toe_row=max(toe_segment,[],2);
2: [peaks_toe,row_peaks_toe]=findpeaks(max_toe_row);
project peak coordinates:
3: Initiate peak_toe_loc=[];
4: for m=1:size(peaks_toe,1) do
5:    [row,col]=find(toe_segment==peaks_toe(m));
6:   if(size(row,1)>1) || (size(col,1)>1) do
      col=col(2); row=row(2);
     end if
```

```
7:    peak_toe_loc=[peak_toe_loc;row col];
8: end for
Big toe extraction
9: toe_num=1;
10: for i=1:length(toe_num) do
11: T_loc=peak_toe_loc(toe_num,:);
12: T_row=T_loc(1); T_col=T_loc(2);%peak pixel location
First level neighboring pixels to the peak:
13: T_RP_row=T_row ; T_RP_col=T_col+1;
14: T_LP_row=T_row ; T_LP_col=T_col-1;
15: T_UP_row=T_row-1; T_UP_col=T_col;
16:T_DP_row=T_row+1; T_DP_col=T_col;
17: T_R_UP_row=T_row-1;T_R_UP_col=T_col+1;
18: T_L_UP_row=T_row-1;T_L_UP_col=T_col-1;
19: T_R_DP_row=T_row+1;T_R_DP_col=T_col+1;
20: T_L_DP_row=T_row+1;T_L_DP_col=T_col-1;
Second level neighboring pixels to the peak:
21: T_UP2_row=T_row-2; T_UP2_col=T_col;
22: T_DP2_row=T_row+2; T_DP2_col=T_col;
23: T_R_UP2_row=T_row-2;T_R_UP2_col=T_col+1;
24: T_L_UP2_row=T_row-2;T_L_UP2_col=T_col-1;
25: T_R_DP2_row=T_row+2;T_R_DP2_col=T_col+1;
26: T_L_DP2_row=T_row+2;T_L_DP2_col=T_col-1;
27: T_RP2_row=T_row ; T_RP2_col=T_col+2;
28: T_LP2_row=T_row ; T_LP2_col=T_col-2;
Third level neighboring pixels to the peak:
29: T_R_UP3_row=T_row-1;T_R_UP3_col=T_col+2;
30: T_R_UP4_row=T_row-2;T_R_UP4_col=T_col+2;
31: T_L_UP3_row=T_row-1;T_L_UP3_col=T_col-2;
32: T_L_UP4_row=T_row-2;T_L_UP4_col=T_col-2;
33: T_R_DP3_row=T_row+1;T_R_DP3_col=T_col+2;
34: T_R_DP4_row=T_row+2;T_R_DP4_col=T_col+2;
35: T_L_DP3_row=T_row+1;T_L_DP3_col=T_col-2;
36: T_L_DP4_row=T_row+2;T_L_DP4_col=T_col-2;
37:     T=[toe_segment(T_L_UP4_row,T_L_UP4_col)    toe_segment(T_L_UP2_row,T_L_UP2_col)
toe_segment(T_UP2_row,T_UP2_col)                   toe_segment(T_R_UP2_row,T_R_UP2_col)
toe_segment(T_R_UP4_row,T_R_UP4_col).....
  ;toe_segment(T_L_UP3_row,T_L_UP3_col)              toe_segment(T_L_UP_row,T_L_UP_col)
toe_segment(T_UP_row,T_UP_col)                     toe_segment(T_R_UP_row,T_R_UP_col)
toe_segment(T_R_UP3_row,T_R_UP3_col).....
  ;toe_segment(T_LP2_row,T_LP2_col)                      toe_segment(T_LP_row,T_LP_col)
toe_segment(T_row,T_col)                               toe_segment(T_RP_row,T_RP_col)
toe_segment(T_RP2_row,T_RP2_col).....
  ;toe_segment(T_L_DP3_row,T_L_DP3_col)              toe_segment(T_L_DP_row,T_L_DP_col)
toe_segment(T_DP_row,T_DP_col)                     toe_segment(T_R_DP_row,T_R_DP_col)
toe_segment(T_R_DP3_row,T_R_DP3_col).....
  ;toe_segment(T_L_DP4_row,T_L_DP4_col)              toe_segment(T_L_DP2_row,T_L_DP2_col)
toe_segment(T_DP2_row,T_DP2_col)                   toe_segment(T_R_DP2_row,T_R_DP2_col)
toe_segment(T_R_DP4_row,T_R_DP4_col)];
38: end for
Repeat for all toes
```